

**New materials and architectures  
for organic photovoltaic diodes**

**Ioannis Ierides**

Thesis submitted for the degree of  
Doctor of Philosophy

December 2022

Department of Physics & Astronomy  
University College London



# Declaration

I, Ioannis Ierides, confirm that the work presented in this thesis is my own. For work in the thesis already available in another format, UCL research paper declaration forms have been completed as appropriate. Where information has been derived from other sources, I confirm that this has been indicated in the thesis. All figures appearing in the thesis have been created by the author unless otherwise stated.

---

Ioannis Ierides

Cambridge, 24<sup>th</sup> December 2022

**Principal Supervisor:** Prof. Franco Cacialli

Department of Physics & Astronomy and London Centre for Nanotechnology,  
University College London

(Currently at the Faculty of Science and Technology, Free University of Bozen-Bolzano)

**Subsidiary Supervisor:** Prof. Natalie Stingelin

School of Materials Science and Engineering, Georgia Institute of Technology

# Abstract

The work presented in this thesis has been motivated by the potential of organic photovoltaics (OPVs) to meet the requirements of envisioned photovoltaic (PV) manufacturing methods and future PV applications. Electron transport layers (ETLs) have been instrumental in breaking the power conversion efficiency (PCE) boundaries of solution-processed PVs. New ETLs must enable higher PCEs to be attained and be compatible with large scale manufacturing that benefits from the use of low temperature processes. In this thesis with a view to increase sustainability and compatibility with flexible or foldable substrates I have developed novel ETLs for OPVs processed at an annealing temperature of 150°C, by modifying ZnO ETLs with MgO.

Firstly, I demonstrate OPVs incorporating a “bilayer” ZnO/MgO ETL. These ETLs have a more uniform top surface and a lower work function compared to single ZnO ETLs which is expected to be beneficial to electron extraction. Furthermore, I demonstrate that insertion of the thin (~ 10 nm) MgO interlayer in devices leads to an increase in the shunt resistance ( $R_{SH}$ ) and to a reduction in recombination losses that boost the short circuit current density ( $J_{SC}$ ) and fill factor (FF), enhancing the PCE by ~ 10%.

Secondly, I demonstrate an Mg-doped ZnO ETL formed from a single solution (via the direct addition of the Mg precursor in the ZnO precursor solution). Previous use of such an ETL for OPVs has been limited, and only investigated in

connection with annealing temperatures of  $\sim 300^{\circ}\text{C}$ . I demonstrate that Mg doping ( $\sim 1\%$ ) in the ZnO ETL reduces leakage currents and recombination losses, whilst leaving the work function of the ETL unaffected. A concomitant increase of the  $J_{\text{sc}}$ , open circuit voltage ( $V_{\text{oc}}$ ) and FF leads to an  $\sim 18\%$  enhancement of the PCE.

# Impact statement

Overreliance on fossil fuels for the world's energy supply will have catastrophic consequences for the future of humanity. PVs play a key role in the effort to halt climate change and provide a clean and reliable renewable energy source. The research presented herein, supports the major scientific and industrial effort to develop new PV technologies that have more sustainable production and can enable the wider use of PVs, for example in niche indoor applications.

More specifically, my contribution has been to develop novel ETLs applied to OPVs. Recently, interest in the field of OPVs has been re-ignited due to the development of non-fullerene acceptors (NFAs) that enabled the PCE of single junction OPVs to exceed 18%. My findings can facilitate pushing the PCE of OPV technologies further, bringing them one step closer to wider commercial applications. The applicability of my work to industrial large-scale settings has been central in my development efforts, and for this reason all of my devices are fabricated at temperatures not exceeding 150°C.

Beyond the potential impact my work has on the commercialisation of OPVs, the addition of my work in the body of knowledge, allows other researchers to extract design rules for further developments of ETLs for solution-processed PVs. For example, through my investigations, I show that high transparency and a high ionisation potential can serve as useful design rules for modifiers of ETLs. My work has been disseminated via several publications in internationally renowned

journals and talks at major conferences to increase exposure to the scientific community. The work has been recognised by the institution of engineering and technology, resulting in the presentation of a postgraduate researcher award to the author.

# Research dissemination & research paper declaration forms

Work presented in this thesis or carried out in parallel has led to the following publications and conference presentations.

Peer reviewed journals:

1] **I. Ierides**, I. Squires, G. Lucarelli, T. M. Brown, F. Cacialli. *Inverted organic photovoltaics with a solution-processed ZnO/MgO electron transport bilayer*, Journal of Materials Chemistry C, 9, 11, 3901-3910 (2021)<sup>1</sup>

2] **I. Ierides**, G. Ligorio, M. A McLachlan, K. Guo, E. J. W. Kratochvil, F. Cacialli. *Inverted organic photovoltaics with a solution-processed Mg-doped electron transport layer annealed at 150°C*, Sustainable Energy & Fuels, 6, 11, 2835-2845 (2022)<sup>2</sup>

3] **I. Ierides**, A. Zampetti, F. Cacialli. *The resurgence of organic photovoltaics*, Current Opinion in Green and Sustainable Chemistry, 17, 15-20 (2019)<sup>3</sup>

4] M. Pompilio, **I. Ierides**, F. Cacialli. *Biomimetic Approaches to “Transparent” Photovoltaics: Current and Future Applications*. Molecules 28(1) 180 (2022)<sup>4</sup>

5] A. Attanzio, M. Rosillo-Lopez, A. Zampetti, **I. Ierides**, F. Cacialli, C. G. Salzmann, M. Palma. *Assembly of graphene nanoflake–quantum dot hybrids in aqueous solution and their performance in light-harvesting applications*, *Nanoscale*, 10, 42, 19678-19683 (2018)<sup>5</sup>

Conference contributions:

1] **I. Ierides**, K. Guo, I. Squires, G. Lucarelli, T. M. Brown, F. Cacialli. *Organic electronics with solution-processed electron transport layers based on ZnO and MgO*, MRS Fall Meeting 2021, Talk

2] **I. Ierides**, G. Lucarelli, T. M. Brown, F. Cacialli. *MgO Interlayers in Emergent Photovoltaics*, ICMAT 2019, Talk

3] **I. Ierides**, G. Lucarelli, T. M. Brown, F. Cacialli. *Revealing the function of an MgO interlayer in emerging photovoltaics*, InnoLAE 2019, Poster presentation

1. For a research manuscript that has already been published (if not yet published, please skip to section 2):		
a) Where was the work published? (e.g. journal name)	Journal of Materials Chemistry C	
b) Who published the work? (e.g. Elsevier/Oxford University Press):	Royal Society of Chemistry	
c) When was the work published?	16/02/2021	
d) Was the work subject to academic peer review?	Yes	
e) Have you retained the copyright for the work?	Yes	
[If no, please seek permission from the relevant publisher and check the box next to the below statement]:		
<input type="checkbox"/> I acknowledge permission of the publisher named under 1b to include in this thesis portions of the publication named as included in 1a.		
2. For a research manuscript prepared for publication but that has not yet been published (if already published, please skip to section 3):		
a) Has the manuscript been uploaded to a preprint server? (e.g. medRxiv):	Please select.	<b>If yes, which server?</b> Click or tap here to enter text.
b) Where is the work intended to be published? (e.g. names of journals that you are planning to submit to)	Click or tap here to enter text.	

c) List the manuscript's authors in the intended authorship order:	Click or tap here to enter text.		
d) Stage of publication	Please select.		
3. For multi-authored work, please give a statement of contribution covering all authors (if single-author, please skip to section 4):			
Ioannis Ierides was involved in the inception of the work, organised and undertook the experiments and drafted/reviewed the manuscript. Isaac Squires assisted with experiments for part of the work. Giulia Lucarelli and Thomas M. Brown assisted with the inception of the work and reviewed the manuscript. Franco Cacialli was involved in the inception of the work and drafted/reviewed the manuscript.			
4. In which chapter(s) of your thesis can this material be found?			
Chapter 4 includes the Figures and Tables presented in this work. Chapters 2 & 3 includes text presented in this work.			
5. <b>e-Signatures confirming that the information above is accurate</b> (this form should be co-signed by the supervisor/ senior author unless this is not appropriate, e.g. if the paper was a single-author work):			
Candidate:	Ioannis Ierides	Date:	24/12/2022
Supervisor/ Senior Author (where appropriate):	Click or tap here to enter text.	Date:	Click or tap to enter a date.

<b>1. For a research manuscript that has already been published (if not yet published, please skip to section 2):</b>		
<b>f) Where was the work published?</b> (e.g. journal name)	Sustainable Energy & Fuels	
<b>g) Who published the work?</b> (e.g. Elsevier/Oxford University Press):	Royal Society of Chemistry	
<b>h) When was the work published?</b>	10/04/2022	
<b>i) Was the work subject to academic peer review?</b>	Yes	
<b>j) Have you retained the copyright for the work?</b>	Yes	
<p>[If no, please seek permission from the relevant publisher and check the box next to the below statement]:</p> <p><input type="checkbox"/> I acknowledge permission of the publisher named under 1b to include in this thesis portions of the publication named as included in 1a.</p>		
<b>2. For a research manuscript prepared for publication but that has not yet been published (if already published, please skip to section 3):</b>		
<b>e) Has the manuscript been uploaded to a preprint server? (e.g. medRxiv):</b>	Please select.	<b>If yes, which server?</b> Click or tap here to enter text.
<b>f) Where is the work intended to be published?</b> (e.g. names of journals that you are planning to submit to)	Click or tap here to enter text.	

g) List the manuscript's authors in the intended authorship order:		Click or tap here to enter text.	
h) Stage of publication		Please select.	
3. For multi-authored work, please give a statement of contribution covering all authors (if single-author, please skip to section 4):			
Ioannis Ierides was involved in the inception of the work, organised and undertook the experiments and drafted/reviewed the manuscript. Kunping Guo assisted with experiments for part of the work. Giovanni Ligorio performed the UPS/XPS investigations and reviewed the manuscript. Martyn A. McLachlan performed the Hall measurements and reviewed the manuscript. Emil J. W. List-Kratochvil reviewed the manuscript. Franco Cacialli was involved in the inception of the work and drafted/reviewed the manuscript.			
4. In which chapter(s) of your thesis can this material be found?			
Chapter 5 includes the Figures and Tables presented in this work. Chapters 2 & 3 includes text presented in this work.			
5. <b>e-Signatures confirming that the information above is accurate</b> (this form should be co-signed by the supervisor/ senior author unless this is not appropriate, e.g. if the paper was a single-author work):			
Candidate:	Ioannis Ierides	Date:	24/12/2022
Supervisor/ Senior Author (where appropriate):	Click or tap here to enter text.	Date:	Click or tap to enter a date.

# Acknowledgements

It is on a rainy Christmas Eve that I am bringing this work to completion with a lot of emotion and pride. The last five years have been an incredible journey and a period of immense personal growth, filled with its ups and downs that would have been impossible without the support of those dear to me. First and foremost, a huge **Thank you** to Constantina. You have been with me throughout this journey, cheering my successes and picking me up and encouraging me when things went awry. An everlasting light in my life, shining through my darkest hours and inspiring me to become the best version of myself. Thank you for sacrificing so much and for believing in me!

I could not have completed this journey without the love and support of my family. To my sister Marisa, and my parents Thoula and Michalis, thank you for never doubting me and always being there to help. Danae, Yianna, Pano, Maro, Constanti, Ntino, Niko, Koulla, Savva, Nefeli, Stephanie, and especially Jason, you have always cared to find out how my PhD journey is coming along and I know that you are proud of me for completing this challenge. Throughout these years I always felt the moral support of my "*κουμπάροι*" Alkis and Simone and my precious friend Demetris, who often visited me in London.

My UCL colleagues have been instrumental in the success of this PhD. My deepest gratitude goes to my supervisor Franco Cacialli for offering me the opportunity to join the group and challenging me to work independently. The

guidance you have offered and help to publish my work has been invaluable and I have learned a great many lessons from our discussions. Many thanks to all the members of the organic semiconductors and nanostructures group. The lively conversations in F9 will never be forgotten. Adil Patel, Michele Pompilio, Kunping Guo, Marcello Righetto, Alessandro Minotto, Tecla Arcidiacono, Giovanni Cotella, Giuseppe Carnicella, Alex Rapidis, Andrea Zampetti, it has been an absolute pleasure to work with you. A special thanks to Isaac Squires and Marcello D'Ascenzi, whom I had the pleasure to supervise. Beyond my research group, a big thank you goes to my second supervisor Natalie Stingelin for her help, George Tsaviris for his endless support and the members of the ACM CDT, especially the director Neil Curson for his pastoral support. I am very grateful to my collaborators Giulia Lucarelli, Thomas M. Brown, Giovanni Ligorio, Martyn A. McLachlan and Richard Thorogate for their valuable input in my research projects. Lastly, I would like to thank the funding bodies for their financial support throughout these years. The work has been supported for four years by the EPSRC and SFI Centre for Doctoral Training in Advanced Characterisation of Materials Grant Ref EP/L015277/1 that has also granted me an additional three month extension for the impact that Covid-19 had on the work. The first three years of my PhD have been supported by a grant from the prestigious Leventis Foundation in Cyprus. The Institution of Engineering and Technology has recognised the impact of the work presented in this thesis and awarded me with a post-graduate research award.

Ioannis Ierides

Cambridge, 24<sup>th</sup> December 2022

# Table of Contents

<b>1 Introduction</b> .....	<b>21</b>
1.1 Thesis overview.....	21
1.2 Thesis structure.....	22
<b>2 Background</b> .....	<b>25</b>
2.1 Photovoltaic technologies.....	25
2.1.1 Photovoltaics .....	25
2.1.2 The current market landscape of photovoltaic technologies .....	28
2.2 Organic photovoltaics.....	33
2.2.1 Introduction to organic semiconductors and diodes.....	33
2.2.2 Brief history and recent developments of organic photovoltaics .....	38
2.2.3 Electron transport layers in organic photovoltaics.....	47
<b>3 Experimental techniques</b> .....	<b>51</b>
3.1 Materials and fabrication methodologies .....	51
3.2 Device characterisation .....	53
3.2.1 Current density–voltage measurements .....	53
3.2.2 Open circuit voltage decay and rise measurements .....	55
3.2.3 External quantum efficiency measurements .....	56
3.2.4 Electroabsorption spectroscopy measurements .....	57
3.3 Sample characterisation.....	62

3.3.1 Kelvin probe .....	62
3.3.2 UV-VIS absorption spectroscopy .....	63
3.3.3 Profilometry.....	64
3.3.4 Atomic force microscopy.....	64
3.4 Measurements carried out by partners .....	64
3.4.1 X-ray photoelectron spectroscopy (XPS) and ultraviolet photoemission spectroscopy (UPS) .....	64
3.4.2 Hall measurements .....	65
<b>4 ZnO/MgO bilayer electron transport layers .....</b>	<b>66</b>
4.1 Introduction.....	66
4.2 Experimental details .....	68
4.2.1 Solution preparation.....	68
4.2.2 Device fabrication .....	69
4.3 Preliminary investigations.....	71
4.4 Results .....	75
4.4.1 Electrical characterisation of organic photovoltaic devices .....	76
4.4.2 Characterisation of electrodes .....	79
4.4.3 Extending the use of ultrathin MgO to other types of organic photovoltaic diodes .....	88
4.5 Conclusions.....	90
<b>5 Mg-doped ZnO electron transport layers.....</b>	<b>92</b>

5.1 Introduction .....	92
5.2 Experimental details .....	96
5.2.1 Solution preparation.....	96
5.2.2 Device fabrication .....	97
5.3 Preliminary investigations.....	98
5.3.1 Optimisation of the PM6:Y6 active layer .....	98
5.3.2 Formation of the Mg-doped ZnO electron transport layers .....	102
5.4 Results .....	105
5.4.1 Electrical characterisation of organic photovoltaic devices .....	105
5.4.2 Characterisation of electrodes .....	109
5.4.3 Discussion: Origin of performance improvement and comparison with previous literature .....	115
5.4.4 Extending the use of Mg-doped ZnO to PM6:Y6 (non-fullerene) organic photovoltaics.....	119
5.5 Conclusions.....	123
<b>6 Conclusions and outlook .....</b>	<b>124</b>
6.1 Summary and conclusions .....	124
6.2 Future research .....	128
<b>Bibliography.....</b>	<b>130</b>

# Abbreviations

A-D-A	Acceptor–donor–acceptor
BHJ	Bulk heterojunction
BIPVs	Building integrated photovoltaics
(c)AFM	(Conductive) Atomic force microscopy
CIGS	Copper indium gallium selenide
CN	1-chloronaphthalene
CZTS	Copper zinc tin sulphide
DIO	1,8-diiodooctane
D-A-D	Donor-acceptor–donor
EA	Electroabsorption
$E_b$	Binding energy
EQE	External quantum efficiency
ETL(s)	Electron transport layer(s)
FF	Fill Factor
FRET	Förster resonance energy transfer
HOMO	Highest occupied molecular orbital
HOPG	Highly oriented pyrolytic graphite
HTL(s)	Hole transport layer(s)
IOT	Internet of things
ITO	Indium tin oxide
$J_{PH}$	Photocurrent density
$J_{sc}$	Short circuit current density

LUMO	Lowest unoccupied molecular orbital
NFA(s)	Non-fullerene acceptor(s)
OPV(s)	Organic photovoltaic(s)
OS	Organic semiconductors
PCE	Power conversion efficiency
PEDOT:PSS	Poly(3,4-ethylenedioxythiophene) polystyrene sulfonate
PSC(s)	Perovskite solar cell(s)
PV(s)	Photovoltaic(s)
Rpm	Revolutions per minute
R <sub>s</sub>	Series resistance
R <sub>SH</sub>	Shunt resistance
SECO	Secondary electron cut off
SMU	Source measure unit
Sq	Root mean square roughness
UPS	Ultraviolet photoemission spectroscopy
V <sub>BI</sub>	Built-in potential
V <sub>EFF</sub>	Effective voltage
V <sub>OC</sub>	Open circuit voltage
WEO	World energy outlook
XPS	X-ray photoelectron spectroscopy
P <sub>DISS</sub>	Relative exciton dissociation efficiency

# 1 Introduction

## 1.1 Thesis overview

The case for photovoltaics (PVs) as one of the main tools in our arsenal to tackle climate change is strong. As the PV technology scales, the call for materials that offer higher efficiency, enablement of novel applications and, at the same time, a more environmentally friendly production becomes vital, requiring an eventual move away from the current incumbent silicon.

Solution-processed PVs enable a new manufacturing paradigm for cheap deposition over large areas and organic photovoltaics (OPVs) in particular are a key solution to focus on, due to their high indoor PV efficiency.

The use of an electron transport layer (ETL) is crucial in inverted OPVs in order to enhance charge extraction, with the metal oxide ZnO being a frequent choice. To keep in line with a “green” PV production, the processing temperature of ZnO films should be kept below 150°C. ZnO ETLs are usually sub-optimal, for example, due to the presence of surface defects. The main strategies developed to improve ZnO ETLs include treatment with UV-ozone, the application of a modifying interlayer between ZnO and the active layer and the direct addition of dopants in the precursor solution of the ZnO ETL to form doped ZnO ETLs.

The latter two techniques are explored in this thesis, where MgO is used to modify ZnO ETLs formed by simple solution-processing and low temperature annealing

(150°C), initially by the formation of a bilayer ZnO/MgO ETL followed by the modification via the doping of ZnO with MgO.

## 1.2 Thesis structure

The subsequent sections of this thesis are organised as follows:

Chapter 2:

Initially, the basis for the motivation of carrying out the research in this thesis is discussed, by outlining the potential impact of the PV technology, the main way to assess the technology and by describing the current PV market and the key drivers for exploring PVs beyond those based on silicon. Since the focus of the thesis is in OPVs, the fundamental physics of organic semiconductors (OS) and their corresponding diodes are introduced, followed by an overview of the milestones in the development of OPVs, namely, the bilayer device, the bulk heterojunction, ternary and tandem OPVs and the recent discovery of non-fullerene acceptors (NFAs). Finally, the discussion is focused on the characteristics of ETLs and specifically ZnO and the different strategies by which it can be modified to improve OPV PCE.

Chapter 3:

The experimental methods used to characterise OPV devices and ETLs are discussed. These include optoelectronic methods such as current density-voltage, open circuit voltage ( $V_{oc}$ ) decay and rise, external quantum efficiency (EQE) and electroabsorption (EA) spectroscopy measurements as well as photophysical methods such as Kelvin probe, UV-VIS absorption spectroscopy, profilometry and atomic force microscopy (AFM) measurements. Experiments carried out by

collaborators that include XPS, UPS and Hall measurements are also briefly described.

#### Chapter 4:

In chapter 4, the strategy of employing ultrathin (~ 10 nm) MgO to serve as the top component of a ZnO/MgO bilayer ETL to improve OPV performance is explored. Initially, the literature of bilayer ETLs based on ZnO and prior uses of metal oxide/MgO bilayer ETLs in optoelectronic devices is reviewed. The experimental procedures used to fabricate devices and samples are detailed, together with preliminary investigations that describe the optimisation studies that led to the ITO/ZnO/PTB7-Th:PC<sub>70</sub>BM/MoO<sub>3</sub>/Au OPV device that is used as benchmark for the rest of the investigations. In the results section, current density-voltage investigations, analysis of devices including the dependence of photocurrent density ( $J_{PH}$ ) on the effective voltage ( $V_{EFF}$ ) and  $V_{OC}$  decay and rise curves are presented. In addition to the above studies, AFM, cAFM, Kelvin probe and optical spectroscopy (namely transmittance, absorbance and EA) measurements are presented. OPVs with the modified ETL for both fullerene and NFA active layer blends are tested.

#### Chapter 5:

In chapter 5, the strategy of doping the ETL by directly adding an Mg precursor in a ZnO precursor solution to form an Mg-doped ZnO ETL is explored. Initially, successful dopants for ZnO ETLs and prior uses of the Mg-doped ZnO ETLs in optoelectronic devices are discussed. The experimental procedures used to

fabricate devices and samples are detailed, together with preliminary investigations that describe the optimisation studies that led to the ITO/ZnO/PM6:Y6/MoO<sub>3</sub>/Au OPV device that is used as benchmark for a portion of the investigations. In the results section, XPS is initially used to assess the ETL films. This is followed by current density - voltage investigations, analysis of the dependence of the  $J_{PH}$  on  $V_{EFF}$ , and measurements of the  $V_{OC}$  decay and rise. Furthermore, UPS, Kelvin probe, AFM optical spectroscopy and Hall measurements are carried out. OPVs with the modified ETL for both fullerene and NFA active layer blends are tested. The above studies together with a brief investigation of devices with ETLs fabricated at an annealing temperature of 300°C, are used to explain the findings within the context of pre-existing literature.

## Chapter 6:

The main findings in each chapter are summarised followed by the possibilities of future research for the work presented in this thesis.

# 2 Background

## 2.1 Photovoltaic technologies

### 2.1.1 Photovoltaics

PV technology is viewed as one of the key technologies with the scope and potential to leverage renewable energy sources and meet the challenge of increasing demand for current and future generations, since it enables the use of the Sun; an “infinite” source of energy. The PV process is “green” and the electricity produced does not result in CO<sub>2</sub> emissions. The only (and minor) CO<sub>2</sub> footprint of PV energy technologies is related to the fabrication and installation of the plants. Hence PVs play a central role in the world’s energy roadmap to 2050.<sup>6</sup>

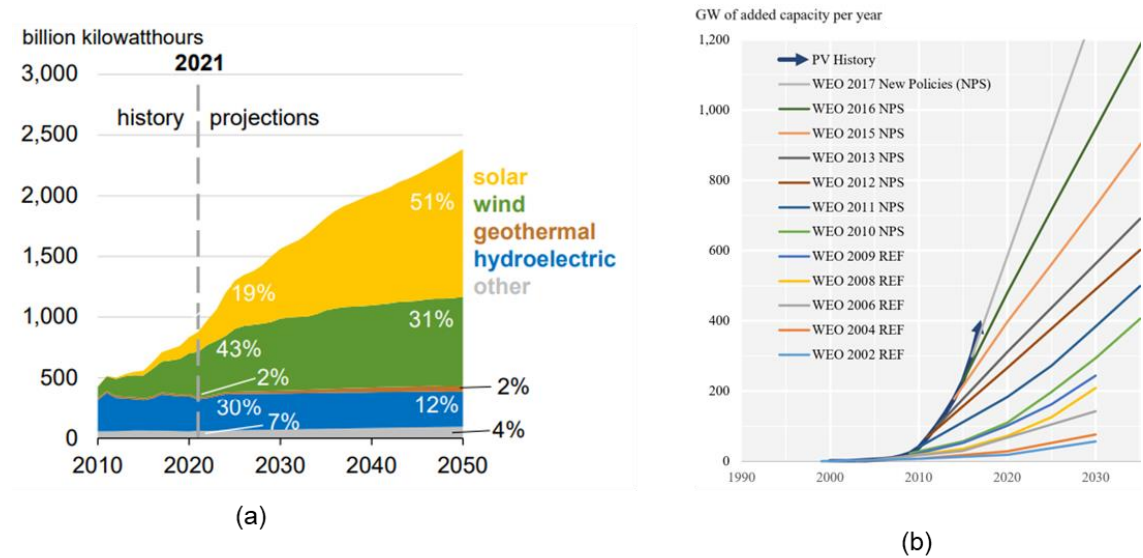


Figure 1. (a) The US Energy Information Administration annual energy outlook 2022 predictions for electricity generation from renewable energy sources in the US between today and at 2050.<sup>7</sup> (b) Yearly projections of forecasted PV applications vs. actual PV installations (REF stands for reference and NPs for new policies reports).<sup>8</sup>

Figure 1 (a) shows the forecasted renewable electricity generation in the U.S. from different sources. Solar (including both PV and solar-thermal) is showing the biggest expected increase in future years from 19% in 2021 to 51% in 2050.<sup>7</sup> As demonstrated in Figure 1 (b) the installed capacity of PVs has constantly exceeded the yearly forecasts of installations (as forecasted by the International Energy Agency in their world energy outlook (WEO) reports),<sup>8</sup> showcasing that the benefits of this technology are established and current market drivers are in place to accelerate its use.

The PV effect refers to the phenomenon where a voltage/current is generated in a material upon exposure to light. In a semiconductor, incoming photons can excite electrons from the valence band into the conduction band, leaving positive quasi particles called holes in the valence band. There is a Coulombic attraction between electrons and holes which leads to the formation of an exciton. The binding energy of an exciton ( $E_b$ ), that is, the energy required to separate the electron and hole into free charges can be rationalised in terms of the Coulombic binding energy of two charges as summarised by equation (1).

$$E_b = \frac{q_1 q_2}{4\pi r \epsilon_0 \epsilon_r} \quad (1)$$

where  $q_1, q_2$  refer to the charges of the electron and hole,  $r$  is their separation distance,  $\epsilon_0$  the vacuum permittivity and  $\epsilon_r$  the dielectric constant. When  $E_b < k_b T$ , where  $k_b$  is Boltzmann's constant and  $T$  the temperature, the exciton can dissociate freely. In the case of silicon for example this is  $\sim 15$  meV ( $\epsilon_r \sim 11.7$ ) and since this is less than the thermal energy at room temperature ( $k_b T \sim 26$  meV) free charge carriers can be generated in the material upon

photoexcitation. Although equation (1) only provides a simplified description,<sup>9</sup> it does capture the overall important dependence of the binding energy on the dielectric environment and on the charge.

Rather than allowing the charge carriers to recombine, the introduction of an in-built asymmetry to the system enables their use to power an external circuit. The effectiveness of a PV device depends upon the choice of light absorbing materials and the way in which they are connected to the external circuit.<sup>10</sup> To enable comparison between different PV devices, a few key performance indicators have been established. These are expressed in equation (2) and shown diagrammatically in a typical current density – voltage characteristic of a PV diode in Figure 2.

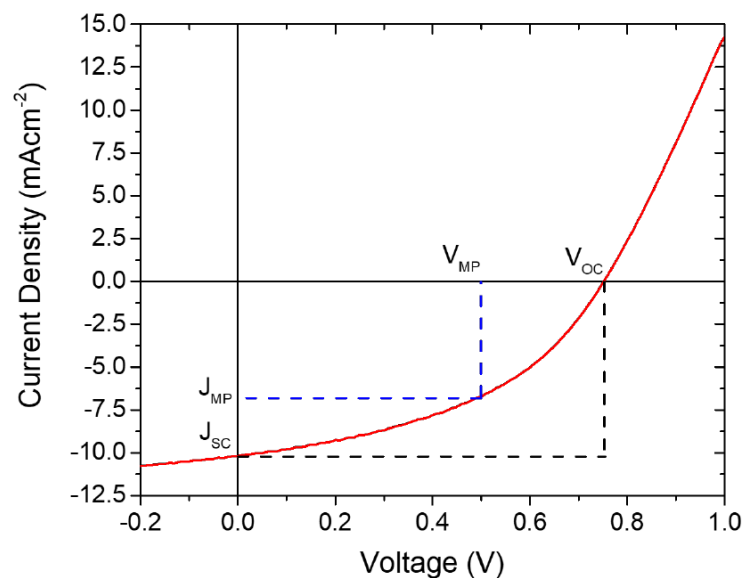


Figure 2. A typical current density-voltage curve of a PV diode under illumination.

$$PCE = \frac{J_{SC} \times V_{OC} \times FF}{P_{IN}} \quad (2)$$

where  $PCE$  is the power conversion efficiency of the system,  $P_{IN}$  is the incoming (optical) power density (per unit area),  $J_{SC}$  (short circuit current density) is the current density at 0 voltage,  $V_{OC}$  (open circuit voltage) is the voltage at 0 current density and  $FF$  is the “so-called” fill factor. The  $FF$  is defined as  $= \frac{J_{MP} \times V_{MP}}{J_{SC} \times V_{OC}}$ , where  $J_{MP}$  and  $V_{MP}$  correspond to the current density and voltage at the maximum power output of the device respectively. The  $FF$  can therefore be thought of as the ratio of the areas enclosed by the dotted blue lines and the axes relative to the dotted black line and the axes in Figure 2. The  $PCE$  (and the parameters it depends on) is the central consideration when assessing materials and architectures for use as PV devices. However, other characteristics of the system have become increasingly important since desired PV solutions must also be economically viable and ideally enable for a circular economy. When assessing PV technologies, characteristics such as the earth abundance of the materials used, the necessitated manufacturing processes, the stability and toxicity of the materials and potential recycling and refurbishment strategies to minimise environmental impact need to be considered.<sup>11</sup>

### **2.1.2 The current market landscape of photovoltaic technologies**

The PV market for the year 2020-2021 was valued at \$200 billion and is expected to grow to \$1000 billion by 2028.<sup>12</sup> It has been dominated by doped crystalline silicon PVs that make up more than 95% of installed solar cell modules.<sup>13</sup> Although silicon is likely to dominate the market for many more years, there are

some drawbacks associated with this technology. Even though increasing economies of scale enable a significant decrease on the price of silicon modules year on year, the balance of system costs (including costs of installations and cost for inverters for example) is not decreasing at the same pace. To achieve decreased balance of system costs, higher efficiency modules are necessitated so that fewer modules and hence peripherals and less effort are required for installations of equivalent capacity.<sup>14</sup> Silicon single junctions have been refined overtime and are already close to their maximum possible efficiency. Hence the most promising way to achieve higher efficiency is to look at other PV materials. In addition, because silicon is an indirect band gap semiconductor material, thick layers are necessitated and the manufacturing process of silicon solar cells requires high temperature treatments that are harmful for the environment due to their increased CO<sub>2</sub> footprint.<sup>15</sup> New envisioned applications for PVs include vehicle integration to increase the range of electric vehicles as well as building integrated photovoltaics (BIPVs). Such applications necessitate lightweight (as opposed to the heavy and thick silicon) modules and durable flexible modules that can withstand several bending cycles. The latter need to be fabricated on substrates which cannot withstand temperature treatments higher than ~ 150°C.<sup>16-19</sup> Design flexibility for PVs has also been of increasing value hence material requirements from architects include semi-transparency or colour-tunability.<sup>4</sup> Lastly the need to power devices that operate indoors rather than outdoors has increased the demand of materials that have high indoor efficiency. Unfortunately the indoor efficiency of silicon and flexibility in its design are

currently lacking, and it is challenging to meet the demand for these niche applications.<sup>20</sup>

To meet the above requirements, several technologies are currently under intense research. These include PVs based on organic semiconductors (henceforth referred to as organic photovoltaics (OPVs)), hybrid halide perovskites (henceforth referred to as perovskite solar cells (PSCs)),<sup>21-23</sup> quantum dot PVs,<sup>24</sup> copper zinc tin sulphide (CZTS)<sup>25</sup> and copper indium gallium selenide (CIGS) PVs.<sup>26</sup> The comparison between the progress in PCEs under 1 Sun illumination achieved with these technologies overtime is shown in Figure 3.

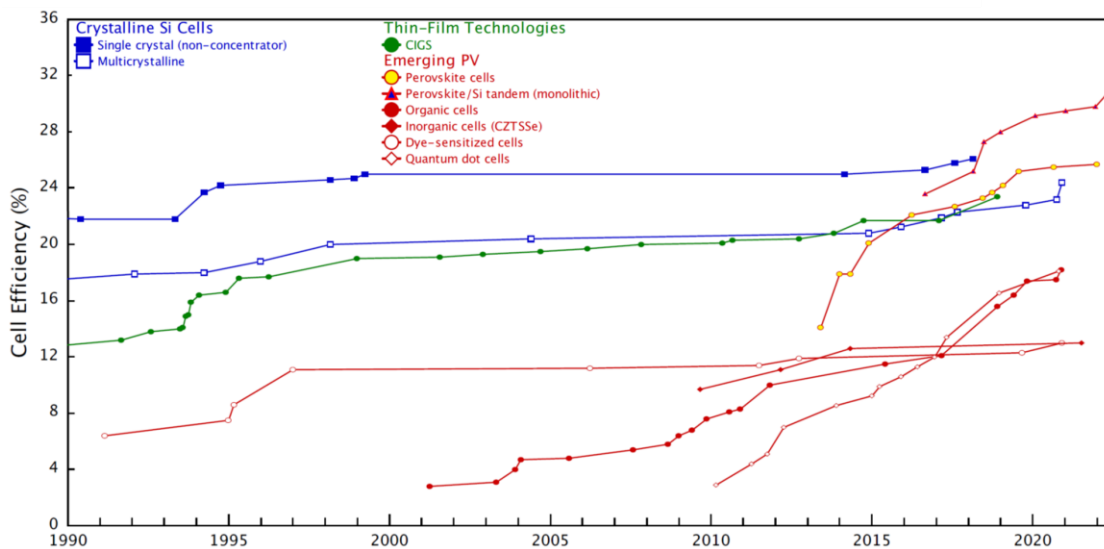


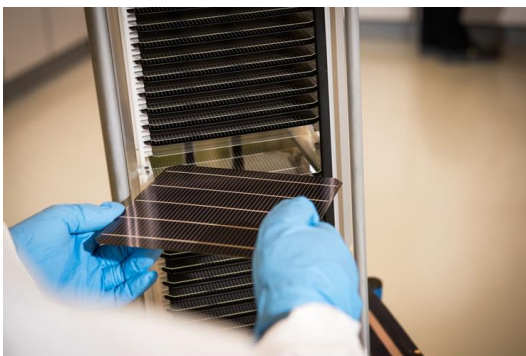
Figure 3. Progress in PCEs for different PV technologies under development in laboratories.<sup>27</sup>

A key advantage of a number of the emerging PV technologies that makes them such viable candidates to eventually replace silicon, is their compatibility with solution-processable fabrication that enables a new manufacturing paradigm for cheap deposition over large areas. Such processes are also less energy intensive and lead to more environmentally friendly production.

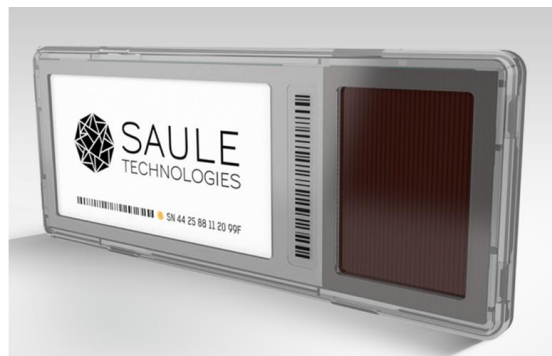
## **Early commercialisation of hybrid halide perovskite solar cells**

Out of the emerging PV materials PSCs are most poised for commercialisation. Their PCE rose from 3.8 to more than 25% for a single junction within a decade or so.<sup>28</sup> PSCs have almost ideal optoelectronic properties, such as high optical-absorption coefficients,<sup>29</sup> balanced and long hole/electron diffusion lengths,<sup>30</sup> high defect tolerance<sup>31</sup> and very small exciton binding energies ( $\sim 10$  meV).<sup>32</sup> Perovskites typically adopt a 3D crystal ABX<sub>3</sub> structure, where the A-cation is an organic or inorganic one (e.g. methylammonium, formamidinium or caesium), the B-cation is either lead or tin, and the X-anion is a halide (mainly chlorine, bromine, or iodine). PSCs are made of earth abundant materials and can meet the requirements of novel solar cell applications that silicon struggles to achieve. In addition, another significant advantage is their compatibility with silicon to form tandem solar cells. Tandem solar cells consist of two PV materials stacked on top of one another with the high bandgap material (perovskite in this case) on top (i.e., close to the transparent electrode through which light is entering the device) to absorb high energy photons and then the low energy gap material (silicon in this case) below to absorb the low energy photons. Perovskite/silicon tandem solar cells could in principle achieve PCEs exceeding 30% and cells with over 29% PCE have already been demonstrated in practice.<sup>33</sup> In this way PSCs do not need to compete with silicon directly, but can be integrated easily into existing silicon PV modules and give them more mileage, whilst offering the opportunity for perovskite technologies to penetrate the markets.

Stability has been a major challenge that PSCs face but this issue has been adequately resolved (with further improvements anticipated in the future) to enable the fabrication of devices with expected lifetime of 20+ years, as showcased by Oxford PV (Figure 4 (a)).<sup>33</sup> There is, however, an issue with PSCs that has yet to be resolved, their reliance on toxic lead. Due to its limited amount in the active layer, the use of lead does not seem to limit the applicability of PSCs in the industry, especially for applications away from humans such as solar farms.<sup>34</sup> However, the use of lead becomes more questionable when considering how PSCs can address other markets for PVs such as those requiring indoor applications. These include, for example internet of things (IOT) applications that are nearer to humans. Some believe that despite the use of lead there is a market for PSCs in these use cases too, with demonstrations being made from Saule Technologies for example, with their PV powered shelf labels (Figure 4 (b)).<sup>35</sup>



(a)



(b)

*Figure 4. (a) Silicon-perovskite tandem solar cells by Oxford PV.<sup>33</sup> (b) PSC electronic shelf labels IOT solution by Saule Technologies.<sup>35</sup>*

### **Early commercialisation of organic photovoltaics**

Consumer perception for lead products gives a considerable advantage to other emerging technologies to address these niche markets. OPVs in particular may

be better suited for these, since, in addition to the non-toxic materials used in these PVs, their indoor efficiency seems to be one of the highest from the emerging technologies.<sup>20, 36</sup> Epishine, a Swedish start-up founded in 2016, already commercialised OPVs for these applications.<sup>37</sup>

Intensive research is still required to perfect the emerging PV technologies, to make them future-proof and viable competitors to silicon. For OPVs, several advances have been reported in the field in the last few years with PCE (under 1 Sun illumination) now exceeding 18% for single junctions.<sup>38</sup> Currently the biggest obstacle for OPVs to reach widespread commercialisation is stability. In addition to stability, other challenges include boosting the performance even further to exceed a PCE of 25% and ensuring that the fabrication methods used in the multilayer structure of these devices are suited to enable novel (and less energy intensive) manufacturing paradigms such as roll to roll manufacturing on bendable substrates. The developments presented in this thesis, align with the effort to increase performance of OPVs within a future-proof framework. In chapter 4 and chapter 5, ZnO - a typical ETL for OPVs is improved with the use of MgO at low processing temperatures - compatible with the desired manufacturing processes.

## **2.2 Organic photovoltaics**

### **2.2.1 Introduction to organic semiconductors and diodes**

Organic semiconductors are a class of carbon-based materials - ranging from small molecules to polymers - that have the ability to conduct electricity. Carbon

has 4 valence electrons in its outer atomic shell and therefore can achieve  $sp$ ,  $sp^2$  and  $sp^3$  hybridisation.

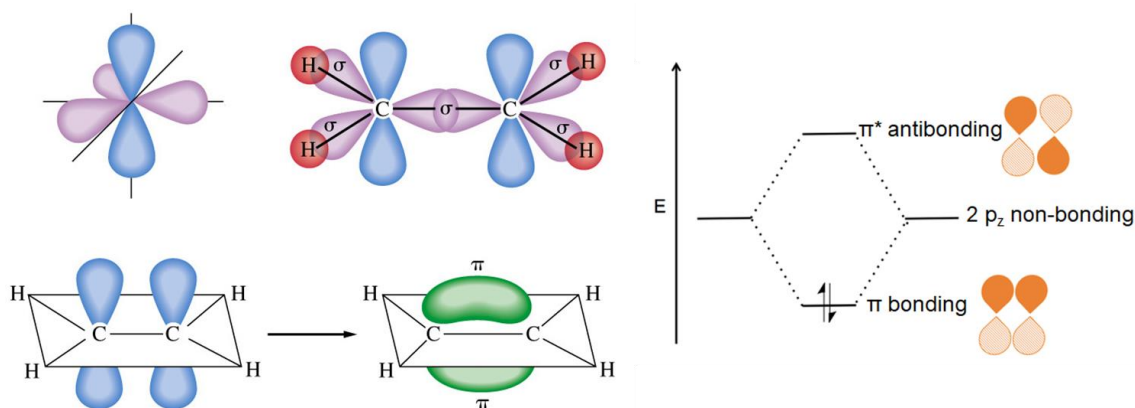


Figure 5. Formation of the  $\pi$  bond and orbitals for ethene. The  $sp^2$  hybridised atoms form three coplanar  $\sigma$  bonds with  $120^\circ$  to each other, while the remaining  $p_z$  orbital is able to delocalise and form a double bond. This leads to the formation of a higher energy  $\pi^*$  orbital and a lower energy  $\pi$  orbital.

When  $sp^2$  hybridised carbon atoms come together, formation of a molecular orbital - and bond - takes place consisting of a bonding orbital ( $\pi$ ) lower in energy than the original  $p_z$  orbital and a higher energy anti-bonding orbital ( $\pi^*$ ). Figure 5 shows the formation of this molecular orbital for the case of ethene. Increasing the number of carbon atoms added to the chain will result to a conjugated system with altering single and double bonds. This leads to the formation of a greater number of molecular orbitals and consequently the discrete  $\pi$  and  $\pi^*$  orbitals form quasi-continuous bands. Electrons occupy the lowest energy levels first, with the uppermost level of the filled  $\pi$  band labelled as the highest occupied molecular orbital (HOMO) while the lowest level of the  $\pi^*$  band is termed as the lowest unoccupied molecular orbital (LUMO). An energy gap between the HOMO and LUMO is always present as demonstrated by Peierls.<sup>39</sup> By considering the

case of polyacetylene with an infinite number of carbon atoms, he showed that instead of the naively expected 1-D metallic system that would originate from equal C-C bond lengths, it is energetically favourable for a non-metallic structure with an energy gap to be present. However, increasing the conjugation leads to a decreased energy gap in general, although topological and chemical defects that occur in these materials in relatively high numbers pose a limit to the spatial extent of the conjugated  $\pi$ -electron system. This is quantified by the so-called effective conjugation length, or the length of the corresponding, defect-free oligomer that would have the same energy gap. Importantly, the delocalisation of the electron wavefunction in the  $\pi$ -orbital results in conductivity in these systems.

In addition, it should be noticed that the lattice of conjugated polymers is soft, e.g. in comparison with that of inorganic ones such as silicon. Therefore, the formation of excited species in these systems leads to structural reorganisation, slightly altering the bond length environment surrounding the excited species. This change in molecular configuration reduces the overall energy of the system; therefore these (excited) species have energies within the forbidden gap. The absorption of a photon by OS leads to the formation of a bound exciton due to a relatively low dielectric constant ( $\epsilon_r \sim 2.5$ , equation (1)). This might be beneficial for light-emitting devices but makes the use of OS in devices where charge separation is necessary (OPVs and organic photodetectors), more challenging. In addition, excitons in OS have a limited diffusion length (10 nm or so for singlets, and somewhat longer 70 nm or so, for triplets).<sup>40, 41</sup> The diffusion of (singlet)

excitons in OS can be modelled using Förster resonance energy transfer (FRET).<sup>42</sup>

The simplest device configuration for an OS diode consists of the photoactive material sandwiched between two electrodes as shown in Figure 6.

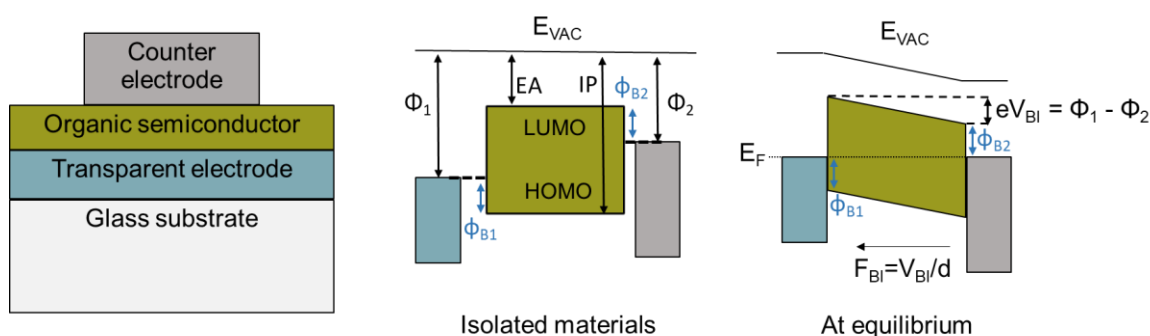


Figure 6. Device structure and schematic energy level diagram of a single layer OS device before and after application of electrodes. The tilting of the band levels is displayed.  $E_{VAC}$  is the vacuum energy,  $\Phi$  is the work function of the contacts, EA the electron affinity, IP the ionisation potential and  $\phi$  the barrier height between the OS and electrode.  $V_{BI}$  is the built-in voltage and  $F_{BI}$  the corresponding built-in field that has the direction indicated by the arrow.

The two electrodes will have different work functions depending on their device function. As soon as the device components come in contact, electrons from the low work function electrode will flow towards the high work function electrode until the electrochemical potentials are equalised and thermodynamic equilibrium is reached. As demonstrated in Figure 6, the band levels of the OS tilt and remain rigid with very limited band bending. This is due to the limited concentration of free charges in OS and the use of very thin layers ( $\sim 100$  nm). As a consequence of the significantly reduced number of free carriers present, contribution to the screening effect (usually found in inorganic semiconductors where band bending is more typical) is limited, therefore the OS can be approximated to have linear

band edges and consequently a uniform electric field ( $F_{BI}$ ) is formed by the migration of charges between the electrodes. The built-in potential ( $V_{BI}$ ) is a crucial factor in device operation as it facilitates the extraction/injection of charge carriers. Application of a bias can be used to either increase or decrease the total potential,  $V_T$ , present in the device ( $V_T = V_{DC} - V_{BI}$ ) as shown in Figure 7.

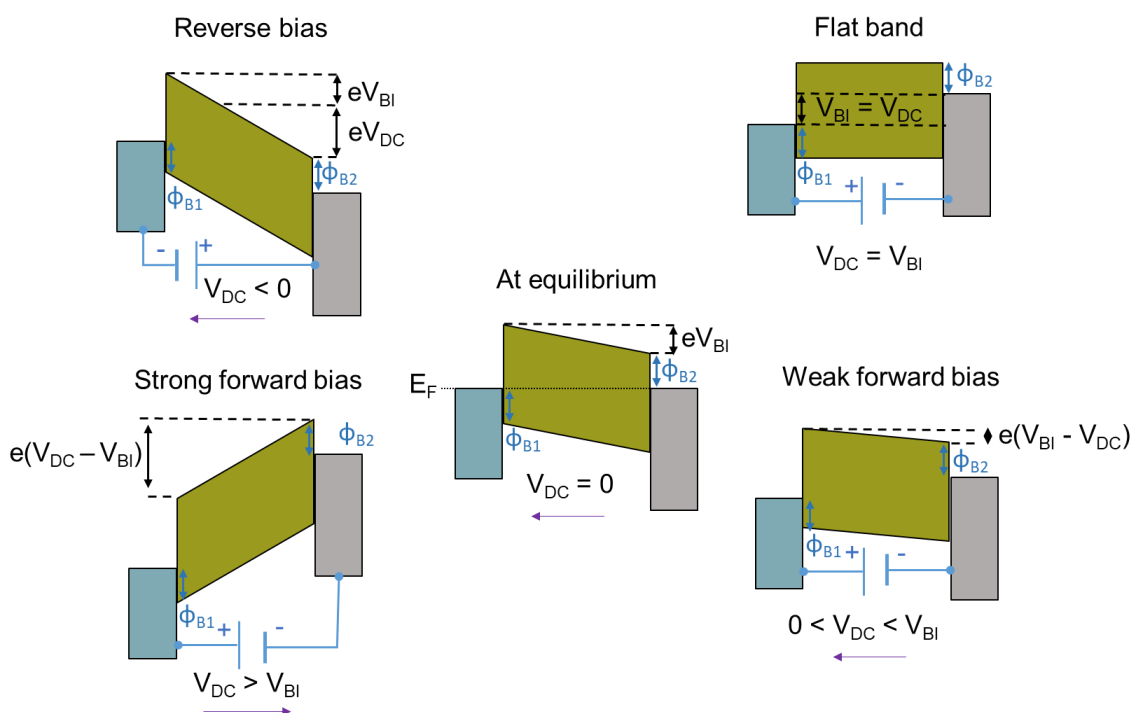


Figure 7. Different regimes of operation for an OS device dependent on the applied external bias. The (conventionally) positive value of  $V_{DC}$  is applied to create a field to oppose the existing built-in field. The purple arrow signifies the direction of the total field after the application of the external bias. In the operation of organic light-emitting diodes usually a strong forward bias is necessary, while organic photodetectors require a strong reverse bias.

## **2.2.2 Brief history and recent developments of organic photovoltaics**

OS rapidly became a success story for light-emitting diodes and then displays, now found in a plethora of commercial applications. On the other hand, OPVs have lagged behind due to their limited PCEs compared to the dominant PV technology (crystalline Si, or c-Si, affording PCEs >20% even in large modules). Up until 1985, OPVs consisted of only a single layer, similar to the example shown in Figure 6. Due to the typically high exciton binding energy of OS (0.5 eV or so) only about 1 in 10 million excitons dissociate spontaneously. Dissociation of excitons is essential for OPVs, to create the free charges that can be collected by the electrodes, therefore these devices exhibited very low PCEs. Tang, was the first to introduce the novelty of a bilayer structure that boosted efficiency beyond 1% and ignited interest in the field.<sup>43</sup> Forming a heterojunction between electron donating (donor) and electron accepting (acceptor) OS, allowed for efficient exciton splitting by providing a driving force to overcome the high binding energy of excitons (~ 0.5 eV). This type of device structure however, has a limitation. The photo-generated singlet excitons must diffuse to the interface of the two materials to split, but singlet excitons in OS have diffusion lengths of only ~ 10 nm. This means that for devices of typical thicknesses (~ 200 nm) only 5% of the singlets can dissociate to form free charge carriers.

The advent of the bulk heterojunction (BHJ) concept that followed solved this issue. Before deposition, the donor and acceptor are mixed in solution which allows formation of extended donor-acceptor interfaces with both mixed and

crystalline regions significantly boosting performance.<sup>44, 45</sup> The bilayer and BHJ OPV structures are shown in Figure 8.

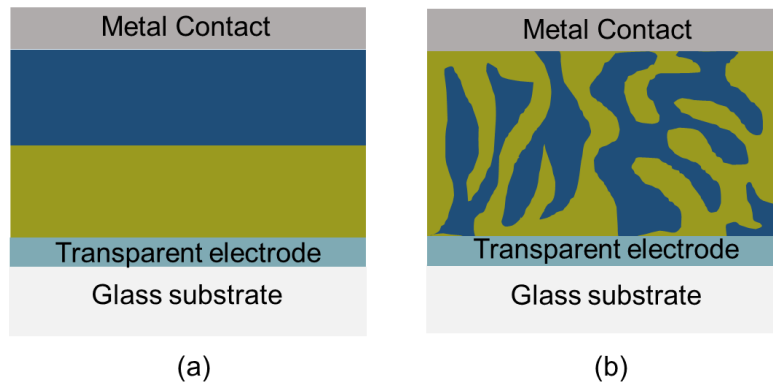


Figure 8. Schematic of (a) a bilayer OPV structure and (b) a bulk-heterojunction OPV structure.

### Operating principle and design rules for organic photovoltaics

The operating principle of OPVs is shown diagrammatically in Figure 9.

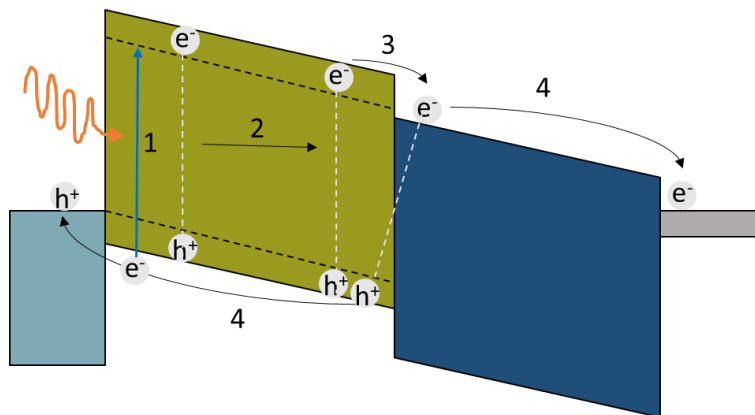


Figure 9. Operating principle of OPVs. The photo-generated exciton (step 1) diffuses to the interface (step 2) where it is split (step 3). The separated free charges can then be collected by the electrodes (steps 4).

An incoming photon is absorbed by the OS leading to the formation of an exciton. The exciton then diffuses through the OS until it either decays to the ground state (radiatively or non-radiatively) or reaches an interface. If the interface is not within the diffusion length of the exciton (in practice  $\sim 10$  nm or so), the so-called

“geminate” recombination will occur (i.e., recombination of an electron and a hole derived from the same original exciton). At the interface, the exciton can instead be dissociated. The dissociation is expected to be driven by the energy level offset between the donor and acceptor, although recent results obtained with a variety of NFAs seem to suggest the importance of this energy offset might have been overrated to some extent. Uncertainties in the exact determination of the semiconductors frontier energy levels make determination of such importance relatively difficult. The dissociation mechanism is thought to happen through the formation of a so called “charge transfer” state. This is a state in which the charges constituting the exciton, while still bound by a Coulombic interaction, are separated by a distance (significantly) larger than in "monomolecular" excitons, e.g. with the electron and the hole on different macromolecular strands either of the same or different chemical nature (the donor and acceptor in this case). Because of the longer distance and the subsequent weaker binding the electron and the hole can separate more easily from one another thus leading to the formation of free charges. The latter can then either be transported to the electrodes and extracted to the external circuit, or they can recombine with oppositely-signed carriers and form again an exciton, in what effectively constitutes a loss mechanism. If recombination is with an oppositely signed carrier that originated from another exciton (as in most of the cases) recombination is said to be “non-geminate”, and “geminate” otherwise.

The above understanding in the basic operation of OPVs helped establish design rules that are instrumental in maximising the PCE of OPVs. For example, for

outdoor operation, the performance of an OPV can be optimised by matching the absorption spectrum of the device to the emission spectrum of the Sun. This ensures a high number of excitons being formed. To prevent geminate recombination, materials that have high exciton diffusion lengths are selected but also care must be taken to provide an optimised blend morphology, by the introduction of solvent additives for example, that can effectively modulate the molecular orientation and packing of the BHJ blend.<sup>46</sup> Based on their chemical structure, solvent additives are typically classified as non-conjugated or aromatic additives. 1,8-diiodooctane (DIO) is a widely used non-conjugated solvent additive that tends to increase the crystallinity of the active layer. 1-chloronaphthalene (CN), tends to increase the miscibility of the OS materials.<sup>47, 48</sup>

Lastly the interfacial energetics in the device are important, including the interface with the electrodes to enable effective charge extraction. A strategy to enhance charge extraction in OPV devices, involves the use of a multilayer stack where the active layer is sandwiched between an ETL and a hole transport layer (HTL) prior to the addition of electrodes on either side. Typical multi-layered stacks for OPVs are shown in Figure 10. ETLs and HTLs, can serve different functions. They can be used to modify the interfacial energetics of the device<sup>49</sup> by matching and controlling the work function of different components and thus increase the built-in field,<sup>50</sup> and/or form ohmic contacts,<sup>51</sup> to name but a few examples. Ultimately, their common purpose is to facilitate charge transport and extraction.

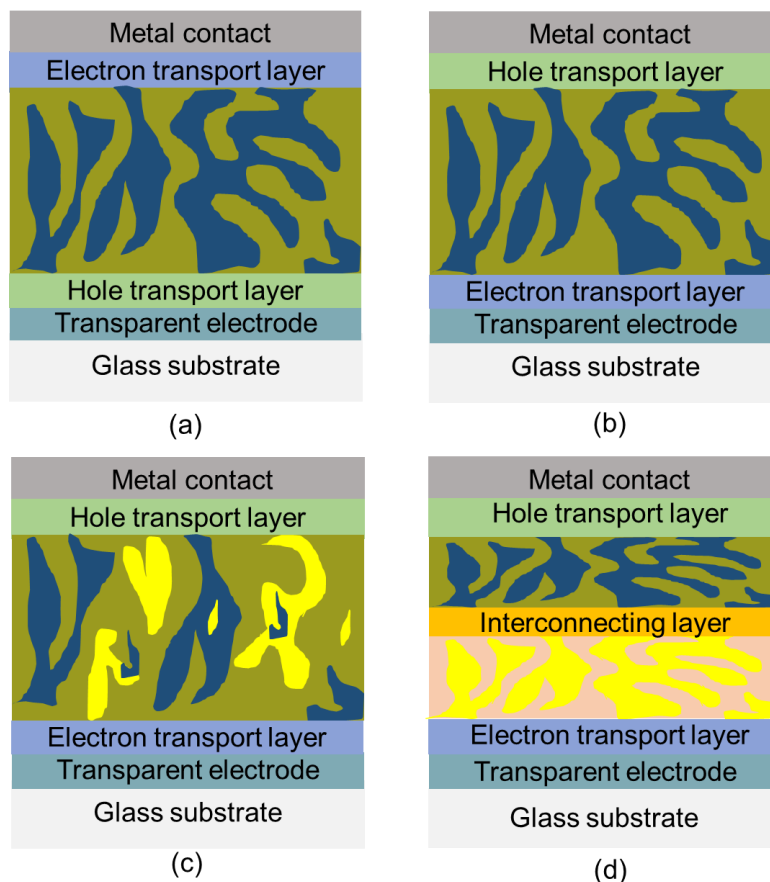


Figure 10. Typical multilayer stack for the (a) standard OPV architecture, (b) inverted OPV architecture, (c) ternary blend OPV architecture, (d) tandem OPV architecture.

### Ternary and tandem organic photovoltaics

After the advent and consolidation of the BHJ concept, by the year 2000, fullerenes, and especially the soluble derivatives [6,6]-phenyl-C<sub>61</sub>-butyric acid methyl ester (PC<sub>60</sub>BM) and [6,6]-Phenyl-C<sub>71</sub>-butyric acid methyl ester (PC<sub>70</sub>BM - Figure 11), became the "elective" acceptors mainly due to their ability to form effective BHJs.<sup>52</sup> In the years 2000 - 2015 the efforts of the scientific community were therefore directed to the careful optimisation of the morphology of active layers via solvent additives and annealing, the development of interlayers and most importantly, the synthesis of high-mobility and strongly absorbing donors for which there is currently a very large palette to choose from.<sup>53-56</sup> This effort

successfully led to PCEs exceeding 10%.<sup>57</sup> Some other key developments in the field of OPVs overtime consisted of the inverted OPV structure, the use of ternary blends as the active layers and the concept of a tandem OPV. The device architectures resulting from these concepts are shown in Figure 10. The benefit of the inverted structure is related to the stability of the device. The typical materials used for hole extraction in standard architectures are Indium tin oxide/poly(3,4-ethylenedioxythiophene) polystyrene sulfonate (ITO/PEDOT:PSS) in combination with a low work function metal cathode for electron extraction. Replacing these with MoO<sub>3</sub>/Au or MoO<sub>3</sub>/Ag for hole extraction and a metal oxide for electron extraction instead, avoids the use of the low work function metals that are more easily oxidised, hence inverted devices can offer similar efficiencies but with the added benefit of increased stability.<sup>58</sup>

Ternary blends involve the formation of an active layer via the use of three materials, either two donors and an acceptor or two acceptors and a donor. The typical benefits resulting from the addition of a third component include the enhancement of the light-harvesting ability (by selecting materials with complementary absorption to increase the absorption window of the active layer) and the optimization of the morphology of the active layer.<sup>59, 60</sup> Two common strategies are typically used to select the third active component of the blend. The first strategy involves constructing a cascade-like energy level alignment between the three components; hence the third component is selected to have LUMO and HOMO levels lying between the LUMO and HOMO levels of the “host donor” and “host acceptor”. This enables efficient charge transport in the ternary

blend. The second strategy is the formation of a so-called alloy-like composite. In this case, the acceptors are selected to have a similar structure and good compatibility resulting in a system that works like a single material. The properties of the composite, including energy levels and crystallinity, can be continuously adjusted via a change of ratios of the two acceptors, hence the alloy-like model can be used to achieve morphology optimization.<sup>61</sup> Tandem solar cells can be used to counter thermalisation losses by using one active layer blend (consisting of a large band gap material) to absorb high energy photons and the other active layer blend to absorb low energy photons.

Ternary blends and tandem structures are particularly useful for OPVs, as the absorption and coverage of the solar irradiation spectrum is not optimal in single junction donor:acceptor BHJs due to the relatively narrow optical absorption of OS and relatively low mobilities that require active layers of limited thickness compared to inorganic semiconductors such as silicon for example.

### **Non-fullerene acceptor organic photovoltaics**

In the year 2015 the innovation of NFAs re-ignited the scientific effort in the field of OPVs. NFAs have enabled OPVs to reach new levels of performance with PCEs now exceeding 18%.<sup>38</sup> The limited tunability of the electron affinities of fullerenes<sup>52</sup>, which in turn limits the number of potential donor materials that can be utilised and more importantly the weak absorption in the visible and near infra-red regions, which limits the maximum value of short circuit current densities restricted attainment of efficiencies above ~ 12% for single junction OPVs based on donor:fullerene blends. Furthermore, although there is evidence that the

crystallinity of the fullerene phase influences OPV performance this lacks optimisation since the crystal phase depends on the solvent and is difficult to characterise.<sup>62, 63</sup> These drawbacks motivated the development of strongly absorbing NFAs.<sup>64</sup> Combining these NFAs with donors having complementary absorption features, allows for a significant  $J_{SC}$  boost.<sup>65, 66</sup>

In NFAs, energy levels and absorption spectra can be tuned more easily than in the case of fullerenes so as to optimise device function and charge transfer from excited states formed both in the donor and the acceptor can occur effectively in NFA blends.<sup>67, 68</sup> NFAs are split into 3 main classes, based respectively on:

- (1) perylene diimides
- (2) diketopyrrolopyrrole
- (3) acceptor–donor–acceptor (A-D-A) NFAs

A-D-A type NFAs have been most successful and consist of an electron-rich core (D) flanked with two electron deficient terminals (A). The D and A parts can be modified separately to fine-tune the energy levels, bandgap, molecular packing, and other properties.<sup>69, 70</sup> Many “top-performing” A-D-A NFA molecules have been developed in recent years with the most successful ones being ITIC-2F,<sup>71</sup> Y6,<sup>72</sup> (see section 3.1 for full chemical names and structures) and 2,2'-[[4,4,11,11-tetrakis(4-hexylphenyl)-4,11-dihydrothieno[2',3':4,5]thieno[2,3-thieno[2''',3''':4''',5''']]thieno[2''',3''':4'',5'']pyrano[2'',3'':4',5']thieno[2',3':4,5]thieno[3,2-b]pyran-2,9-diyl]bis[methyldiylidene(5,6-difluoro (COi8DFIC)).<sup>73</sup> The development of ITIC-2F enabled a PCE of 13.1% beating any previous fullerene performance. In 2018, COi8DFIC-based tandem solar cells delivered a PCE of ~ 17.4%,<sup>74</sup>

setting a new record for the organic tandem cell. A-D-A type NFAs have a planar skeletal structure that enables for a high charge mobility through ordered  $\pi$ - $\pi$  stacking and the push-pull effect extends optical absorption to the near-infrared region.

The emergence of the so-called Y-series of acceptors is the latest impetus to further push forward OPVs. In Y-series acceptors, an electron-deficient benzothiadiazole is added to the donor core resulting in a banana shaped material. The first use of Y6 resulted to a PCE of 15.7% (when blended with donor PM6 (Table 1)) that was unprecedented at the time.<sup>72</sup> Synthetic difficulties associated to the monofunctionalization of the A building block meant that D-A-D molecules preceded A-D-A molecules, but nowadays the combination of the two arrangements to form molecules such as Y6, has induced the new wave in OPV research, with these NFAs separately classified as A-DA'D-A type NFAs.<sup>75, 76</sup> In 2020, Ding et al. blended Y6 with a wide-bandgap polymer donor poly[(2,6-(4,8-bis(5-(2-ethylhexyl-3-fluoro)thiophen-2-yl)-benzo[1,2-b:4,5-b']dithiophene))-alt-5,5'-(5,8-bis(4-(2-butyloctyl)thiophen-2-yl)dithieno[3',2':3,4;2'',3'':5,6]benzo[1,2,c][1,2,5]thiadiazole)] (D18) and achieved a PCE of 18.22%.<sup>38</sup> Strategies to increase the performance of donor:A-DA'D-A type OPVs, including formation of ternary blends are likely to bring even greater PCEs in the near future.

During the development of these significant advances in the last few years, great strides have also been achieved in developing the other layers of the multi-

layered OPV device beyond the active layer. This includes the optimisation of the ETLs and HTLs. Optimisation of interlayers can in fact be key to enable improvement in the performance and stability of NFA based OPV devices. Chemical reactions at interfaces can result in formation of charge traps that damage the conjugated structures of NFAs in the blend films, hence special attention needs to be paid to ensure that novel ETLs are compatible with NFAs.<sup>77</sup> Importantly, ETLs and HTLs find common use between the emerging PV technologies and are not just constricted to use in OPVs.<sup>78</sup> Hence novelties in ETLs for other solution-processed systems can be transferred to OPVs and vice versa enabling the synergistic push of the performance boundaries of these promising technologies to even higher levels.

In this thesis too, I leverage the significant developments in optimisation of ETLs for PSCs, and apply and adapt these to OPVs. Specifically the modification of SnO<sub>2</sub> with MgO that optimised ETLs for PSCs<sup>79</sup> has inspired the use of MgO to modify ZnO - the “elective” ETL for OPVs - as presented in chapter 4 and chapter 5.

### **2.2.3 Electron transport layers in organic photovoltaics**

In the case of inverted OPVs, a plethora of materials have been investigated for application as ETLs. A key example is the polymer poly[(9,9-bis(30-(N,N-dimethylamino)propyl)-2,7-fluorene)-alt-2,7-(9,9-dioctylfluorene)] known as PFN<sup>80</sup> that is used to reduce the work function of ITO. There are of course many other examples.<sup>81, 82</sup> The ideal ETL should not require high temperature processing to be effective, so as to be compatible with low temperature energy

saving manufacturing processes. The prevailing ETLs in inverted OPVs are semiconducting metal oxides since they have the combined ability to effectively extract/transport electrons due to their relatively high mobilities and at the same time offer good solution-processability, high optical transparency and good environmental stability.<sup>51</sup> However, to achieve long-term stability, metal oxide ETLs frequently require high temperature treatment (at ~ 300°C). These annealing temperatures are not favourable for industrial scale applications and may not be suitable where plastic flexible substrates are mandated by the application. In addition, avoiding the use of high temperature processing automatically increases the sustainability of the whole life cycle. For some applications, such as IOT devices that can be used to power smart packaging on supermarket shelves, high temperature annealing can be avoided since a long lifetime may not be required. In other cases where long lifetimes are necessary, judicious selection and engineering of the precursor materials or techniques such as UV-ozone treatment<sup>81</sup> have shown promise in prolonging the lifetime of devices based on metal oxide ETLs processed at low temperatures.

ZnO is one of the most widely used metal oxide ETLs.<sup>83, 84</sup> Indeed, ZnO has been the “elective” ETL for the latest state-of-the-art inverted OPV devices<sup>85, 86</sup> affording higher PCE than other metal oxides such as TiO<sub>2</sub>. There are a number of routes that enable the formation of a ZnO ETL such as atomic layer deposition,<sup>87</sup> pulsed laser deposition,<sup>88</sup> metal organic chemical vapor deposition,<sup>89</sup> spray pyrolysis and electrodeposition<sup>90</sup> but in most reports the facile sol-gel spin-coating method is used.<sup>83, 84</sup> Sol-gel ZnO, usually requires an

annealing treatment upon deposition at a temperature of  $\sim 300^{\circ}\text{C}$  so as to completely decompose the zinc acetate precursor and form a crystalline ZnO structure. Lower temperature treatments have also been implemented and resulted to reasonable stability. For example, Sun et al. fabricated devices using ZnO ETLs processed at 130 and  $150^{\circ}\text{C}$  that retained 70% of the PCE after exposure in air at room temperature for more than 30 days and without encapsulation.<sup>91</sup> In addition, low-temperature processed ZnO ETLs have been reported to outperform (in terms of PCE) ZnO ETLs annealed at higher temperatures.<sup>92-94</sup>

Nevertheless, solution-processed ZnO is a sub-optimal ETL. ZnO drawbacks include surface defects (formed by excess zinc at the interstitial position or oxygen vacancies in ZnO films) that can act as electron trap sites and result in severe charge recombination losses.<sup>95, 96</sup> In addition, given the large number of different acceptor materials that have been developed for use in active layers of OPVs, having some degree of control over the properties of the ZnO ETL such as its work function or conductivity, so as to tailor it for the specific active layer blend has become crucial. To this end, three main strategies have been developed over time to remedy the shortcomings of ZnO ETLs and to enable control of its properties. One possibility is the treatment of the deposited ZnO with UV-ozone.<sup>97, 98</sup> This is similar to oxygen-plasma treatments that are usually applied to ITO electrodes to increase their work function, smooth surfaces and increase their surface polarity.<sup>99</sup> UV-ozone treatment can also adjust a layer's work function. Another effective strategy is to apply a modifying interlayer

between ZnO and the active layer. The final strategy involves the direct addition of dopants in the precursor solution of the ZnO ETL to form doped ZnO ETLs.

In general the modification of an ETL, can lead to an increase in PCE that is associated with one (or more) of the following mechanisms:<sup>95</sup>

(1) An improved rate of photon capture which depends strongly on the transmittance of the semi-transparent cell electrode.

(2) A favourable change in the active layer blend morphology leading to higher exciton dissociation.

(3) A change in the interfacial properties of the ETL:

- Fewer recombination sites and reduced alternative current paths (lower leakage current).
- Increased blocking of undesired hole currents in the ETL.
- A change in the interfacial energetics of the interface between the ETL and blend (an improved energy level alignment) by a variation of the ETL's work function (leading to higher charge extraction).

In chapters 4 and 5 of this thesis, MgO is used to modify ZnO ETLs formed by simple solution-processing and low temperature annealing (150°C). In chapter 4, the modification involves the formation of a bilayer ZnO/MgO ETL, whereas in chapter 5, the modification is via the doping of ZnO with MgO. In these chapters, I present evidence to help establish which of the above mechanisms occur when MgO is present in devices and identify the origin of the success of MgO as a modifier for ZnO ETLs applied to OPVs.

# 3 Experimental techniques

## 3.1 Materials and fabrication methodologies

The full chemical names and chemical structures of the materials used as active layers for the thesis can be found in Table 1 and Figure 11.

Table 1. Full chemical names of materials used in active layers for this thesis

(a)	PTB7-Th	Poly[4,8-bis(5-(2-ethylhexyl)thiophen-2-yl)benzo[1,2-b;4,5-b']dithiophene-2,6-diyl-alt-(4-(2-ethylhexyl)-3-fluorothieno[3,4-b]thiophene-)-2-carboxylate-2-6-diyl]
(b)	PC <sub>70</sub> BM	[6,6]-phenyl-C71-butyric acid methyl ester
(c)	PM6	Poly[(2,6-(4,8-bis(5-(2-ethylhexyl-3-fluoro)thiophen-2-yl)-benzo[1,2-b:4,5-b']dithiophene))-alt-(5,5-(1',3'-di-2-thienyl-5',7'-bis(2-ethylhexyl)benzo[1',2'-c:4',5'-c']dithiophene-4,8-dione))
(d)	Y6	2,2'-((2Z,2'Z)-((12,13-bis(2-ethylhexyl)-3,9-diundecyl-12,13-dihydro-[1,2,5]thiadiazolo[3,4-e]thieno[2'',3'':4',5']thieno[2',3':4,5]pyrrolo[3,2-g]thieno[2',3':4,5]thieno[3,2-b]indole-2,10-diyl)bis(methanylylidene))bis(5,6-difluoro-3-oxo-2,3-dihydro-1H-indene-2,1-diylidene))dimalononitrile
(e)	ITIC-2F	3,9-bis(2-methylene-((3-(1,1-dicyanomethylene)-6,7-difluoro)indanone))-5,5,11,11-tetrakis(4-hexylphenyl)-dithieno[2,3-d:2',3'-d']-s-indaceno[1,2-b:5,6-b']dithiophene
(f)	F8BT	Poly(9,9-dioctylfluorene-alt-benzothiadiazole

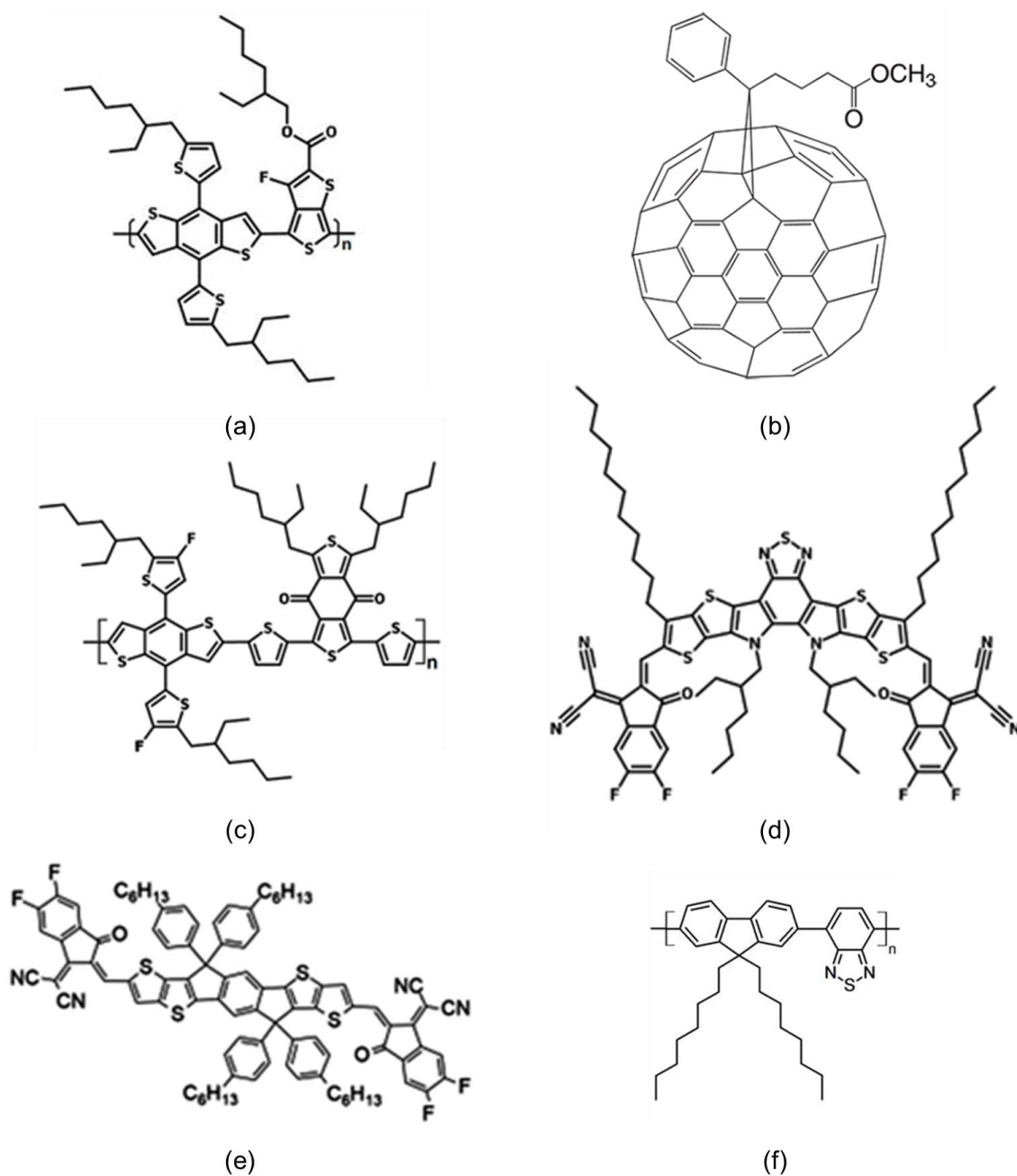


Figure 11. Chemical structures of materials used in the thesis. (a) PTB7-Th, (b) PC<sub>70</sub>BM, (c) PM6, (d) Y6, (e) ITIC-2F, (f) F8BT. See Table 1 for full chemical names.

The above materials were purchased from Ossila. Additionally, zinc acetate dihydrate, 2-methoxyethanol, ethanolamine, magnesium acetate tetrahydrate, tin chloride dihydrate, CN, PEDOT:PSS, chloroform, ethanol, acetone, isopropanol

and toluene were purchased from Sigma Aldrich. Chlorobenzene was purchased from Acros organics and DIO was purchased from Alfa Aesar. Evaporation materials Au, Ag, Ca, Al and MoO<sub>3</sub> were purchased from Kurt J. Lesker. Glass/ITO substrates were purchased from Ossila.

The full details of the solution preparation of the above materials and device fabrication methodologies can be found in the experimental sections of each of the subsequent chapters. In general, standard practices and techniques have been used, such as the use of a nitrogen glovebox to avoid material degradation, spin-coating for the deposition of solutions, ultra-sonication for cleaning substrates, and the use of a thermal evaporator (housed in the nitrogen glovebox) for formation of top contacts.

## **3.2 Device characterisation**

### **3.2.1 Current density–voltage measurements**

Current density–voltage characteristics under illumination and in darkness, were obtained using a source measure unit (SMU) (Keithley 2400) and a class AAA solar simulator (ABET Technologies, model Sun 3000 11016A). For measurements under illumination, the output of the lamp was calibrated to 1 Sun using a standard calibrated Si photodetector. The  $J_{sc}$ ,  $V_{oc}$ , FF and PCE were extracted from the current density-voltage curve.

Dark curves were analysed further to extract the shunt resistance ( $R_{SH}$ ) following the procedure described by Brus et al.<sup>100</sup> The modified ideal diode equation

(equation (3)) that includes a component for  $R_{SH}$  and series resistance ( $R_S$ ) (often used to model inorganic semiconductors) in the dark was used.

$$J = J_0 \left( \exp \left( \frac{q(V - JR_S)}{nkT} \right) - 1 \right) + \frac{V - JR_S}{R_{SH}} \quad (3)$$

where  $J$  is the current density,  $J_0$  is the saturation current density,  $V$  is the voltage,  $n$  is the ideality coefficient,  $R_S$  is the series resistance and  $R_{SH}$  is the shunt resistance. The  $R_{SH}$  can be determined from the voltage dependence of the differential resistance  $dV/dJ$  (note that the units are  $\Omega\text{cm}^2$ ), where the value of the  $R_{SH}$  is equal to the differential resistance in the vicinity of zero bias as shown in Figure 12. The extraction of the  $R_S$  from the plot is not attempted. As discussed by Servaites et al.<sup>101</sup> the above model assumes that the  $R_S$  is independent of electric field strength, an assumption that breaks down at high fields due to the field-dependent conductivities in OS, complicating the accurate determination of  $R_S$  in OPVs.

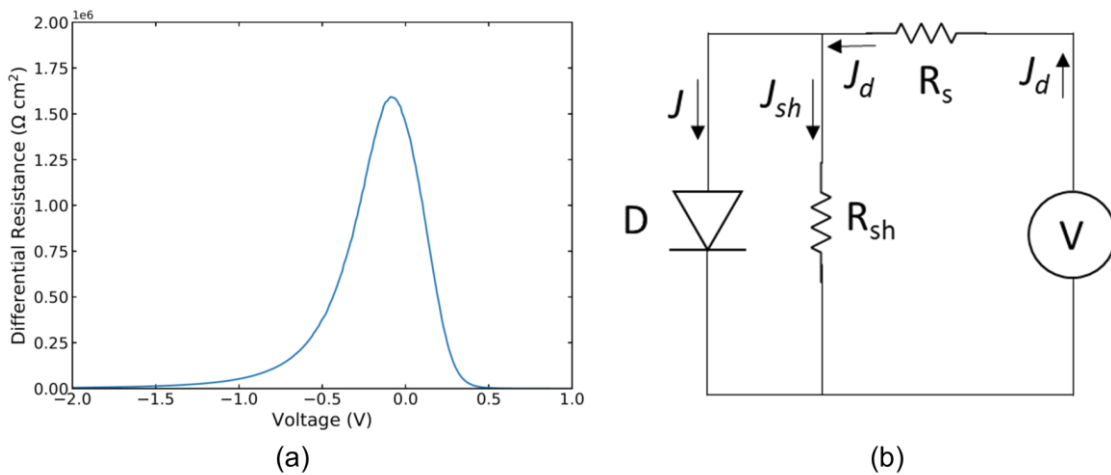


Figure 12. (a) Example of a differential resistance vs. voltage plot used to extract  $R_{SH}$ . (b) The equivalent circuit used to model OPV devices when operated in the dark. An increased  $R_{SH}$  leads to a reduction in the leakage (reverse bias) current of the devices.

The dependence of the photocurrent density ( $J_{PH}$ ) on the effective voltage ( $V_{EFF}$ ) is also extracted using the current-density voltage curves under illumination and in darkness. The  $J_{PH}$  and  $V_{EFF}$  can be calculated using equation (4) and equation (5).

$$J_{PH} = |J_L - J_D| \quad (4)$$

where  $J_L$  and  $J_D$  are the measured photocurrents under light and in the dark.

$$V_{EFF} = V_0 - V_a \quad (5)$$

where  $V_a$  is the externally applied voltage and  $V_0$  is the (externally applied) voltage at  $J_{PH} = 0$ . The extraction of  $J_{PH}$  at saturation ( $J_{PH,SAT}$ ) which occurs at high  $V_{EFF}$  (where the device is in reverse bias) as well its extraction at short circuit ( $J_{PH,SC}$ ) allow for the calculation of a quantitative performance indicator. Such an indicator is the ratio  $J_{PH,SC}/J_{PH,SAT}$  ( $P_{DISS}$ ) which some authors consider akin to the relative exciton dissociation efficiency.<sup>102-104</sup> Since such a parameter is calculated as a ratio of collected currents it will not account for any recombination event taking place even at the strongest fields applied “in saturation” (as specified above). It does however provide information on the effectiveness with which dissociated excitons are extracted.

### 3.2.2 Open circuit voltage decay and rise measurements

$V_{OC}$  rise/decay measurements were performed by connecting the PV devices to a Tektronix TD oscilloscope. The aforementioned solar simulator was used for switching the light incident on the device from the dark to 1 Sun and the oscilloscope was used to record the complete ON/OFF signal trace. The decay/rise times, are calculated as the time it takes for the  $V_{OC}$  to move from 10% to 90% of its final value and vice versa.

### 3.2.3 External quantum efficiency measurements

EQE spectra were obtained using a home-built system that employs a monochromated xenon lamp. The incident power is extracted via the use of a calibrated Bentham DH-Si photodiode connected to an amplifier. The outputs from the photodiode-amplifier combination and current from the device under test are recorded with Keithley 2400 SMUs.

The readings from the SMUs are then analysed as follows to extract the EQE: Firstly, any signal offset present in the dark is removed. To convert the voltage reading from the photodiode-amplifier combination to incident power, voltage values are initially converted to current by division with the value of the amplifier gain. Then the data are divided by the response curve of the photodiode as provided by its manufacturer to obtain the incident power spectrum.

The incident power spectrum and current from the device under test at each wavelength are then divided by the relevant device area to obtain the power density and current density spectra. The EQE is extracted using equation (6).

$$EQE(\lambda) = \frac{1241 \times J}{\lambda \times P_{PD}} \quad (6)$$

where 1241 accounts for the constants and unit conversions ( $\frac{hc}{e} \times 10^9$ ),  $\lambda$  is the wavelength (nm) and  $P_{PD}$  the incident power density. It is best practice to cross-check that the measured EQE provides an accurate prediction of the  $J_{SC}$  of the device. To calculate the expected  $J_{SC}$  from EQE data, equation (7) can be used

$$J_{SC} = \int \frac{EQE(\lambda) P_{sun}\lambda}{1241} d\lambda \quad (7)$$

where  $P_{sun}$  is the typical 1 Sun spectrum.

### 3.2.4 Electroabsorption spectroscopy measurements

In electroabsorption spectroscopy the variation in the absorption spectrum of a system of interest due to the application of a modulating electric field is investigated. More specifically the normalised variation of light transmitted through a sample upon application of a periodic electric field is measured, probing the manifestation of non-linear optical effects. Since changes in absorption are minute, phase sensitive detection is employed. The schematic of the home-built apparatus used to perform the measurement is shown in Figure 13.

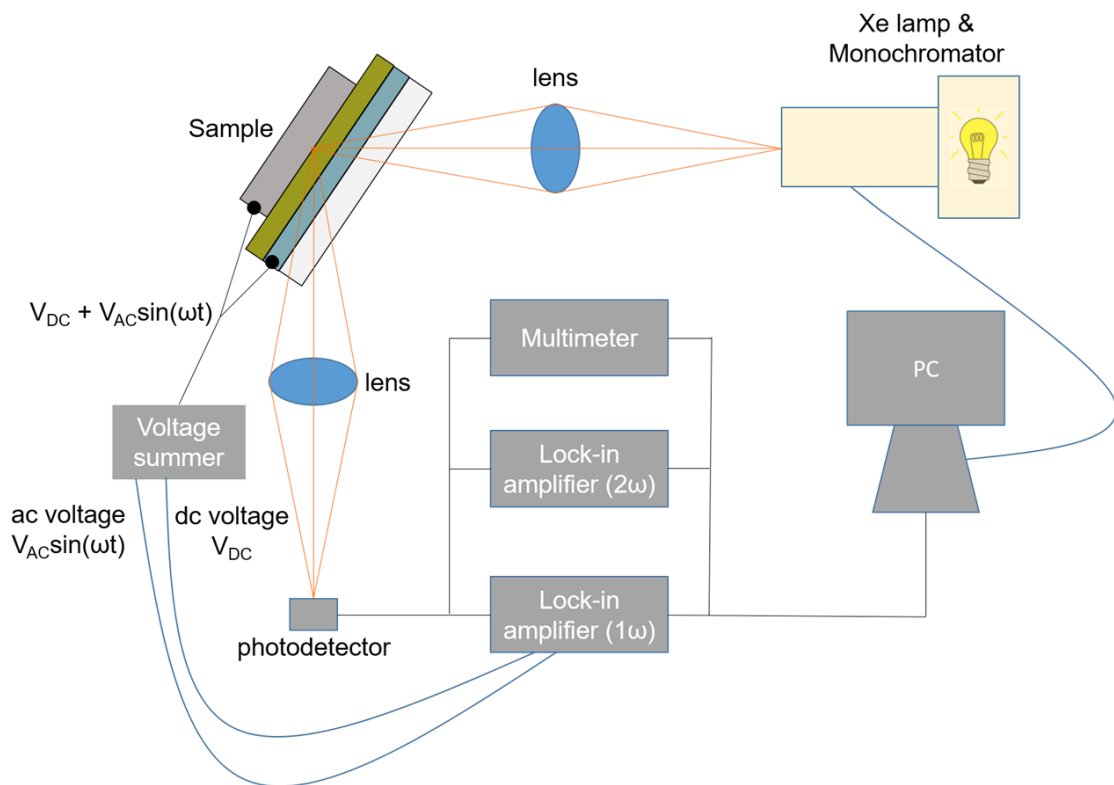


Figure 13. Schematic of the home-built EA set-up used in the investigations.

Light of selected wavelength from the Xenon lamp/monochromator system is reflected by the sample and is then detected via the use of a photodetector. The equipment allows for both a DC ( $V_{DC}$ ) and a periodic AC ( $V_{AC}$ ) voltage to be applied on the sample. This voltage is generated by the lock-in amplifier, which uses the same periodic signal as reference to enable phase sensitive detection. The lock-in amplifier records the change in transmission of the incoming beam through the sample ( $\Delta T$ ) and a multimeter the overall transmission ( $T$ ). The EA signal is then calculated by equation (8).

$$EA = \frac{\Delta T}{T} \quad (8)$$

The set-up is equipped with lock-in amplifiers set to measure the signal at two frequencies ( $\omega$ ). The first lock-in is set at the first harmonic ( $1\omega$ ) whilst the second at the second harmonic ( $2\omega$ ).

Considering the transmitted intensity ( $I_T$ ) through a sample (ignoring multiple reflections and interference effects) equation (9) can be derived.

$$I_T = I_0(1 - R)^2 e^{-ad} \quad (9)$$

where  $I_0$  is the incident intensity,  $R$  the reflection coefficient,  $a$  the absorption coefficient and  $d$  the sample thickness. By the application of an electric field ( $F$ ), a change is induced on both the absorption and reflection coefficients.

Equation (10) shows the change in transmitted intensity due to the applied field.

$$\frac{\partial I_T}{\partial F} = -I_0 d (1 - R)^2 e^{-ad} \frac{\partial a}{\partial F} - I_0 2(1 - R) e^{-ad} \frac{\partial R}{\partial F} \quad (10)$$

Dividing equation (10) by equation (9) the resulting normalised change in transmission is calculated in equation (11).

$$\frac{\frac{\partial I_T}{\partial F}}{I_T} = -d \frac{\partial a}{\partial F} - \frac{2}{1-R} \frac{\partial R}{\partial F} \quad (11)$$

Changing the notation to  $I_T = T$  and  $\frac{\partial I_T}{\partial F} = \Delta T$  and ignoring the change in intensity caused by the field-induced change of the reflection coefficient (a valid approximation for the set-up employed) equation (12) is derived.

$$\frac{\Delta T}{T} \cong -d\Delta a \quad (12)$$

where  $\Delta a$  is the field-induced change in the absorption coefficient. Hence, it can be concluded that the normalised change in the transmitted intensity that is measured with the EA set-up, corresponds to the field induced variation in the absorption coefficient of the tested sample.

For the case of OS where excitons are bound, the response of the system of interest in the field can be modelled using the framework of Stark's shift theory. Within this framework, the EA signal is expected to have a quadratic dependence with respect to the applied electric field. Since the field in the device is induced by the application of a potential with the form  $V_{DC} + V_{AC} \sin(\omega t)$ , the resulting field in the device has the form shown in equation (13).

$$F_0 + F_{AC} \sin(\omega t) \quad (13)$$

where  $F_0 = \frac{V_{DC} - V_{BI}}{d}$  considering the built-in voltage ( $V_{BI}$ ) formed in the device from the presence of electrodes. Hence, due to the quadratic dependence a modulation appears at frequency  $1\omega$  and  $2\omega$  as shown by equation (14).

$$\frac{\Delta T}{T} \propto F_0^2 + \frac{F_{AC}^2}{2} + 2F_0F_{AC} \sin(\omega t) - \frac{F_{AC}^2}{2} \cos(2\omega t) \quad (14)$$

For the case of a fixed frequency these two components can be written out individually:

$$EA_{(1\omega)} = \frac{\Delta T}{T_{(1\omega)}} \propto (V_{DC} - V_{BI})V_{AC} \quad (15)$$

$$EA_{(2\omega)} = \frac{\Delta T}{T_{(2\omega)}} \propto \frac{V_{AC}^2}{2} \quad (16)$$

The  $V_{DC}$ ,  $V_{AC}$  and frequency that dictate the electric field in the sample as well as the wavelength of light incident on it are parameters that can be controlled in the EA set-up. To demonstrate the accurate operation of the home-built system and that the above theory holds, measurements were performed on a device consisting of the polymer poly(9,9-dioctylfluorene-alt-N-(4-sec-butylphenyl)-diphenylamine) (TFB) sandwiched between ITO and Ca/Al electrodes. The results from the measurements are shown in Figure 14.

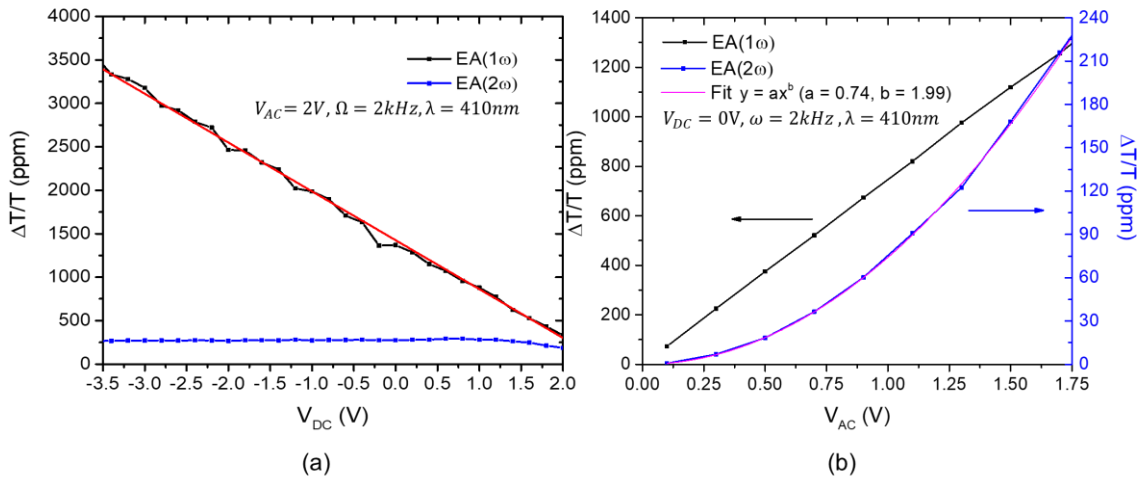


Figure 14. Verification of Stark's shift theory predictions and the accurate operation of the experimental apparatus. The parameters of the fit in (b) are  $a = 0.74 \pm 0.01$  and  $b = 1.99 \pm 0.01$ .

The R-square value of the fit is 0.999.

In the case of the second harmonic signal  $EA(2\omega)$ , no  $V_{DC}$  dependence is observed in Figure 14 (a), with the value of the EA signal remaining constant throughout the measurement. By fitting the  $V_{AC}$  dependent second harmonic signal with an equation of the form  $y = ax^b$  (Figure 14 (b)), equation (16) is verified and the  $V_{AC}$  dependence of the second harmonic is shown to be quadratic. In the case of the first harmonic signal  $EA(1\omega)$ , both the  $V_{AC}$  and  $V_{DC}$  dependencies are shown to be linear as expected from equation (15).

PV devices can be characterised using EA spectroscopy to gain insight into a number of properties of the device, for example, to calculate the binding energy of the photoinduced charges in the active layer.<sup>105</sup> In this thesis the EA spectroscopy set-up has been solely used to determine the change in built-in voltage of devices caused by variations in the ETL hence only first harmonic signals are reported. As shown in equation (15), for a nulled EA signal,  $V_{BI}$  equals the applied  $V_{DC}$ . Hence, by studying the variation of the  $EA(1\omega)$  signal with  $V_{DC}$ , the  $V_{BI}$  of a device can be extracted at the point where the EA signal intersects with the  $\Delta T/T = 0$  line. The above analysis assumes that there are no interfering spectral contributions (e.g., from permanent dipole moments possibly associated to polar molecules). To confirm this is the case, it is best practice to plot wavelength dependent EA spectra with different applied DC and AC voltages and show that the isosbestic points always intersect at the point where the EA signal is nulled as in Figure 15. Such measurements have been undertaken for all studies presented in the thesis.<sup>106</sup> The wavelength dependent EA spectra are also used to determine the fixed incident light wavelength of choice for the

investigations to extract the  $V_{BI}$ . A wavelength near the peak EA value is selected so as to reduce noise in these investigations.<sup>107</sup>

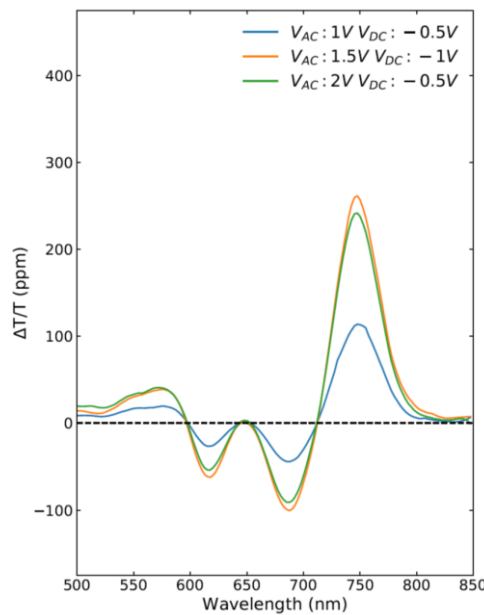


Figure 15. Representative examples of incident light wavelength dependent EA measurements used to determine the wavelength of choice and to test the validity of extracting the built-in voltage in the  $V_{DC}$  dependent investigations. In the above example, an ITO/ZnO/MgO(10 nm)/PTB7-Th:PC<sub>70</sub>BM/Au device is characterised. Note the isosbestic point occurrence at points where the EA signal is null.

## 3.3 Sample characterisation

### 3.3.1 Kelvin probe

The Kelvin probe measurement involves the arrangement of a capacitor circuit between an oscillating gold tip with a known work function and a surface whose work function is to be measured. The difference between the work function levels, leads to a contact potential difference between the tip and sample that is nulled by application of an external bias. Extraction of the voltage where nulling occurs

enables the measurement of the sample's surface work function. The working principles of the technique are demonstrated in Figure 16. A Besocke DeltaPhi Kelvin probe was used for the measurements, which were performed in darkness to avoid any light induced effects. The measurements are corrected by using as reference a freshly-cleaved highly oriented pyrolytic graphite (HOPG) sample that has a known work function of  $4.475 \pm 0.005$  eV.

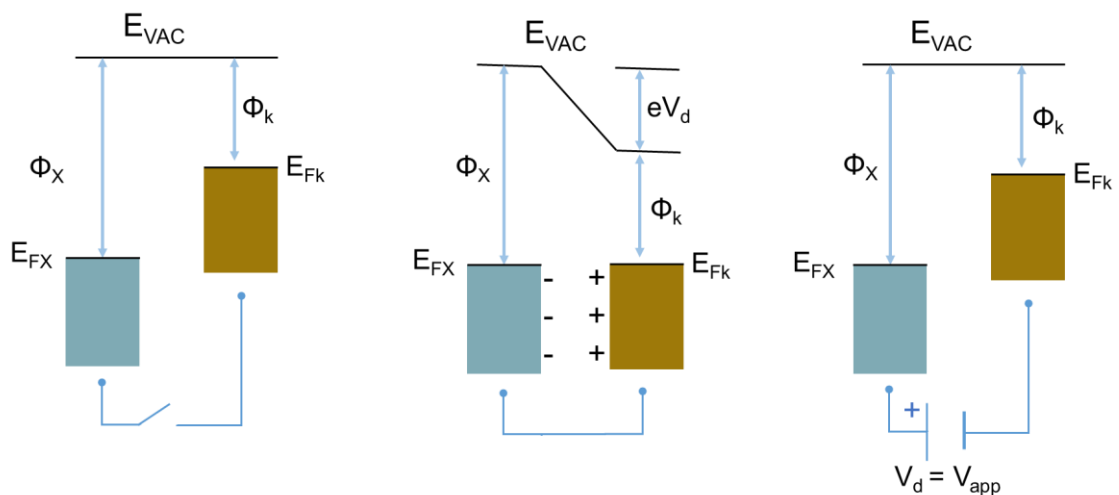


Figure 16. The Kelvin probe measurement.  $E_{FX}$  and  $\Phi_X$  correspond to the Fermi level and work function of the sample under investigation whilst  $E_{FK}$  and  $\Phi_K$  to the Fermi level and work function of the oscillating tip. When the materials form a capacitor circuit, electrons flow from the low work function material to the high work function material setting up a potential difference  $V_d$ .  $eV_d$  corresponds to the work function difference between the surfaces of the two materials. To extract  $eV_d$ , an external bias  $V_{app}$  is applied until the potential difference is nulled where  $V_d = V_{app}$ . The work function of the surface of the material of interest is then calculated by addition of  $eV_{app}$  to the known work function of the oscillating tip.

### 3.3.2 UV-VIS absorption spectroscopy

Transmission measurements were carried out by using an Agilent 8453 UV-VIS spectrophotometer. The measurements for deposited materials were corrected

by subtracting the spectrum of the corresponding glass substrate (on which the material was deposited).

### **3.3.3 Profilometry**

The thickness of different layers was measured using a Dektak 3 profilometer (Veeco Instruments Inc).

### **3.3.4 Atomic force microscopy**

Atomic force microscopy (AFM) images were captured with a Bruker Dimension Icon atomic force microscope, in peak force tapping mode with a ScanAsyst® cantilever (Bruker). Images were then analysed using Gwyddion. The uncertainty on the root mean square roughness ( $S_q$ ) is the standard deviation calculated on a set of two areas (of size  $1.6 \mu\text{m} \times 1.6 \mu\text{m}$ ) on two different samples of each type. For conductive AFM images, contact mode measurements were performed using a SCM-PIT-V2 tip. The sample was attached to a conductive plate and a conductive pathway was formed from the instrument to the sample using silver paste.

## **3.4 Measurements carried out by partners**

### **3.4.1 X-ray photoelectron spectroscopy (XPS) and ultraviolet photoemission spectroscopy (UPS)**

XPS and UPS measurements were performed by Dr. Giovanni Ligorio at Institut für Physik, Institut für Chemie & IRIS Adlershof, Humboldt-Universität zu Berlin. XPS was performed in a JEOL JPS-9030 photoelectron spectrometer system using the Al  $K\alpha$  (1486 eV) excitation source (a monochromator was employed). The samples were grounded during the photoemission measurements. UPS was

performed in an Omicron system equipped with a hemispherical energy analyser (SPECS Phoibos 100) using the He I emission (21.2 eV) as excitation source with an 80% intensity aluminium filter. The samples were grounded during the measurements of the valence band region while a bias of -10 V was applied to the samples during the measurements of the work function calculated through the secondary electron cut off (SECO).

### **3.4.2 Hall measurements**

Van der Pauw and Hall measurements were carried out on a Lakeshore 8404 Hall Measurement System by Prof. Martyn A McLachlan at the Department of Materials and Centre for Processable Electronics of Imperial College London. Contacts were confirmed ohmic (linear I-V plot) prior to carrying out any measurements. The Van der Pauw technique was used to obtain the thin film sheet resistance. Hall measurements were carried out using a DC magnetic field of 1T.

# 4 ZnO/MgO bilayer electron transport layers

## 4.1 Introduction

The application of a thin or ultrathin interlayer between ZnO and the active layer to form a bilayer ETL has proven to be a simple and effective method to improve ZnO-based inverted OPVs through various mechanisms. For example, Abd-Allah et al.<sup>108</sup> employed a carboxylic acid as the modifying interlayer that decreased the work function of the ETL by ~ 0.4 eV (from 4.5 to 4.1 eV), and boosted both the  $J_{sc}$  and FF with respect to devices based on a single ZnO ETL leading to a relative increase in PCE by 20%. Another example is the study by Wang et al.<sup>95</sup> where a ZnO/In ETL nanojunction is formed by vacuum deposition of indium films (~ 1 nm thick) on ZnO. The formation of the nanojunction, reduces recombination in devices by filling up electron trap sites that usually exist on ZnO-only ETLs (formed due to surface defects). The modification of ZnO with the Indium films, also creates an energy cascade from the fullerene component (PC<sub>70</sub>BM – LUMO (- 4.1 eV)) to a formed In<sub>2</sub>O<sub>3</sub> top surface (work function – 4.1 eV) to the ZnO/In nanojunction (work function – 4.15 eV) which facilitates carrier transport and extraction. An increase in  $J_{sc}$  and the FF has also been achieved by the passivation of traps on the surface of ZnO through the formation of bilayer ETLs with MoS<sub>2</sub> quantum dots,<sup>96</sup> poly(vinylpyrrolidone) and polyethylene glycol,<sup>98</sup> calcium fluoride<sup>109</sup> and solid alcohol 1-pyrenemethanol<sup>110</sup> serving as the modifying interlayers. Other interlayers such as a pyrene BODIPY molecular

dye<sup>111</sup> and commercially available dispersants (solutions of an alkylammonium salt of a polyfunctional polymer) D181 and D187<sup>112</sup> applied between ZnO and the active layer, optimised the active layer morphology. Recently, it has been demonstrated that biomaterials such as DNA<sup>113</sup> and processed spinach leaves<sup>114</sup> can serve as effective modifying interlayers in bilayer ZnO ETLs. In all the above cases the use of a bilayer ETL led to enhanced PCEs when compared with a single ZnO ETL.

An effective material used as interlayer in combination with SnO<sub>2</sub> to form bilayer ETLs for solution-processed PVs is MgO. Dagar<sup>79</sup> and collaborators for example demonstrated SnO<sub>2</sub>/MgO bilayer ETLs in CH<sub>3</sub>NH<sub>3</sub>PbI<sub>3</sub> PSCs reaching efficiencies up to 19% under 1 Sun illumination. This represented an increase of ~ 20% compared to the single SnO<sub>2</sub> ETL that was attributed to an improved ETL film quality as the presence of MgO removed pinholes on the SnO<sub>2</sub> surface, and to a reduced interfacial carrier recombination (most likely a result of the hole blocking ability of MgO due to its high ionization potential of around 10 eV). Similarly, Han et al.<sup>115</sup> employed a TiO<sub>2</sub>/MgO bilayer ETL improving the PCE by ~ 10% compared to the single TiO<sub>2</sub> ETL. The use of a bilayer ETL incorporating MgO as a top component (and thus in contact with the active layer) has also been demonstrated in systems beyond CH<sub>3</sub>NH<sub>3</sub>PbI<sub>3</sub> perovskites. Jayaweera et al.<sup>116</sup> used an SnO<sub>2</sub>/MgO ETL to form CdS nanosheet sensitized PVs. This study was preceded by the study of Docampo et al.,<sup>117</sup> where an SnO<sub>2</sub>/MgO bilayer ETL was applied to both solid state and electrolyte dye sensitised solar cells leading to a tripling and almost doubling of the PCE for the two cases respectively,

compared to their single SnO<sub>2</sub> ETL counterparts. In the study by Docampo et al., transient photovoltage and charge collection measurements were employed to demonstrate that the presence of MgO favourably shifts the conduction band edge of the ETL by 200 mV, thereby partly enabling the increase in  $V_{oc}$ , hence increasing performance. It is important to note that the mechanism by which the bilayer MgO based ETL facilitated the performance enhancement with respect to having a single ETL, differs in each of the above instances and necessitates a separate investigation in each case to uncover it.

MgO has a very high ionisation potential ( $\sim 10$  eV) and an insulating nature.<sup>115</sup> These characteristics may serve to block undesired hole currents flowing through the electron-collecting electrode and reduce recombination in OPV devices. The question which therefore arises and is investigated in this work, is whether MgO could be applied effectively as a modifying interlayer in ZnO ETLs for OPVs so as to increase their performance. The use of an MgO interlayer for OPVs has not been reported previously, with the exception of a recent publication<sup>118</sup> that uses a different device architecture, FTO/MgO/ZnO, for electron extraction (with the MgO not in direct contact with the active layer but “buried” below the ZnO film).

## **4.2 Experimental details**

### **4.2.1 Solution preparation**

The PTB7-Th:PC<sub>70</sub>BM blend precursor solution was formed by initially dissolving 15 mg of PTB7-Th in 1.5 mL chlorobenzene mixed with 45  $\mu$ L of DIO. The solution was stirred at 70°C for 4 hours. Then 22.5 mg of PC<sub>70</sub>BM were added to yield a 25 mgmL<sup>-1</sup> concentration with blend ratio of 1:1.5. The solution was then allowed

to stir overnight at room temperature. All the above processes were carried out in a glovebox under a nitrogen environment. The PTB7-Th:ITIC-2F precursor solution was formed by dissolving 10 mg of PTB7-Th in 1 mL chlorobenzene and 15 mg of ITIC-2F in 0.25 mL of chlorobenzene. The individual solutions were stirred for 4 hours and then mixed together along with 26  $\mu\text{L}$  of DIO to yield a 20  $\text{mgmL}^{-1}$  concentration with blend ratio of 1:1.5. The solution was then allowed to stir overnight at room temperature. The above processes were carried out in a glovebox under a nitrogen environment as well. The F8BT precursor solution was formed by dissolving 10 mg of F8BT in 1 mL of toluene. The solution was then allowed to stir overnight at room temperature in the nitrogen glovebox. The ZnO precursor solution was formed by dissolving 0.1 g zinc acetate dihydrate and 28  $\mu\text{L}$  ethanolamine in 1 mL of 2-methoxyethanol. The solution was then stirred vigorously for 12 hours at room temperature. The SnO<sub>2</sub> precursor solution was formed by dissolving 45.13 mg of tin chloride dihydrate in 2 mL ethanol and stirring overnight at room temperature. The MgO precursor solution was formed by dissolving 5 mg of magnesium acetate tetrahydrate in 1 mL of ethanol and stirring overnight at room temperature.

#### **4.2.2 Device fabrication**

The first step to form the ITO/ZnO/MgO/PTB7-Th:PC<sub>70</sub>BM/MoO<sub>3</sub>/Au OPV structure (shown in Figure 19 (a)) is the cleaning of glass/ITO substrates (Ossila ITO glass substrates – pixelated anode (S101)) in an ultra-sonicator sequentially, using soapy water, acetone and isopropanol for 10 minutes in each case. The substrates were then dried with a nitrogen spray gun. A ~ 30 nm (as measured by a profilometer) ZnO layer was then formed by spin-coating the ZnO precursor

solution on top of the substrate at 3000 revolutions per minute (rpm) for 30 seconds, followed by 1 hour annealing at 150°C in air. The ~ 10 nm MgO layer was then formed by spin-coating the MgO precursor solution on top of the ZnO layer at 5000 rpm for 30 seconds, followed by 1 hour annealing at 150°C in air. Devices with a thicker ~ 150 nm MgO layer were formed by spin-coating the MgO precursor solution at 3000 rpm for 30 seconds, followed by 1 hour annealing at 150°C in air. Samples were then transferred to a nitrogen glovebox for the deposition of the PTB7-Th:PC<sub>70</sub>BM active layer. This was deposited via spin-coating at 670 rpm for 60 seconds. The samples were then masked and loaded into a metal evaporator (also housed in the nitrogen glove-box) that was evacuated to a residual pressure of  $1.6 \times 10^{-6}$  mbar before evaporation. A 10 nm MoO<sub>3</sub> layer was then thermally evaporated with a rate of 0.1 Ångstrom second<sup>-1</sup> (Ås<sup>-1</sup>). This was followed by thermal evaporation of 80 nm of Au at rate of 0.2 Ås<sup>-1</sup>. These devices were completed by encapsulation with an epoxy resin (Ossila E132) applied on top of the whole cell, and glass cover slips (Ossila C181), and by application of electrical connection legs (Ossila E241). In the studies presented, a range of other structures have been employed to form OPVs. The same fabrication processes have been followed for these devices as well, with minor modifications. Specifically, if no MgO is found in the structure, the process is identical but skipping the MgO deposition and its 1 hour annealing step. Similarly, when no HTL is applied in the structure, the evaporation of MoO<sub>3</sub> is skipped. In the case where Ag is used as a top contact rather than Au, this is evaporated under  $1.6 \times 10^{-6}$  mbar pressure at 0.25 Ås<sup>-1</sup> to form a 100 nm contact. In the case where PTB7-Th:ITIC-2F instead of PTB7-Th:PC<sub>70</sub>BM was used as

the active material, this was spin-coated inside the glovebox at 1000 rpm for 90 seconds. Lastly, for devices employing the SnO<sub>2</sub> ETL, this was formed via a two-step spin-coating process first at the spin speed of 1500 rpm for 30 seconds, followed by a further 30 seconds at 2500 rpm, to form a ~ 24 nm thick layer. The layer was then annealed for 1 hour at 150°C in air. For the transmittance/absorbance, AFM and Kelvin probe investigations samples with varying structures were prepared. All layers in these samples were processed with the same conditions used for the corresponding layers in OPVs. Lastly, samples intended for the testing of the ITO and ITO/SnO<sub>2</sub> substrates via EA spectroscopy were fabricated in the same manner as OPVs, but instead of a blend, F8BT was employed as the active layer that was deposited via spin-coating at 1000 rpm for 90 seconds in the nitrogen glovebox. These samples were not encapsulated and their measurement was carried out under vacuum (~10<sup>-3</sup> mbar). Finally, for the ITO/PEDOT:PSS/PTB7-Th:PC<sub>70</sub>BM/Ca/Al structure used in the preliminary investigations, the PEDOT:PSS was filtered and deposited via spin coating at 5000 rpm and annealed at 150°C for 10 minutes in air and the Ca and Al were evaporated under 1.6x10<sup>-6</sup> mbar pressure to form a 30 nm contact at a rate of 0.4 Ås<sup>-1</sup> and a 200 nm contact at a rate of 2 Ås<sup>-1</sup> respectively.

### **4.3 Preliminary investigations**

For an effective comparison between the ZnO/MgO ETL and the ZnO-only ETL a reproducible testing system to be used as benchmark is necessitated. Therefore, the starting point of the study is the optimisation of the performance of

an OPV based on the ZnO-only ETL and the active materials used (PTB7-Th and PC<sub>70</sub>BM).

In the first iteration of experiments, whose aim was to optimise the active layer blend, the more “typical” direct ITO/PEDOT:PSS/PTB7-Th:PC<sub>70</sub>BM/Ca/Al architecture was employed. As shown by Song et al.<sup>119</sup> the donor:acceptor ratio in PTB7-Th:PC<sub>70</sub>BM active layer blends significantly alters the resulting PCE of OPV devices. A limited amount of PC<sub>70</sub>BM results to limited percolation pathways of the acceptor, whereas an excessive amount leads to a decreased polymer crystal size and crystallinity of the donor. The best performance is achieved at an optimal donor:acceptor phase separation when the donor:acceptor ratio is 1:1.5. To achieve roughly reproducible results between batches the donor:acceptor ratio for PTB7-Th and PC<sub>70</sub>BM was always set to 1:1.5. To observe whether the correct ratio was achieved when this blend was used, UV-VIS was employed. For an accurate ratio, the expected peak intensity for the polymer at 700 nm and fullerene signal at 400-600 nm has roughly the same intensity. It is useful to note that even with careful experimentation that enables a correct blend ratio (as evidenced by UV-VIS spectra) small deviations between the PCE of different batches of OPVs can still be present. Once reproducible results with the direct architecture were achieved, a move towards an inverted architecture and the first proof of principle tests of the benefits of MgO addition were attempted. Before using ZnO, ITO/SnO<sub>2</sub> with and without an MgO interlayer (deposited at 5000 rpm) were used as ETLs (similarly to previous investigations in the literature)<sup>79</sup>, with Au serving as the counter electrode. The current-density voltage curves for these

investigations are shown in Figure 17. The devices yielded “s-shaped” current density–voltage curves. Such an “s-shaped” curve for SnO<sub>2</sub>-only ETLs in OPV devices have been previously reported in the literature, e.g. by Tran et al.<sup>120</sup> “S-shaped” curves are observed when accumulated carriers within a device induce an electric field that opposes the motion of carriers drifting to the electrode under the V<sub>BI</sub>. The charge carrier accumulation resulting in “s-shape curves” could for example originate from defects or dipoles at the interface of contacts or unbalanced charge carrier mobilities.<sup>121</sup> Tran et al. mitigated the occurrence of “s-shaped” characteristics by incorporating a bilayer SnO<sub>2</sub>/CsCO<sub>3</sub> ETL in the device structure. Similarly, as shown in Figure 17, the MgO addition removes some of the “s-shape” behaviour, boosting the PCE from 1.44% to 2.08%.

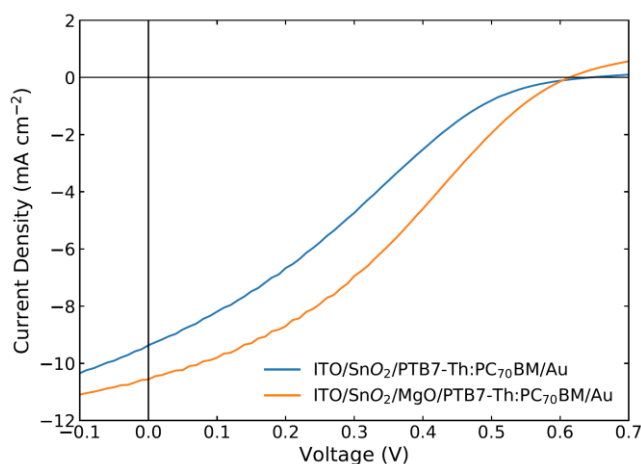


Figure 17. Current density–voltage curves under 1 Sun illumination for OPVs with SnO<sub>2</sub> vs. SnO<sub>2</sub>/MgO ETLs.

Since the objective of the study was to employ MgO to improve ZnO based OPVs, the SnO<sub>2</sub> OPVs were not optimised and in the next iteration of experiments, ZnO based ETLs were used instead as shown in Figure 18. The corresponding average key PV performance indicators for these devices are set out in Table 2.

These results were the first indication that addition of ultra-thin MgO results in an increase in PCE for ZnO based devices, through an increase in the  $J_{sc}$  and the FF. The increase in  $J_{sc}$  was also verified by the calculation of the photocurrent from EQE spectra calculated to be  $8.5 \pm 0.7$  and  $8.7 \pm 0.7$   $\text{mAcm}^{-2}$  for the single ZnO ETL and the ZnO/MgO(5000 rpm) ETL respectively, which are in agreement with the extracted data from the current density–voltage investigations.

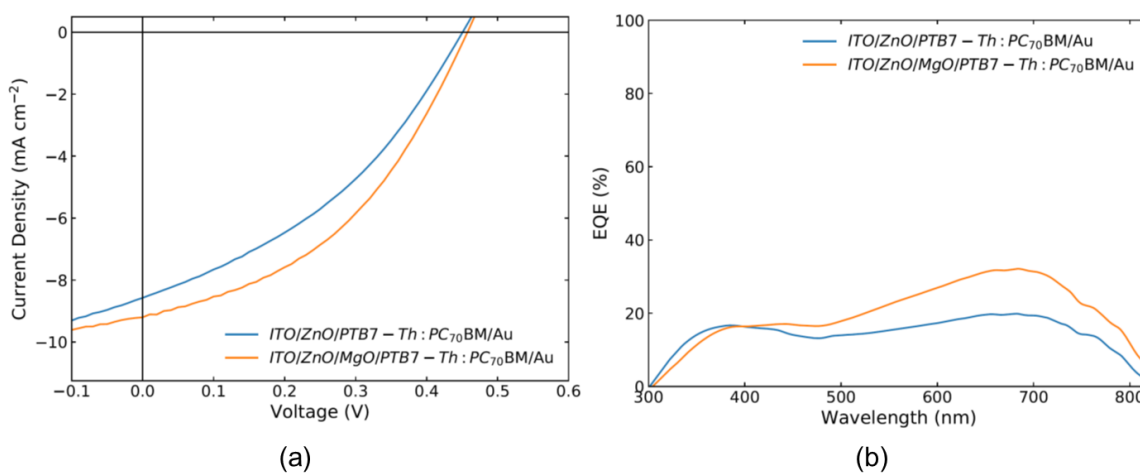


Figure 18. (a) Representative current density–voltage curves under 1 Sun illumination and (b) representative EQE curves of a single ZnO ETL vs. the bilayer ZnO/MgO ETL.

Table 2. Variation in key PV parameters of OPVs based on a single ZnO ETL vs. the bilayer ZnO/MgO ETL.

ETL	PCE (%)	$J_{sc}$ ( $\text{mAcm}^{-2}$ )	$V_{oc}$ (V)	FF
ZnO	$1.61 \pm 0.09$	$8.9 \pm 0.5$	$0.46 \pm 0.01$	$0.39 \pm 0.01$
ZnO/MgO(5000rpm)	$1.75 \pm 0.06$	$9.2 \pm 0.2$	$0.46 \pm 0.01$	$0.41 \pm 0.01$

The final modification applied to increase the performance of the OPV devices, is the application of an HTL ( $\text{MoO}_3$ ) which is essential to achieve good extraction. A schematic of the final multi-layered structure used in the investigations and the

approximate energy level structure of its components are shown in Figure 19. The addition of the HTL results in a PCE of 3.98% for the ZnO-only device that could now be used as a benchmark to test the effect of MgO addition.

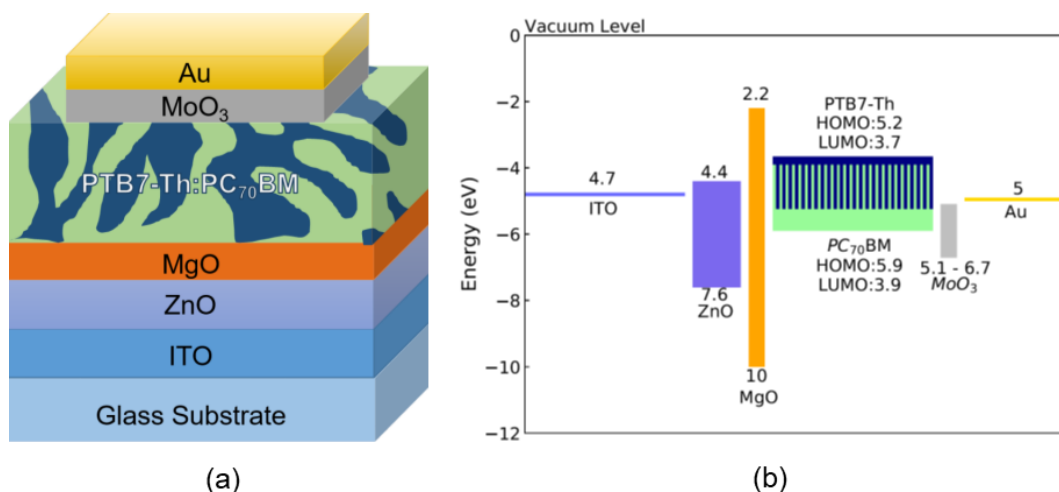


Figure 19. (a) Schematic of the multi-layered structure of the optimised OPV devices. (b) Approximate energy levels for the different components used in the OPV device (values have been obtained from the literature<sup>95, 104, 122-124</sup>). In the case of MoO<sub>3</sub> a relatively large range is reported (please note the rectangle is not meant to indicate the energy gap but the spread of reported values of work function) since it is known that the work function depends strongly on the preparation conditions. Values ~ 5.1 eV were measured in our own laboratory.

## 4.4 Results

After the completion of the preliminary experiments, the effect of MgO as a top component to form bilayer ETLs with ZnO was analysed. More specifically, the fabricated OPV devices are tested with a number of electrical tests and their corresponding ETL films have undergone further physical and optical characterisation. For these investigations the device structure used is ITO/ZnO/(MgO)/PTB7-Th:PC<sub>70</sub>BM/MoO<sub>3</sub>/Au unless otherwise stated. For brevity,

in the Figures, these structures are referred to as ETL:ZnO for the ZnO-only device and ETL:ZnO/MgO for the device containing the MgO interlayer. For a better insight to the effect of MgO, two different thickness regimes for MgO were tested where the MgO was deposited at 3000 rpm corresponding to a thickness of ~ 150 nm and 5000 rpm that results in a thickness of ~ 10 nm as measured by profilometry. For clarity, the deposition settings are stated in each case.

#### **4.4.1 Electrical characterisation of organic photovoltaic devices**

The current density–voltage characteristics at 1 Sun illumination for OPVs based on a single ZnO ETL vs. the bilayer ZnO/MgO ETL (where MgO was deposited at 5000 rpm or 3000 rpm) are shown in Figure 20 (a). The corresponding average key PV performance indicators are set out in Table 3.

The application of the ZnO/MgO bilayer rather than the single ZnO layer (when MgO is kept sufficiently thin ~ 10 nm (5000 rpm)) successfully enhances the performance, boosting the PCE by ~ 10%. This is achieved mainly through an increase in  $J_{sc}$  and in the FF. The increase in  $J_{sc}$  has also been verified by the calculation of the photocurrent from EQE spectra (Figure 20 (b)) calculated to be  $10.5 \pm 0.7$  and  $11.0 \pm 0.7$   $\text{mAcm}^{-2}$  for the single ZnO ETL and the ZnO/MgO(5000 rpm) ETL respectively, which are in agreement with the extracted data from the current density–voltage investigations. It is important to note that the efficient operation of OPVs employing the MgO interlayer requires the layer to be kept ultrathin (~ 10 nm). For the case of the thicker MgO devices (spin-coated at 3000 rpm with resulting thickness of ~ 150 nm) a poor performance is obtained with a PCE of  $0.03 \pm 0.02\%$  which is the result of a very low  $J_{sc}$  and FF. The current

density–voltage curves for the OPV devices in the dark are shown in Figure 20 (c). Addition of MgO reduces the leakage current which is indicative of an increased effective  $R_{SH}$  for the bilayer devices.<sup>125, 126</sup> The average current density of the single ZnO ETL devices in dark conditions at -1 V is  $-2.9 \times 10^{-3} \text{ mAcm}^{-2}$  and the  $R_{SH}$  is  $5.82 \times 10^5 \text{ } \Omega\text{cm}^2$ . In the case of the ZnO/MgO(5000 rpm) ETL devices, the presence of the MgO layer leads to halving of the leakage current at -1 V (down to  $-1.7 \times 10^{-3} \text{ mAcm}^{-2}$ ) and to an increase of the  $R_{SH}$  to almost double the value of the device without MgO, i.e. up to  $8.35 \times 10^5 \text{ } \Omega\text{cm}^2$ . The increased  $R_{SH}$  can prevent power losses that occur via alternative current paths.<sup>127</sup> To evidence the enhanced extraction properties under illumination due to the addition of ultrathin MgO I plot the  $J_{PH}$  vs.  $V_{EFF}$  curves as shown in Figure 20 (d). I find that the  $P_{DISS}$  (which is an indicator of the effectiveness with which dissociated excitons are extracted) increases from 95.90% for the single ZnO ETL device to 96.42% for the ZnO/MgO(5000 rpm) ETL device. In addition, I investigated the rise and decay times of the  $V_{OC}$  for these devices as shown in Figure 20 (e, f). The OPV device based on the ZnO/MgO(5000 rpm) ETL takes a longer time to be completely discharged in comparison to the single ZnO ETL device and requires a shorter rise time to arrive at the maximum  $V_{OC}$  which serve as evidence of reduction in recombination losses. From the increased  $J_{PH}$ , I infer that the addition of the ultrathin MgO results in a reduction in the  $R_s$  as well. The simultaneous increase in  $R_{SH}$  and decrease in  $R_s$  is conducive to the observed increase in the  $J_{SC}$  and FF for the devices that employ the ultrathin MgO measured under illumination and lead to the boost in PCE. For the case of the devices where a thicker MgO layer is employed (spin-coated at 3000 rpm,

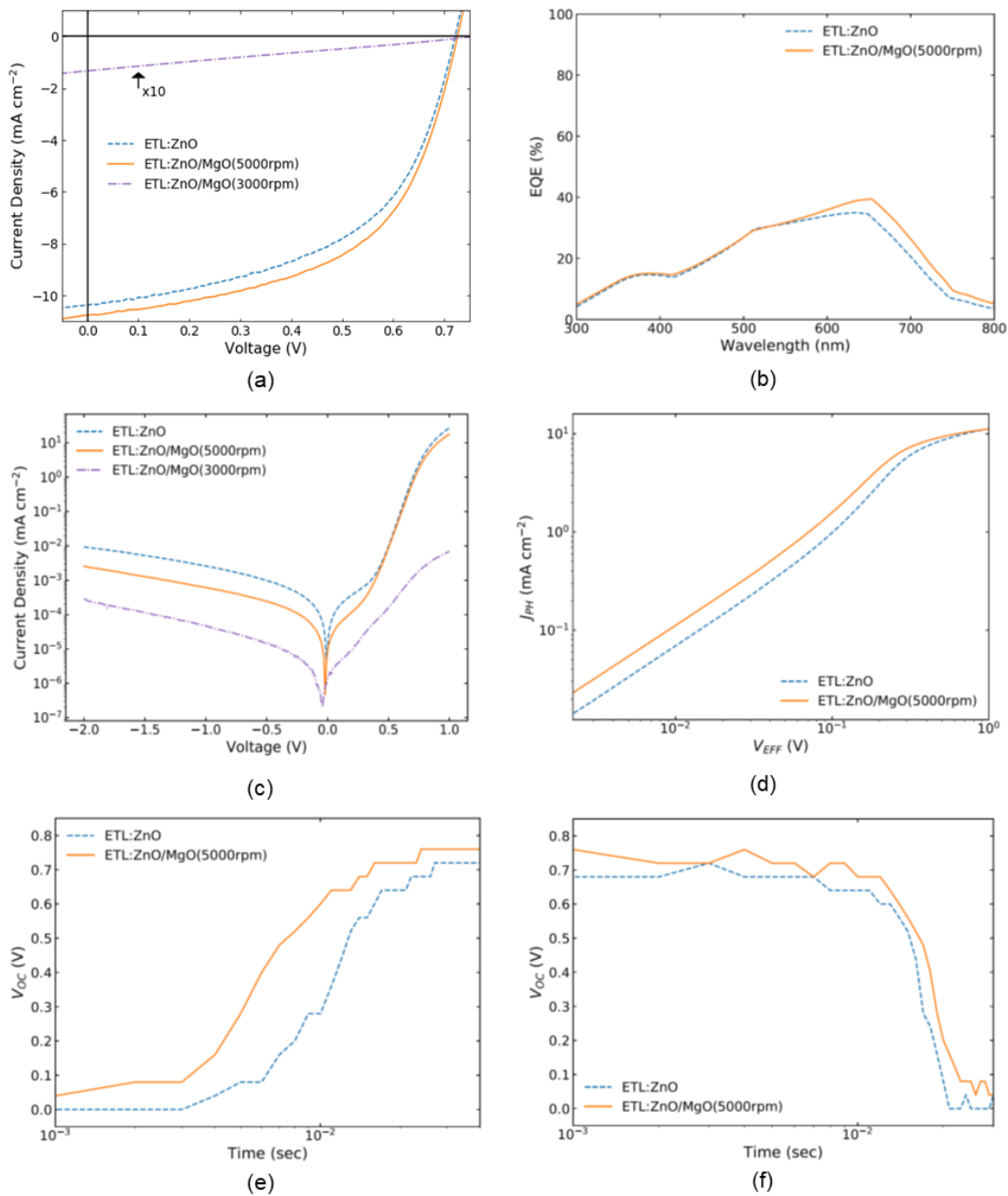


Figure 20. (a) Representative current density–voltage curves under 1 Sun illumination. Active layer: PTB7-Th:PC<sub>70</sub>BM. Here the current density for the device with the thicker MgO layer (3000 rpm, ~ 150 nm) has been multiplied by a factor of 10 to aid legibility. (b) Representative EQE curves (c) Representative current density–voltage curves in the dark. (d) Representative  $J_{PH}$  -  $V_{EFF}$  curves. (e) Representative  $V_{OC}$  rise curves (after switch on (1 Sun illumination)). (f) Representative  $V_{OC}$  decay curves (after switch off (1 Sun illumination)). The thickness of the MgO layer is ~ 10 nm when the precursor is spin-coated at 5000 rpm.

Table 3. Variation in key PV parameters of OPVs based on a single ZnO ETL vs. the bilayer ZnO/MgO ETL. Averages from 7 distinct devices with multiple measurements are reported for each device type

ETL	PCE (%)	J <sub>sc</sub> (mAcm <sup>-2</sup> )	V <sub>oc</sub> (V)	FF
ZnO	3.98 ± 0.16	10.6 ± 0.5	0.72 ± 0.01	0.53 ± 0.03
ZnO/MgO(5000 rpm)	4.31 ± 0.14	10.9 ± 0.2	0.72 ± 0.01	0.55 ± 0.02
ZnO/MgO(3000 rpm)	0.03 ± 0.02	0.2 ± 0.1	0.73 ± 0.01	0.26 ± 0.02

corresponding to ~ 150 nm thickness), even though an even lower leakage current at -1 V of  $-8.2 \times 10^{-5}$  mAcm<sup>-2</sup> and a higher R<sub>SH</sub> of  $1.66 \times 10^6$  Ωcm<sup>2</sup> are achieved, the much thicker insulating layer results in a significant increase in the R<sub>s</sub> leading to a decreased J<sub>sc</sub> and to the FF approaching a value of 0.25 that leads to a hindering of the PCE.

#### 4.4.2 Characterisation of electrodes

##### AFM and cAFM

AFM measurements were carried out to investigate variations in the surface morphology and Sq of ITO/ZnO electrodes vs. ITO/ZnO/MgO electrodes with MgO thicknesses of ~ 10 nm and ~ 150 nm. The 1.6 μm x 1.6 μm images of the above investigations are presented in Figure 21 (a, b, c)). To allow for comparison, I generated images using the same scale height (35 nm). The samples with an MgO uppermost layer appear darker (peaks have a shorter height) and have a lower Sq with increasing MgO thickness evidencing that the MgO layer that is deposited on top of ZnO lacks uniformity. CAFM measurements were carried out

on the corresponding electrodes as well and are shown in Figure 21 (d, e, f). The charge extracted from the electrodes with an MgO uppermost layer is a function of the thickness of MgO (due to its insulating nature) and for the case of the thicker MgO ( $\sim 150$  nm) the current is  $\sim 0$  nA (Figure 21 (f)). This finding is in line with the electrical characterisation of the OPV devices. The blocking of the charges due to the thick MgO leads to an increased  $R_s$  in the corresponding OPV device and hence the very low PCE of  $0.03 \pm 0.02$  %.

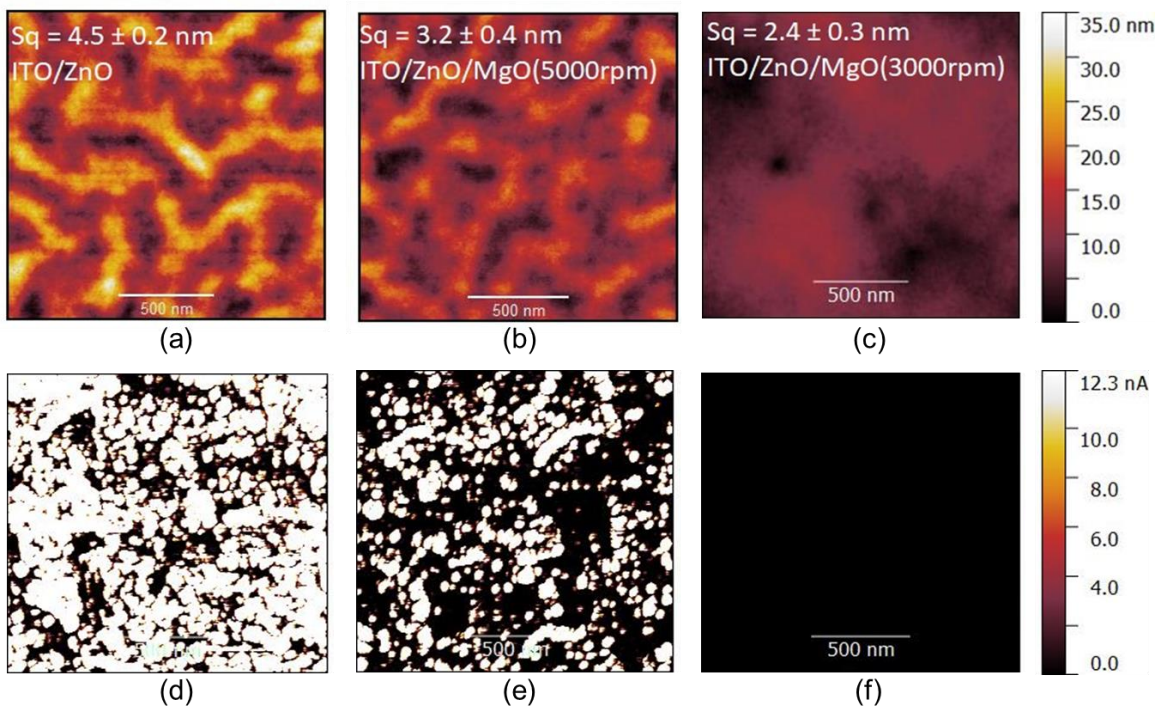


Figure 21. Tapping mode AFM images of the topography of (a) ITO/ZnO, (b) ITO/ZnO/MgO(5000 rpm) and (c) ITO/ZnO/MgO(3000 rpm). CAFM images of (d) ITO/ZnO, (e) ITO/ZnO/MgO(5000 rpm) and (f) ITO/ZnO/MgO(3000 rpm)

For the case of the ultrathin MgO interlayer, due to the lack of uniformity of MgO, it is likely that its thickness is significantly less than 10 nm (therefore enabling efficient charge transport) in certain areas. In other areas it maintains a higher thickness (and insulating nature) as shown in Figure 21 (e). The question

therefore arises as to whether a relatively limited extent of the electrode's area that is effective for charge extraction can still be sufficient for preserving a high overall device performance. Interestingly, and as shown by Dabera et al.,<sup>128</sup> it is possible for ~ 99% of the surface of an ETL to be electrically insulating without eroding the efficiency of charge carrier extraction given that sufficient pathways for conduction remain. The ultrathin and non-uniform MgO interlayer (obtained at spin-coating speeds of 5000 rpm) appears to provide a general suppression of the leakage current and so a higher  $R_{SH}$  as a result of the insulating MgO, while simultaneously preserving sufficient "charge transparency", presumably through the thinner MgO regions and hence leads to the boost in PCE in the corresponding OPV devices. The decrease in  $S_q$  from  $4.5 \pm 0.2$  nm for the ITO/ZnO electrode to  $3.2 \pm 0.4$  nm for the ITO/ZnO/MgO(5000 rpm) sample might also be beneficial and partly contribute to the increase in device performance. Contradictory reports can be found in the literature regarding how the surface roughness of the ETL affects the PCE of OPVs. Some reports show enhanced PV performance upon an increase in  $S_q$ <sup>108, 129</sup> while others support that an increase in performance is a result of a lower surface roughness.<sup>95, 96, 112, 114, 120</sup> Both cases are equally valid but need a further distinction. If the increased roughness is a result of forming specific nanopatterns that aim to change the morphology of the PV blend, then this may be accompanied by an increase in performance. In the case where a change in morphology is not targeted (vide infra), the lower roughness is indicative of a top surface of the ETL with fewer pinholes. This is beneficial as it decreases the number of defective interfaces

where recombination can happen and can lead to a reduction in pathways for current leakage that can lead to an increase of the  $J_{sc}$  and FF.

### Kelvin probe and EA spectroscopy

I have investigated whether the application of MgO on top of metal oxides alters the work function by use of a Kelvin probe as shown in Figure 22.

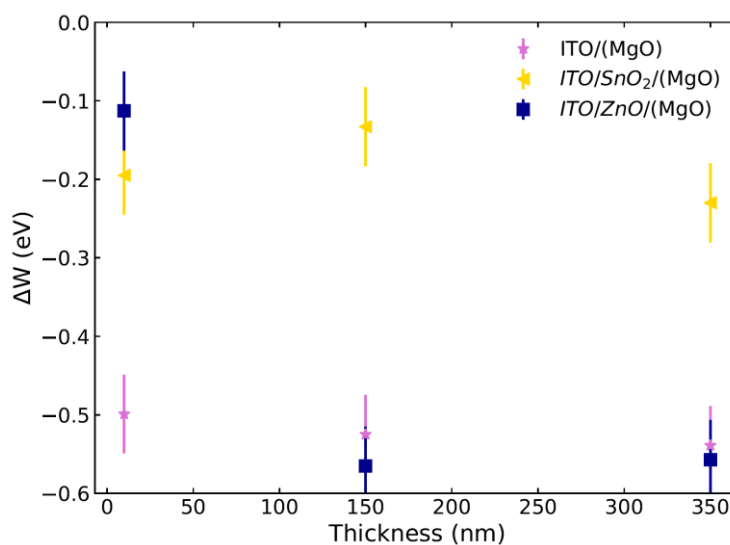


Figure 22. Kelvin probe measurements showing the change in the work function of different substrates upon addition of the MgO layer with varying thickness.

To gain an insight on the potential mechanism by which MgO alters the work function of metal oxides, MgO was deposited on three different electrodes namely ITO, ITO/SnO<sub>2</sub> and ITO/ZnO at three different spin-coating speeds, 5000, 3000 and 1000 rpm corresponding to approximate thicknesses of 10, 150 and 350 nm as measured by profilometry. The work function of the electrodes is reduced by the addition of MgO in all cases. The change in work function ( $\Delta W$ ) differs for each electrode and seems to be independent of the thickness of MgO for ITO and ITO/SnO<sub>2</sub>, whilst for ITO/ZnO, it seems to be thickness dependent only at very small thicknesses (which may be a result of partial coverage). This overall

thickness independence points towards an interfacial mechanism being responsible for the decrease in work function. The application of MgO on different metals and semiconductors and its effect on the corresponding work function has been extensively studied in the literature as a promising solution for catalysis.<sup>130</sup>

The three main mechanisms that have been identified to dictate work function modifications in general are respectively:

- (1) The electrostatic compressive effect
- (2) Charge transfer
- (3) Surface relaxation

For the case of MgO, the electrostatic compressive effect can give a significant contribution.<sup>131</sup> This interfacial effect enables the MgO layer to form a surface dipole on the metal or semiconductor surface even in the absence of charge transfer. The different levels of the contribution of these mechanisms can give considerable differences in the final change in work function, hence the change in work function can be rather different for different substrate materials. This explains why such different values of work function shift ( $\Delta W$ ) are observed upon MgO application for the different substrates studied in my investigations.

A modification in the work function of the ETL can be crucial to OPV operation, since it can enable better matching of the work function of the ETL with the LUMO of the acceptor material.<sup>50</sup> The LUMO level of PC<sub>70</sub>BM is reported to be - 3.9 eV<sup>132</sup> whereas the ITO/ZnO work function was measured by Kelvin probe to be 4.76 eV. By applying the ultrathin MgO layer (spin-coated at 5000 rpm) and

by reducing the work function by 0.1 eV to 4.66 eV, the relevant energy level mismatch is reduced and therefore the losses connected with charge extraction. A change in the work function of an electrode may be manifested as a change in the built-in voltage of the completed device. To measure changes in the built-in voltage upon application of the ultrathin MgO (spin-coated at 5000 rpm) EA spectroscopy was employed as shown in Figure 23. The built-in voltage can be extracted from these plots at the point where the DC voltage nulls the EA signal.<sup>133</sup> As I am interested in probing the change caused by the addition of MgO in the device structure, I characterise devices free of an HTL that provide a clearer demonstration of changes only occurring at the ETL/blend interface. For completeness, I investigate the modification resulting from the presence of MgO on both ITO and ITO/SnO<sub>2</sub> based devices, in addition to the ITO/ZnO device. For ITO and ITO/SnO<sub>2</sub> based devices F8BT was used as the active material as these electrodes were not optimised for OPV application. For the ITO/ZnO device the active layer blend employed in the OPV devices is used (PTB7-Th:PC<sub>70</sub>BM). The measured changes in built-in voltage ( $\Delta V_{BI}$ ) for the devices are found in Table 4 along with the shift in work function (from Kelvin Probe).

The  $V_{BI}$  is increased in all cases and the shift in the built-in voltage is consistent with the shift in work function. Often, a change in the built-in voltage results in a change in the  $V_{OC}$  of OPV devices as well. I do not exclude this possibility, however, scatter from device to device may have washed out the slight difference in  $V_{OC}$  in the average for the investigations presented in section 4.4.1. For devices with thicker MgO layers a bigger shift in  $V_{OC}$  of 0.1 V is obtained. This is likely the

result of a more complete coverage of the MgO layer. An increase in  $V_{BI}$  (and thus a higher internal field) can lead to reduced recombination losses and elimination of the build-up of space charge. Hence both the slightly lower electrode work function and higher built-in voltage are likely enabling (partly) the higher  $J_{SC}$  and FF achieved.<sup>134</sup> However, as the changes in work function and built in voltage are small, I expect that the higher  $R_{SH}$  due to the MgO presence has a more significant contribution in the attainment of the higher PCE.

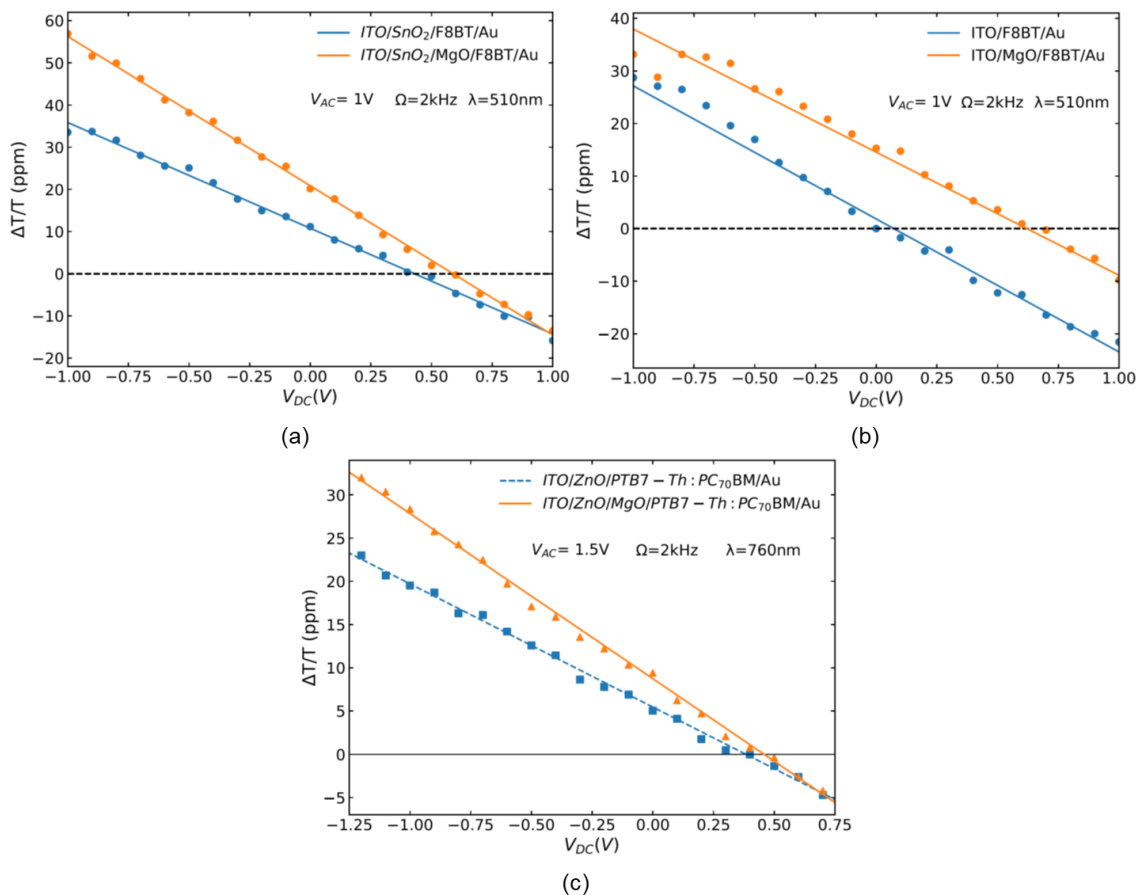


Figure 23. EA signal vs. DC voltage plots used to extract the built-in voltage in the single ETL and bilayer ETL devices for (a)  $ITO/SnO_2$ , (b)  $ITO$  and (c)  $ITO/ZnO$ . F8BT was used as the active material for (a) and (b) whereas PTB7-Th:PC<sub>70</sub>BM was used for (c). The parameters used for the experiments are displayed in the Figure. The MgO layer thickness is  $\sim 10$  nm.

Table 4. The difference in built-in voltage and in work function between samples with and without MgO (5000 rpm) for the three tested substrates. For reference, the work functions of ITO/ZnO, ITO/SnO<sub>2</sub> and ITO were measured by Kelvin probe to be  $4.76 \pm 0.03$  eV,  $4.95 \pm 0.03$  eV and  $4.89 \pm 0.03$  eV respectively.

Sample	Active Layer	$\Delta V_{BI}$ (V)	$\Delta W$ (eV)
ITO/(MgO)	F8BT	$0.46 \pm 0.03$	$-0.50 \pm 0.05$
ITO/SnO <sub>2</sub> /(MgO)	F8BT	$0.19 \pm 0.03$	$-0.20 \pm 0.05$
ITO/ZnO/(MgO)	PTB7-Th:PC <sub>70</sub> BM	$0.05 \pm 0.03$	$-0.11 \pm 0.05$

### Transmittance and blend morphology

As discussed in section 2.2.3 two other potential mechanisms that could lead to increased performance via the modification of an ETL in addition to the change in its interfacial properties that has been observed are an increase in transmittance of the semi-transparent electrode or a favourable change in active layer blend morphology. To assess whether the ultrathin MgO interlayer leads to an improved rate of photon capture or favourable change in blend morphology I performed transmittance measurements on thin films of ITO, ITO/ZnO and ITO/ZnO/MgO(5000 rpm) and absorbance and AFM measurements on ITO/ZnO/PTB7-Th:PC<sub>70</sub>BM and ITO/ZnO/MgO(5000 rpm)/PTB7-Th:PC<sub>70</sub>BM films as displayed in Figure 24. The addition of MgO on top of ZnO seems to have a negligible effect in altering the transmittance. Moreover, the absorbance spectra of films also incorporating the PTB7-Th:PC<sub>70</sub>BM blend are almost identical for ITO/ZnO and ITO/ZnO/MgO(5000 rpm) substrates. It is therefore improbable that an improved rate of photon capture is achieved via the addition of MgO. It is useful to note that the absorbance between 400-600nm (PC<sub>70</sub>BM

characteristic) and at 700nm (PTB7-Th characteristic) is similar, as expected for a blend with a 1:1.5 donor:acceptor ratio. The surface morphology of the samples with the blend (Figure 24 (c, d)) is almost indistinguishable with an identical  $S_q$  of  $1.0 \pm 0.1$  nm. Therefore, regarding the mechanism by which MgO facilitates performance enhancement, it is unlikely that it is associated with a favourable change in the blend morphology since any changes in the bulk of the blend would have also very likely been manifested in the uppermost surface characterised by the AFM investigation.

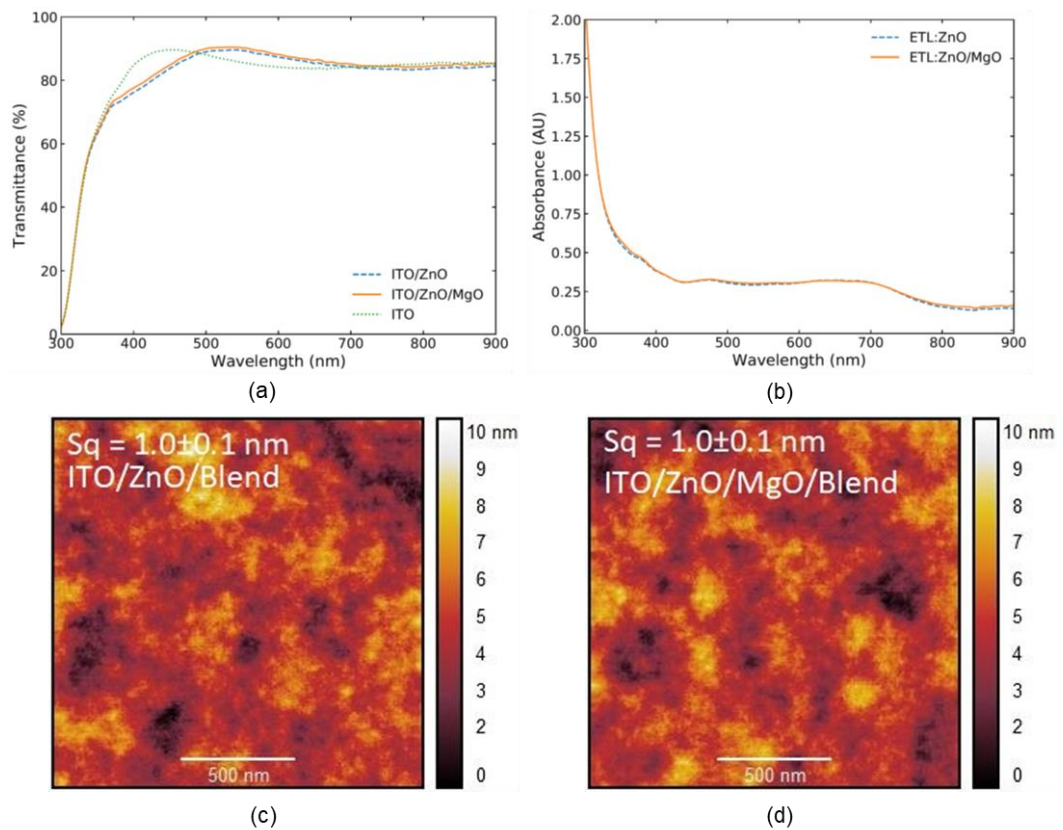


Figure 24. (a) Transmittance of ITO, ITO/ZnO, ITO/ZnO/MgO(5000 rpm) films. (b) Absorbance spectra of thin films comparing the ITO/ZnO/PTB7-Th:PC<sub>70</sub>BM with the ITO/ZnO/MgO(5000 rpm)/PTB7-Th:PC<sub>70</sub>BM structures. Tapping mode AFM images (1.6  $\mu$ m x 1.6  $\mu$ m) of the topography of (c) ITO/ZnO/PTB7-Th:PC<sub>70</sub>BM, (d) ITO/ZnO/MgO(5000 rpm)/PTB7-Th:PC<sub>70</sub>BM. The addition of MgO seems to have a negligible effect in these investigations.

### 4.4.3 Extending the use of ultrathin MgO to other types of organic photovoltaic diodes

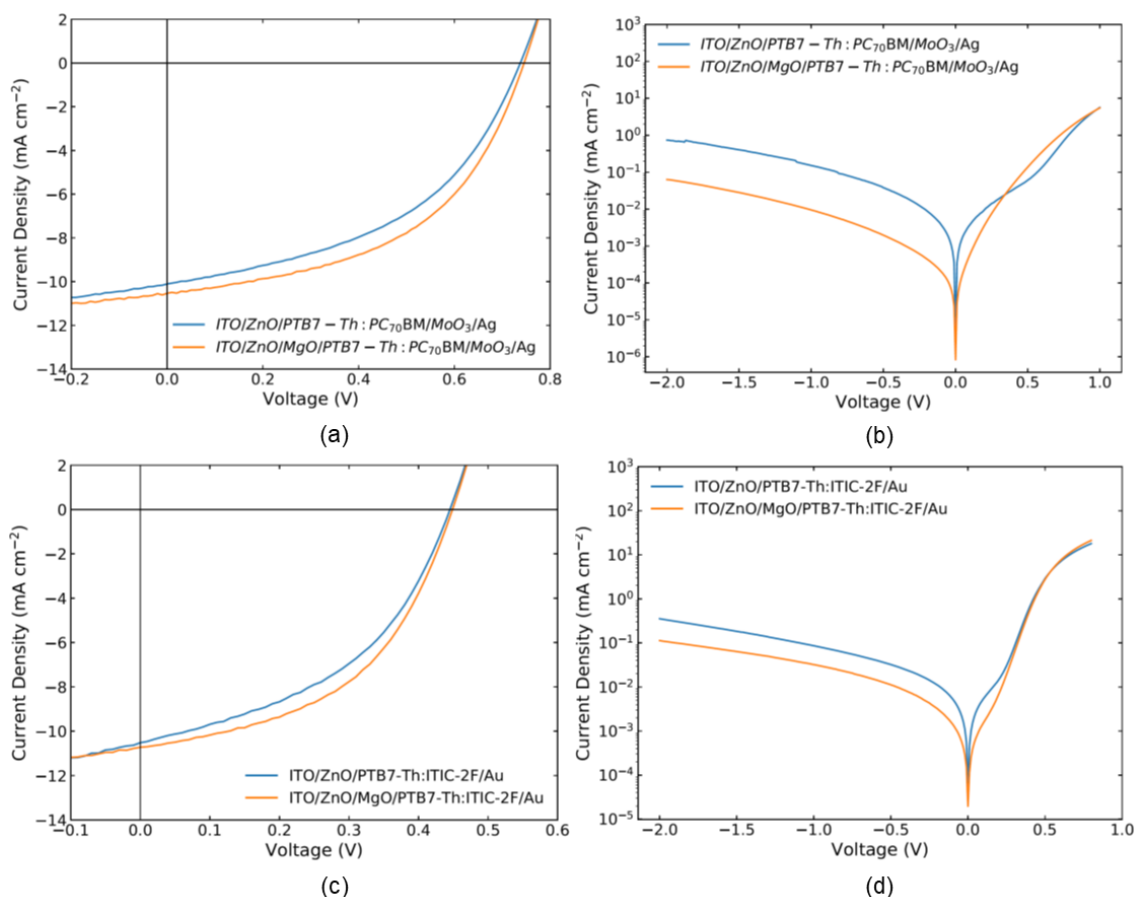


Figure 25. Representative current-voltage curves demonstrating the success of the bilayer MgO ETL vs. a single ETL for various OPV architectures. Measurements for Au top contact substituted with Ag under 1 Sun illumination (a) and in the dark (b). Devices with a blend containing the NFA ITIC-2F rather than PC<sub>70</sub>BM as the acceptor under 1 Sun illumination (c) and in the dark (d).

To demonstrate that the application of an MgO bilayer ETL can be extended to more types of OPVs, I have applied this strategy to other systems as well and assessed its effectiveness. The representative current density–voltage characteristic curves and the corresponding average key PV performance indicators for the modifications can be found in Figure 25 (a,c) and Table 5. For these studies the MgO precursor was spin-coated at 5000 rpm. Firstly, the Au top

contact was substituted with Ag (that can serve as a cheaper alternative). Devices with a blend containing the NFA ITIC-2F rather than PC<sub>70</sub>BM as the acceptor have also been tested.

*Table 5. Variation in key PV parameters of OPVs based on a single ZnO ETL vs. the bilayer ZnO/MgO ETL when the Au top contact is substituted with Ag and a blend containing the NFA acceptor ITIC-2F rather than PC<sub>70</sub>BM is used. Averages from 7 distinct devices with multiple measurements are reported for each device type.*

Sample	PCE (%)	J <sub>sc</sub> (mAcm <sup>-2</sup> )	V <sub>oc</sub> (V)	FF
ITO/ZnO/PTB7- Th:PC <sub>70</sub> BM/MoO <sub>3</sub> /Ag	3.44 ± 0.18	10.1 ± 0.4	0.72 ± 0.01	0.45 ± 0.02
ITO/ZnO/MgO/PTB7- Th:PC <sub>70</sub> BM/MoO <sub>3</sub> /Ag	3.61 ± 0.34	10.6 ± 0.4	0.72 ± 0.01	0.47 ± 0.02
ITO/ZnO/PTB7- Th:ITIC-2F/Ag	2.03 ± 0.24	10.5 ± 0.7	0.44 ± 0.01	0.44 ± 0.02
ITO/ZnO/MgO/PTB7- Th:ITIC-2F/Ag	2.31 ± 0.17	10.7 ± 0.7	0.44 ± 0.01	0.49 ± 0.02

The substitution of the single ZnO ETL to the ZnO/MgO ETL for these devices led to a PCE boost, through an increase in the J<sub>sc</sub> and FF further demonstrating the wider applicability of MgO based bilayer ETLs in OPVs. Note that the NFA device efficiencies are limited since a HTL is absent for these devices, clearly demonstrating the notion that in addition to a good ETL, the inclusion of a HTL is also crucial to achieve high PCE in OPVs. Current density–voltage characteristics in the dark for these devices were collected (Figure 25 (b,d)) and analysed to

extract the leakage current at -1 V and the  $R_{SH}$ . For devices based on the Ag top contact the leakage current at -1 V decreased from  $-2.8 \times 10^{-2}$  to  $-1.1 \times 10^{-2}$   $\text{mAcm}^{-2}$  with a corresponding increase in  $R_{SH}$  from  $2.49 \times 10^5$  to  $8.21 \times 10^5 \Omega\text{cm}^2$ . For devices consisting of ITIC-2F rather than PC<sub>70</sub>BM as the acceptor, similarly, a decreased current leakage is observed for devices based on the bilayer ETL from -1.1 to  $-1.3 \times 10^{-1}$   $\text{mAcm}^{-2}$ . This is accompanied by an increase in  $R_{SH}$  from  $5.3 \times 10^3$  to  $2.6 \times 10^4 \Omega\text{cm}^2$ . The above findings, support the “universality” of using the ZnO/MgO ETL instead of ZnO-only to boost the performance of OPVs.

## 4.5 Conclusions

In this chapter, MgO was investigated as a modifying interlayer on top of a ZnO ETL formed by simple solution-processing and low temperature annealing (150°C) for application in OPVs. The use of the ZnO/MgO bilayer rather than single ZnO as ETL, when MgO was kept ultrathin (~10 nm), led to a ~ 10% and ~ 15% increase in PCE in relative terms for devices consisting of a blend with a fullerene acceptor and a NFA respectively. The increase in PCE was a result of an enhanced  $J_{sc}$  and FF, which can mainly be attributed to a reduction in the leakage current and an increase in the  $R_{SH}$  and decrease in the  $R_s$  of devices. Thicker (~ 150 nm) MgO modifying interlayers are not suitable and lead to poor performance. Partial coverage of the ZnO by MgO, seems to be necessary to preserve sufficient “charge transparency” in the bilayer ETL for effective electron extraction. The presence of MgO leads to a number of favourable characteristics. Without significantly affecting the photon capture rate and blend morphology, the MgO interlayer offers an improved contact preventing shunts and blocking holes (due to its insulating nature and high ionisation potential) and by reducing the

surface roughness of the ETL and lowering its work function. This leads to a better energy level matching with the LUMO of the PV blend acceptor that results in enhanced charge extraction. The lower work function is shown to originate from an interfacial interaction between the MgO and the metal oxide that is consistent with the so-called electrostatic compressive effect.

# 5 Mg-doped ZnO electron transport layers

## 5.1 Introduction

Out of the three main strategies to optimise ZnO ETLs (as described in section 2.2.3), the most favourable strategy when considering fabrication of solution-processed PVs at an industrial scale, involves the direct addition of dopants in the precursor solution of the ZnO ETL so that the finalised improved ETL can be formed without the need of additional processing steps.

A number of different materials have been tested as dopants to be added to ZnO precursor solutions, and enabled formation of ETLs with superior characteristics when compared to their un-doped ZnO ETL counterparts (specifically in terms of PCE of OPVs incorporating them). The list of such dopants is varied and includes, among others, organic molecules, 2-D materials, and metals. For example, Li and collaborators<sup>122</sup> used the organic molecule 2,3,5,6-tetrafluoro-7,7,8,8-tetracyanoquinodimethane (F4TCNQ) as dopant, and found that it suppresses the non-geminate recombination in OPVs by passivating traps in ZnO and leads to a relative increase in the PCE by ~ 15%. Passivation of traps has also been achieved by an alternative molecular dopant TPT-S as shown by Xia et al.<sup>135</sup> Another successful organic molecule dopant for ZnO ETLs is an alcohol-soluble isoindigo derivative with thiophene groups and sulfobetaine zwitterions (IIDTh-NSB)<sup>102</sup> that can improve the interfacial compatibility between ZnO and the active

layer. The 2-D MXene  $\text{Ti}_3\text{C}_2\text{T}_x$  has also been recently used effectively as dopant in ZnO ETLs.<sup>103</sup> The  $\text{Ti}_3\text{C}_2\text{T}_x$  nanosheets act as bridges between the ZnO nanocrystals and therefore provide additional charge transfer paths. These favourable changes lead to a relative increase in the PCE by ~ 10%. Metals have also proved useful dopants for ZnO ETLs. Park, Kang & Cho<sup>136</sup> added aluminium to ZnO to optimise the ETL conductivity, thereby also reducing the overall cell  $R_s$ . Au nanoparticles have instead been used by Usmani et al.<sup>137</sup> and Chi et al.<sup>138</sup> to facilitate an increase in the optical absorption of the active layer via exploitation of plasmonic effects. Another transition metal, zirconium, has been employed by Song et al.<sup>139</sup> to improve electron transport and transmittance of ZnO and concomitantly increase the relative PCE by ~ 12%. Another recent example is the study by Wang et al.<sup>127</sup> where alkali metal salts (lithium acetate or caesium acetate) were used to dope the ZnO ETL. The study indicated an improved crystallinity of the ETL and an increased  $R_{SH}$ , leading to a reduced current leakage. The  $V_{oc}$ , FF and  $J_{sc}$  increased simultaneously for the devices with ETLs containing alkali metal salts.

Having used MgO successfully to form a bilayer ETL with ZnO (as demonstrated in chapter 4) we were interested to test whether direct addition of the MgO precursor to the ZnO precursor solution is a viable route to form an Mg-doped ZnO ETL for application to OPVs. Such an approach would obviously favour scalability at an industrial level because it requires fewer steps and eliminates the need to control the MgO layer thickness to a few nm. Thickness control is in fact crucial, because we observed that MgO interlayers of ~ 150 nm or so hinder

performance significantly and that for an efficient device, non-uniform ETLs are necessary. It would be rather difficult to achieve such a layer with the required degree of accuracy and consistency in an industrial process. Hence, directly doping the ZnO layer with Mg would be advantageous over the bilayer approach as it is much easier to control the concentrations of precursor materials rather than film thickness in large scale processes.

Previous literature demonstrated how an Mg-doped ZnO ETL formed from a single solution can be employed in a variety of solution-processed devices to improve efficiency. For example, such a layer has been incorporated in quantum dot and perovskite light-emitting diodes, either on its own or in combination with another ZnO layer to inject electrons.<sup>123, 124, 140-146</sup> Such studies have demonstrated that doping ZnO with Mg can lead to a more balanced injection and therefore an increase in the maximum external quantum efficiency and current efficiency. The improvement has been attributed to a decreased conductivity and an upward shift of the conduction band of the Mg-doped ZnO ETL compared to the un-doped ZnO ETL. These findings are in-line with studies investigating the optical properties of Mg-doped ZnO films and nano-particles which revealed that increasing the amount of Mg dopant results in an increase in the band gap of the ZnO thin film and that the work function of the Mg-doped ZnO film can be controlled based on the doping level of Mg.<sup>147-149</sup> Sol-gel Mg-doped ZnO ETLs have also been used to improve the PCE of several PV systems. These include silicon<sup>150</sup> and dye-sensitised solar cells<sup>151, 152</sup> as well as PVs based on Cu<sub>2</sub>O,<sup>153</sup> quantum dots<sup>154</sup> and perovskites.<sup>155, 156</sup> Since the working principle of these PV

systems differs, the mechanism by which each PV system benefits from the presence of Mg dopants varies. For example, the dye-sensitised solar cells benefit from the upward shifting of the conduction band which leads to an increased  $V_{OC}$  in the devices, that when balanced with  $J_{SC}$  yields the optimised performance. For the case of perovskite absorbers, the carrier recombination at the interface between the ETL and perovskite active layer is suppressed due to the Mg doping leading to the enhanced performance. Depending on the materials used and preparation protocols the amount of Mg doping necessary to form the “optimum” Mg-doped ZnO ETL varies.

The Mg-doped ZnO single layer ETL has provided excellent results in all the above systems, however, its use for OPVs has remained limited.<sup>157</sup> Only two works by Yin et al.<sup>158</sup> and by MacLeod et al.<sup>159</sup> have reported its application in BHJ OPVs. In both cases the Mg-doped ZnO ETL outperformed the corresponding un-doped ZnO ETL in terms of PCE as a result of the reduced carrier recombination and increased charge-collection. In the case of MacLeod et al. blends of poly(3-hexylthiophene-2,5-diyl) (P3HT) as the donor and PC<sub>70</sub>BM or indene-C60 bisadduct (ICBA) as acceptors were used as active layers. The best PCE was achieved when a doping of 10 mol% (of Mg in precursor solids) was present in the ETL with the increase in PCE mainly resulting from an enhanced  $V_{OC}$  and FF. In the study by Yin et al. the blend used as active layer consisted of poly [[4,8-bis[(2-ethylhexyl)oxy] benzo[1,2-b:4,5-b']dithiophene-2,6-diyl][3-fluoro-2-[(2-ethylhexyl)carbonyl]thieno [3,4-b] thiophenediyl]] (PTB7) as the donor and PC<sub>70</sub>BM as the acceptor. In this case the best PCE was achieved

with a doping of 30% Mg substitutional doping, (i.e. with  $x = 0.3$  in the zinc magnesium oxide layer with formula  $Zn_{1-x}Mg_xO$ ), with the biggest improvement observed in the  $J_{sc}$  and FF of the devices. Both of these studies are excellent demonstrations of the potential of Mg as a dopant to improve ZnO ETLs for use in OPVs. However, the annealing temperatures used to form the Mg-doped ZnO ETLs are 290°C and 300°C for Yin et al. and MacLeod et al. respectively. As discussed in section 2.2.3 reducing the annealing temperature at which the ETL is treated has various advantages in its applicability. For this reason, I investigated whether a lower annealing temperature of 150°C could also be applied to form Mg-doped ZnO ETLs for application in BHJ OPVs. The lower processing temperature might also allow, in principle, fabrication of the electrodes on top of an already deposited active layer without the damaging effects connected, for example, with sputtering (e.g. of ITO).<sup>160</sup> In addition, I have tested that the benefits of this methodology also applies for the latest active materials - high performance NFA BHJ OPVs.

## **5.2 Experimental details**

### **5.2.1 Solution preparation**

The PTB7-Th:PC<sub>70</sub>BM blend precursor solution was formed as described in section 4.2.1. The PM6:Y6 blend precursor solution was formed by dissolving 8 mg of PM6 and 9.6 mg of Y6 in 1.1 mL of chloroform to yield a 16 mgmL<sup>-1</sup> concentration with blend ratio of 1:1.2. CN was added to the solution as a solvent additive (0.5%, v/v). The solution was then allowed to stir overnight at room temperature. All the above processes were carried out in a glovebox under a nitrogen environment. The various Mg-doped ZnO precursor solutions were

formed by dissolving 0.1 g of a mixture of magnesium acetate tetrahydrate and zinc acetate dihydrate (with mass ratios of 0:100, 0.5:100, 1:100, 3:100, 5:100) along with 28  $\mu\text{L}$  of ethanolamine in 1 mL of 2-methoxyethanol. The solutions were then stirred vigorously for 12 hours at room temperature.

### **5.2.2 Device fabrication**

The first step to form the ITO/MgO:ZnO/Active layer (PTB7-Th:PC<sub>70</sub>BM or PM6:Y6)/MoO<sub>3</sub>/Au OPV structure (shown in Figure 28) was the cleaning of glass/ITO substrates in an ultra-sonicator sequentially, using soapy water, acetone and isopropanol for 10 minutes in each case. The substrates were then dried with a nitrogen spray gun and treated for 10 minutes in an oxygen plasma. The  $\sim 30$  nm thick ETL was then formed by spin-coating the ETL precursor solution on top of the substrate at 3000 rpm for 30 seconds, followed by 1 hour annealing at 150°C (or 300°C for high temperature studies) in air. Samples were then transferred to a nitrogen glovebox for the deposition of the active layer that was deposited via spin-coating. When PTB7-Th:PC<sub>70</sub>BM was employed, this was deposited at 670 rpm for 60 seconds. When PM6:Y6 was employed this was deposited at 3800 rpm for 60 seconds and following the spin-coating the PM6:Y6 layer was annealed inside the glovebox at 80°C for 5 minutes. After the formation of the active layer, samples were masked and loaded into a thermal evaporator (also housed in the nitrogen glovebox) evacuated to a residual pressure of  $1.6 \times 10^{-6}$  mbar before evaporation. A 9 nm thick MoO<sub>3</sub> layer was thermally evaporated with a rate of  $0.1 \text{ \AA s}^{-1}$ . This was followed by thermal evaporation of 80 nm of Au at a rate of  $0.2 \text{ \AA s}^{-1}$ . The active area of the devices is  $4.5 \text{ mm}^2$ . The OPV devices were completed by encapsulation with an epoxy resin and glass

cover slips and by application of electrical connection legs. For the XPS, UPS, AFM, Kelvin probe, optical transmittance and DC Hall measurements, samples were prepared by following the exact same recipe detailed above up to the point before the deposition of the active layer. For part of the AFM and transmittance investigations the blend layer was deposited as well. For the transmittance measurements, ETLs were formed on a glass substrate without ITO. Finally, for the ITO/PEDOT:PSS/PM6:Y6/Ca/Al structure used in the preliminary investigations, the PEDOT:PSS was filtered and deposited via spin coating at 5000 rpm and annealed at 150°C for 10 minutes in air and the Ca and Al were evaporated under  $1.6 \times 10^{-6}$  mbar pressure to form a 30 nm contact at a rate of  $0.4 \text{ \AA s}^{-1}$  and a 200 nm contact at a rate of  $2 \text{ \AA s}^{-1}$  respectively.

## **5.3 Preliminary investigations**

### **5.3.1 Optimisation of the PM6:Y6 active layer**

For the investigations in this chapter, in addition to the PTB7-Th:PC<sub>70</sub>BM benchmark system (developed as described in section 4.3), a testing system to be used as benchmark containing the latest high performing active layer blend PM6:Y6 is developed. This enables verification that an increased performance by doping the ETL with Mg can be achieved both by fullerene and NFA OPVs. Therefore, the starting point of the study is the optimisation of the performance of an OPV device based on a ZnO-only ETL and the PM6:Y6 active layer. The experimental strategies often quoted in the literature for the fabrication of state-of-the-art devices using the PM6:Y6 blend involve a precursor solution consisting of a donor acceptor ratio of 1:1.2 and with concentration of  $16 \text{ mg ml}^{-1}$  in chloroform with the solvent additive CN (0.5%, v/v). The above parameters have

also been used in this thesis. Typically spin-coating deposition at 3000 rpm and annealing treatment at 110°C for 10 minutes are used, however these parameters are varied between research groups. Hence, as a first step, I set out to establish the preparation settings that will work best with our in-house equipment. In the first iteration of experiments, the direct ITO/PEDOT:PSS/PM6:Y6/Ca/Al architecture was employed. Three different deposition speeds were used for the active layer, namely 3000, 4000 and 5000 rpm and upon deposition the layer was annealed for 10 minutes at either 130°C or 110°C. The PV performance indicators resulting from current-voltage characterisation of these devices under 1 Sun illumination are found in Table 6. The device fabricated with deposition at 3000 rpm and annealing temperature of 110°C (settings typically used in the literature) is outperformed by other devices signifying the importance of these preliminary investigations. The films annealed at 110°C exhibit a higher  $J_{sc}$  but lower  $V_{oc}$ . In both annealing temperature regimes, the sample deposited at 4000 rpm gives the best results. To elucidate the potential reasons behind the variation in performance for different annealing temperatures, films of the active layer deposited at 3000 rpm with the two different temperatures were prepared on glass and characterised using UV-Vis and AFM as shown in Figure 26.

The annealing temperature significantly changes the morphology of the active layer with a much larger phase separation appearing in the case of a higher annealing temperature at 130°C evidenced by the higher  $S_q$  of 50.5 nm as opposed to 1.1 nm for the case of annealing at 110°C. The change in morphology is further evidenced by the appearance of a peak at ~ 750 nm in the absorbance

spectra. The morphology achieved at higher temperature is not favourable since it results in a much lower  $J_{sc}$  and is detrimental to the PCE. The absorbance spectra also show that the optical density (corresponding to the thickness of the film) does not only depend on the spin coating deposition speed but also the annealing temperature, hence the right balance needs to be struck between annealing conditions and deposition to achieve the desired film thickness. Given the above observations, a new device was fabricated spin coated at 3000 rpm (still using the direct ITO/PEDOT:PSS/PM6:Y6/Ca/Al architecture) and annealed at the temperature of 100°C for 10 minutes resulting in a PCE of 5.49% with a  $J_{sc}$  of 19.85 mAcm<sup>-2</sup>,  $V_{oc}$  of 0.74 V and 0.37 FF. The lower annealing temperature enabled a significant performance increase compared to the devices of the previous study most likely due to an improved morphology that led to a higher  $J_{sc}$  and FF. With the attainment of the above performance, subsequent investigations were focused on the use of the active layer in an inverted architecture. Guided by the findings in the tests on direct structures, including the need to balance spin-coating speed and annealing temperature (since both affect final film thickness), using a temperature close to 100°C and deposition speeds between 3000 rpm and 4000 rpm was targeted and the testing of various annealing times was also introduced. These tests resulted in an optimised performance for the ITO/ZnO/PM6:Y6/MoO<sub>3</sub>/Au architecture of 5.21% PCE with a  $J_{sc}$  of 20.74 mAcm<sup>-2</sup>,  $V_{oc}$  of 737 mV and 0.34 FF. This benchmark device could be reproducibly achieved when 5 minutes annealing at 80°C was used and a spin coating speed of 3800 rpm for 60 seconds.

Table 6. Variation in key PV parameters of ITO/PEDOT:PSS/PM6:Y6/Ca/Al OPVs (at 1 Sun Illumination) with PM6:Y6 prepared at different deposition (dep.) and annealing (an.) settings.

Treatment	PCE (%)	J <sub>sc</sub> (mAcm <sup>-2</sup> )	V <sub>oc</sub> (V)	FF
Dep.: 3000 rpm, An.: 130°C	0.79	3.43	0.73	0.31
Dep.: 4000 rpm, An.: 130°C	1.01	5.34	0.73	0.26
Dep.: 5000 rpm, An.: 130°C	0.67	3.31	0.73	0.28
Dep.: 3000 rpm, An.: 110°C	0.80	6.14	0.61	0.21
Dep.: 4000 rpm, An.: 110°C	3.33	15.86	0.65	0.32
Dep.: 5000 rpm, An.: 110°C	2.77	15.02	0.65	0.29

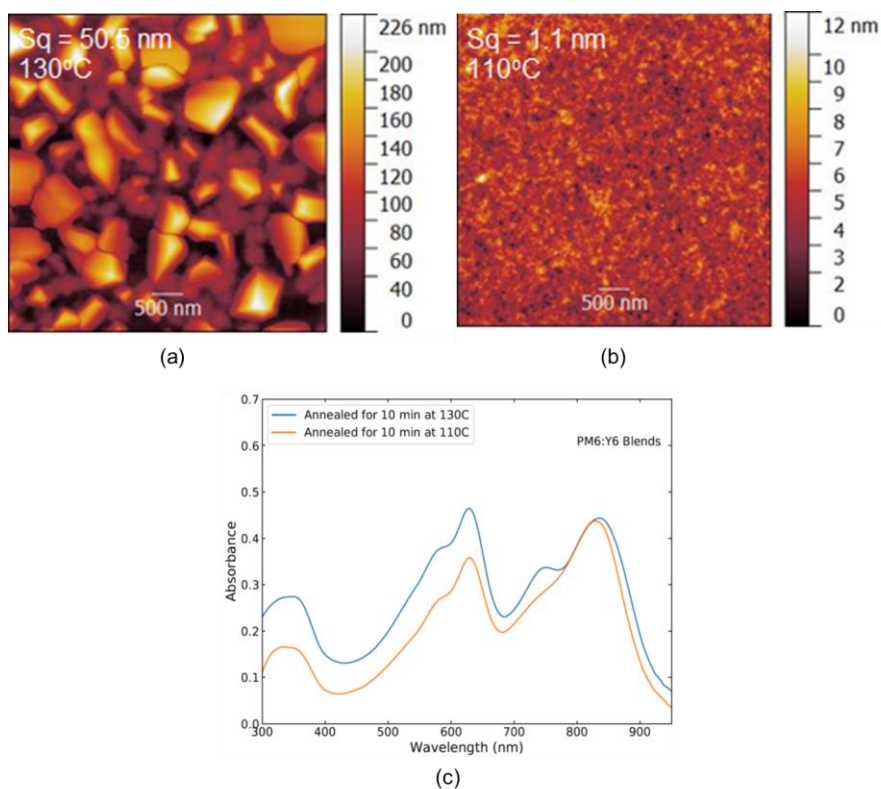


Figure 26. Tapping mode AFM images (1.6  $\mu\text{m}$  x 1.6  $\mu\text{m}$ ) of the topography of glass/PM6:Y6 (deposited at 3000 rpm) annealed at (a) 130°C and (b) 110°C. The annealing temperature results in a significantly different morphology. (c) Absorbance spectra of the two films.

### 5.3.2 Formation of the Mg-doped ZnO electron transport layers

To form the Mg-doped ZnO ETLs, the ratio of magnesium acetate tetrahydrate to zinc acetate dihydrate precursors used in the precursor solution of the ETL is varied to influence the amount of Mg doping in the ETL. Five different precursor mass ratios (defined as mass of the Mg precursor over the mass of the Zn precursor mixture) were tested in the range of 0-5:100, namely 0:100 (un-doped ZnO device), 0.5:100, 1:100, 3:100 and 5:100. As discussed in section 5.1 the level of Mg doping in the device governs its properties. Hence it is crucial to establish that the experimental protocol yields the stoichiometrically predicted ratio of Zn to Mg in the finalised films. Thin films of ITO/ETL with the aforementioned precursor ratios were characterised with XPS. The results of the XPS study are shown in Figure 27 & Table 7.

*Table 7. Relative concentration of the number of atoms for the atomic species found in the various Mg-doped films as measured by XPS.*

ETL (MgO:ZnO)	Zn2p (%)	Mg1s (%)	C1s (%)	O1s (%)
ZnO	38.2	0	15.1	46.7
(0.5:100)	40.3	0.4	11.6	47.8
(1:100)	38.6	0.5	12.6	48.3
(3:100)	37.7	1.1	12.3	48.8
(5:100)	34.9	1.9	13.2	50

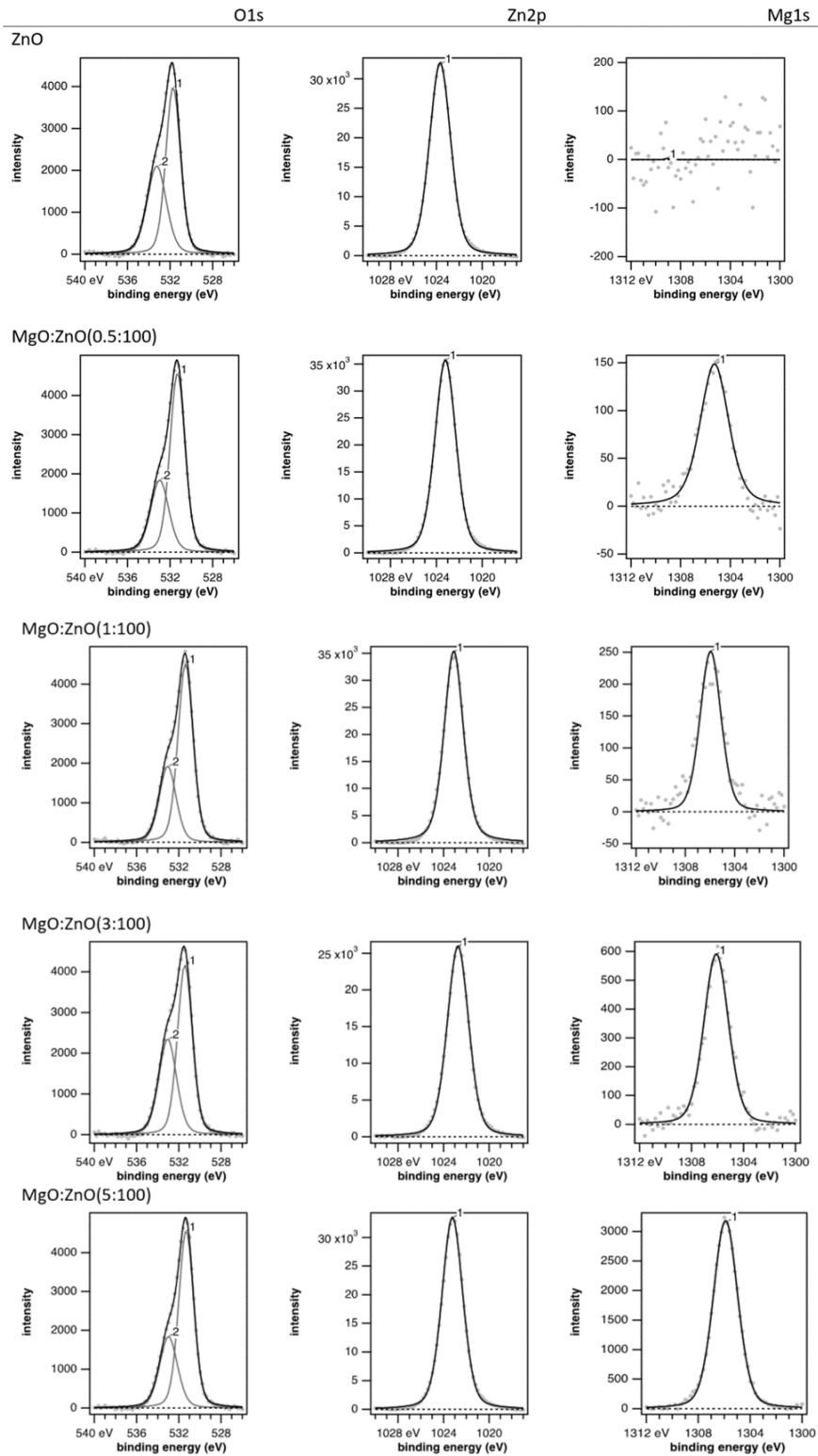


Figure 27. The O1s, Zn2p and Mg1s core level collected on samples via XPS. The scattered data points report the spectra upon background correction (Shirley function was subtracted). Lines are best fits (Voigt functions).

In Table 8, I demonstrate that for the selected precursor materials, the precursor mass ratio results in a similar stoichiometric atomic ratio of Zn:Mg (and corresponding Mg doping level) in the ETLs. The ratio of the Zn atomic signal divided by the Mg atomic signal as obtained from XPS (evaluated by the area of the Zn2p and Mg1s core level peaks) matches the stoichiometry atomic ratios of Zn:Mg expected from the precursors used to form the ETL precursor solutions within ~ 20%. The 0.5:100 sample exhibits a larger deviation between XPS and stoichiometric prediction.

*Table 8. Ratio of Zn:Mg content in the Mg-doped ZnO ETLs containing different amounts of the Mg dopant and the resulting doping level. The last column shows the ratio of Mg atoms to the sum of Mg and Zn atoms in each sample.*

ETL (MgO:ZnO)	Precursor mass ratio Zn:Mg	Stoichiometric atomic ratio Zn:Mg	XPS ratio of Zn:Mg	Stoichiometric Mg doping level (%)
(0.5:100)	200.0	195.4	100.8	0.51
(1:100)	100.0	97.7	77.2	1.01
(3:100)	33.3	32.6	34.3	2.98
(5:100)	20.0	19.5	18.4	4.87

I attribute such a discrepancy to the measurement uncertainty resulting from the weak XPS signal for the film containing a minute amount of Mg and to the difficulty of adding the exact weight of magnesium acetate tetrahydrate precursor, when measuring in the sub-milligram region. Having confirmed that the films have the expected amounts of doping, I employ them as ETLs in inverted OPVs (schematic in Figure 28).

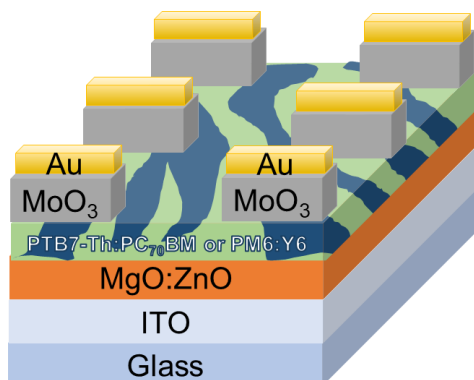


Figure 28. Schematic of the multi-layered structure of the OPV device. 5 Types of OPVs were tested, 4 with ETLs containing different amounts of Mg-doping in ZnO and an un-doped “control” device.

## 5.4 Results

### 5.4.1 Electrical characterisation of organic photovoltaic devices

The current density–voltage characteristics at 1 Sun illumination for PTB7-Th:PC<sub>70</sub>BM OPVs employing the un-doped ZnO ETL vs. the Mg-doped ZnO ETLs with varying Mg content are shown in Figure 29 (a). The corresponding average key PV performance indicators are displayed in Table 9.  $J_{sc}$  values were also extracted by the calculation of the photocurrent from EQE spectra (Figure 29 (b)) calculated to be  $8.36 \pm 0.09$ ,  $9.01 \pm 0.09$  and  $8.34 \pm 0.09$  mAcm<sup>-2</sup> for the ZnO-only device and the devices with an Mg-doped ZnO ETL formed from a MgO:ZnO precursor ratio of 1:100 and 5:100 respectively, which are in agreement with the extracted data from the current density–voltage investigations. The results confirm that an enhancement in the PCE of OPVs can be achieved by doping the ZnO ETL with Mg, via the direct addition of the MgO precursor to the ZnO precursor solution to form a single composite ETL using an annealing temperature of 150°C. The best performing device employing the Mg-doped ZnO

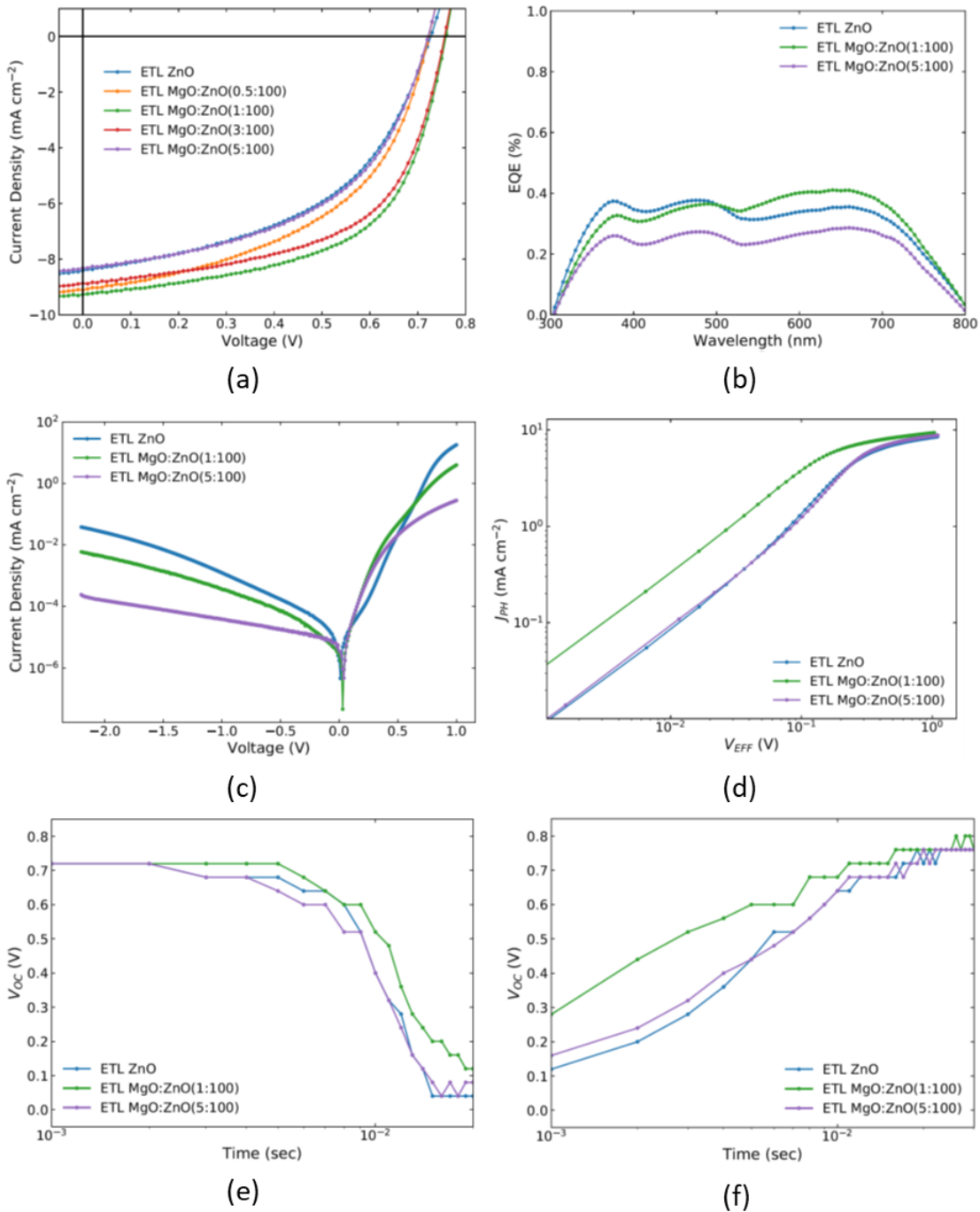


Figure 29. (a) Representative current density vs. voltage curves under 1 Sun illumination. Corresponding average key performance indicators for each type of ETL are reported in Table 9. Active layer: PTB7-Th:PC<sub>70</sub>BM. (b) Representative EQE curves (c) Representative current density–voltage curves in the dark. (d) Representative  $J_{PH}$  -  $V_{EFF}$  curves (e) Representative  $V_{OC}$  decay curves. (f) Representative  $V_{OC}$  rise curves.

Table 9. Extracted parameters for OPV devices presented in Figure 29.  $J_{sc}$  values were cross-checked with integrated EQE. Averages from 8 distinct devices with multiple measurements are reported for each device type

ETL (MgO:ZnO)	PCE (%)	$J_{sc}$ (mAcm <sup>-2</sup> )	$V_{oc}$ (V)	FF
ZnO	3.21 ± 0.07	8.46 ± 0.04	736 ± 1	0.52 ± 0.01
(0.5:100)	3.32 ± 0.07	8.99 ± 0.04	721 ± 1	0.51 ± 0.01
(1:100)	3.79 ± 0.07	9.05 ± 0.04	742 ± 1	0.56 ± 0.01
(3:100)	3.71 ± 0.07	8.80 ± 0.04	739 ± 1	0.57 ± 0.01
(5:100)	3.08 ± 0.07	8.44 ± 0.04	734 ± 1	0.50 ± 0.01

ETL was formed from a MgO:ZnO precursor ratio of 1:100 and has a relative increase in PCE of ~ 18% with respect to the control device employing the un-doped ZnO ETL. This is a consequence of an increase in the  $J_{sc}$ ,  $V_{oc}$  and FF. The device with the ETL formed from a MgO:ZnO precursor ratio of 5:100, is exhibiting lower PCE than the un-doped ZnO control. As the Mg content increases in the doped ZnO ETLs, the  $J_{sc}$  and FF of the devices increase, reaching a peak value in the region of 1-3% Mg doping level. The values of  $J_{sc}$  and FF then decrease with additional Mg doping.

For the  $V_{oc}$  there are slight variations between the devices, but similarly, the highest  $V_{oc}$  is achieved at 1-3% doping. These results are consistent with findings for Mg-doped ZnO ETLs formed with an annealing temperature of 150°C that were applied to PSCs.<sup>156</sup> The results reported herein demonstrate that this strategy can be viable in the case of OPVs as well. Further testing in a sub-

divided region of 1-3% Mg doping can be used to obtain an “optimised” doping level.

To identify the possible reasons behind the observed trends, the OPV devices of the un-doped ZnO ETL as well as devices of the Mg-doped ZnO ETLs formed from MgO:ZnO precursor ratios of 1:100 and 5:100 (that exhibited the biggest variations in OPV performance) have undergone further electrical testing. The incremental addition of Mg in the ZnO ETL leads to a corresponding reduction in the current leakage in the OPV device. This is evidenced in Figure 29 (c), where the (dark) current vs. voltage characteristics of the OPV diodes are shown. This reduced leakage is indicative of an increased  $R_{SH}$  (see Figure 12 (b)). The average current density at -1 V is  $-1.41 \times 10^{-3} \text{ mAcm}^{-2}$  for the un-doped ZnO ETL and decreases to  $-3.31 \times 10^{-4} \text{ mAcm}^{-2}$  for the Mg-doped ZnO ETL device formed from a MgO:ZnO precursor ratio of 1:100 and further decreases to  $-1.18 \times 10^{-4} \text{ mAcm}^{-2}$  for the Mg-doped ZnO ETL device formed from a MgO:ZnO precursor ratio of 5:100. The corresponding increase in  $R_{SH}$  is observed, with  $R_{SH}$  calculated as  $4.35 \times 10^6 \text{ } \Omega\text{cm}^2$ ,  $1.17 \times 10^7 \text{ } \Omega\text{cm}^2$  and  $1.42 \times 10^7 \text{ } \Omega\text{cm}^2$  respectively. To gain further insight in the extraction properties and the recombination in these devices, I have investigated the dependence of the  $J_{PH}$  on the  $V_{EFF}^{161}$  and measured the decay and rise times of the  $V_{OC}$ . Figure 29 (d) shows the variation of the  $J_{PH}$  with  $V_{EFF}$ . As expected from the PV characterisation, the Mg-doped ZnO ETL device formed from a MgO:ZnO precursor ratio of 1:100 shows the best performance.  $P_{DISS}$  increases from 95.85% for the un-doped ZnO device to 96.76% for the 1:100 Mg-doped ZnO device before decreasing to 95.83% at 5:100 Mg loading.

Figure 29 (e) and (f) demonstrate the time dependent  $V_{oc}$  decay and rise for the OPV devices. The OPV device based on the Mg-doped ZnO ETL formed from a MgO:ZnO precursor ratio of 1:100 takes the longest time to be completely discharged in comparison to the other devices. In addition, it requires a shorter rise time to arrive at the maximum  $V_{oc}$ . The trends observed in the  $V_{oc}$  rise and decay studies are indicative of reduced recombination in the 1:100 Mg-doped ZnO device.<sup>79, 162</sup> As OPV devices approach commercial application, an increasingly important property to test for is stability. To test for stability, devices were measured at the day of fabrication and then kept under identical conditions before re-measurement after 45 days. The percentage decrease in PCE when re-measuring devices was 16.2% for the device containing the un-doped ZnO ETL vs. 13.3% and 8.1% for the devices with ETLs formed from MgO:ZnO precursor ratios of 1:100 and 5:100 respectively. Therefore, the presence of Mg is favourable in terms of device stability as well.

Thin films of the un-doped ZnO ETL as well as films of the Mg-doped ZnO ETLs formed from MgO:ZnO precursor ratios of 1:100 and 5:100 have undergone further physical and optical characterisation to elucidate the origin of the observed trends.

## **5.4.2 Characterisation of electrodes**

### **UPS and Kelvin Probe**

To investigate the possible influence of Mg doping on the energetics of devices, the thin films were characterised with UPS, to extract the valence band onset and SECO (from which the work function is determined) as shown in Figure 30.

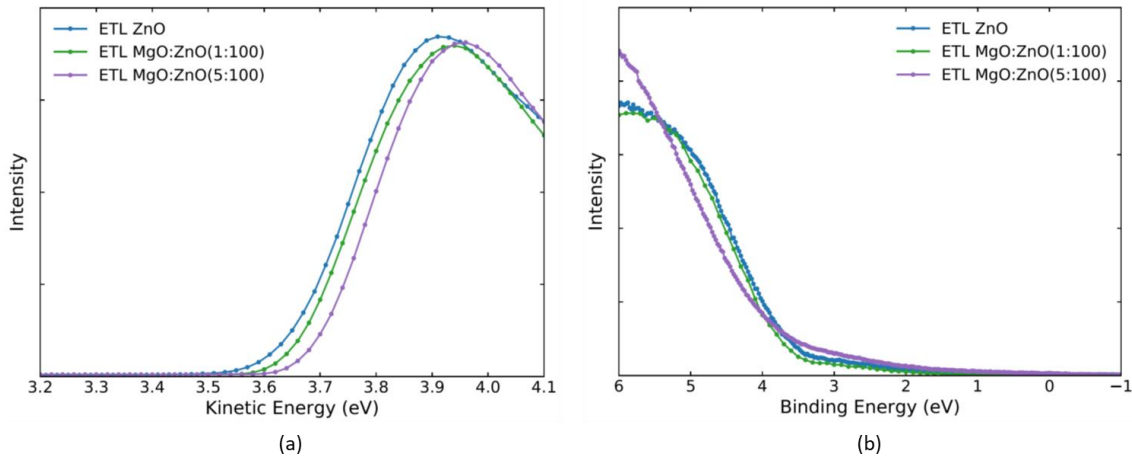


Figure 30. (a) The SECO spectra and (b) the valence band region spectra collected with UPS.

To cross reference the findings with regards to the work function, a Kelvin probe was also used to measure the contact potential difference with respect to a gold reference electrode. The results are summarised in Table 10.

Table 10. Work function measurements from Kelvin probe and UPS investigations, and valance band onset. No significant variation in the energetics of the device is observable.

ETL (MgO:ZnO)	$\Phi$ (eV) (Kelvin Probe)	$\Phi$ (eV) (UPS)	VB onset (eV)
ZnO	$4.2 \pm 0.1$	$3.6 \pm 0.1$	$3.6 \pm 0.1$
(1:100)	$4.1 \pm 0.1$	$3.6 \pm 0.1$	$3.6 \pm 0.1$
(5:100)	$4.1 \pm 0.1$	$3.7 \pm 0.1$	$3.6 \pm 0.1$

I attribute the minor discrepancies in the absolute values of work function obtained from UPS and Kelvin probe to the rather different measurement environments, and to the fact that the minimum value of the work function is measured with UPS, whereas Kelvin probe measurements yield a value averaged over the area of the electrode.<sup>163</sup> In any case, both techniques are suitable in detecting changes in work function between two samples that have

been prepared under the same conditions. Within the tested doping region both the UPS and Kelvin probe measurements show that the work function value remains constant. Mg-doping has been shown to alter the work function or conduction and valence band levels of electrodes but there are some conflicting reports on this issue.<sup>158, 159</sup> In this study, due to the limited amount of doping (<5%), no change is observed in these parameters. Therefore, it is unlikely that the performance changes observed in the PV measurements, relate to the tuning in the energetics of the device.

### **Optical spectroscopy**

To assess the effect of Mg doping on the optical properties of the ETLs, transmission measurements were carried out as shown in Figure 31. The Mg-doped ZnO ETLs show slightly increased transmittance compared to the un-doped ZnO ETL in the region of 325-400 nm. The observed blue shift with increasing Mg content, is consistent with previous literature,<sup>159</sup> however the shift is not very significant (~ 9 nm), a circumstance that I attribute to the amount of Mg doping being minimal. From the Tauc plots (Figure 31 (c)) changes in energetics are shown not to exceed 0.1 eV (equivalent to the error on UPS and Kelvin probe measurements) corroborating that for the minimal Mg doping used in the investigations no significant changes in the energetics of the devices are observed. I also carried out transmission measurements on the films after the deposition of a PTB7-Th:PC<sub>70</sub>BM blend layer on top of the un-doped and Mg-doped ZnO ETLs (Figure 31 (d)). The samples incorporating the Mg-doped ZnO show a slightly increased transmittance (~ 8% in relative terms) throughout the

tested spectral region (300 – 900 nm). The increase in  $J_{SC}$  observed in the OPV devices is thus not associated with increased absorption in the active layer blend.

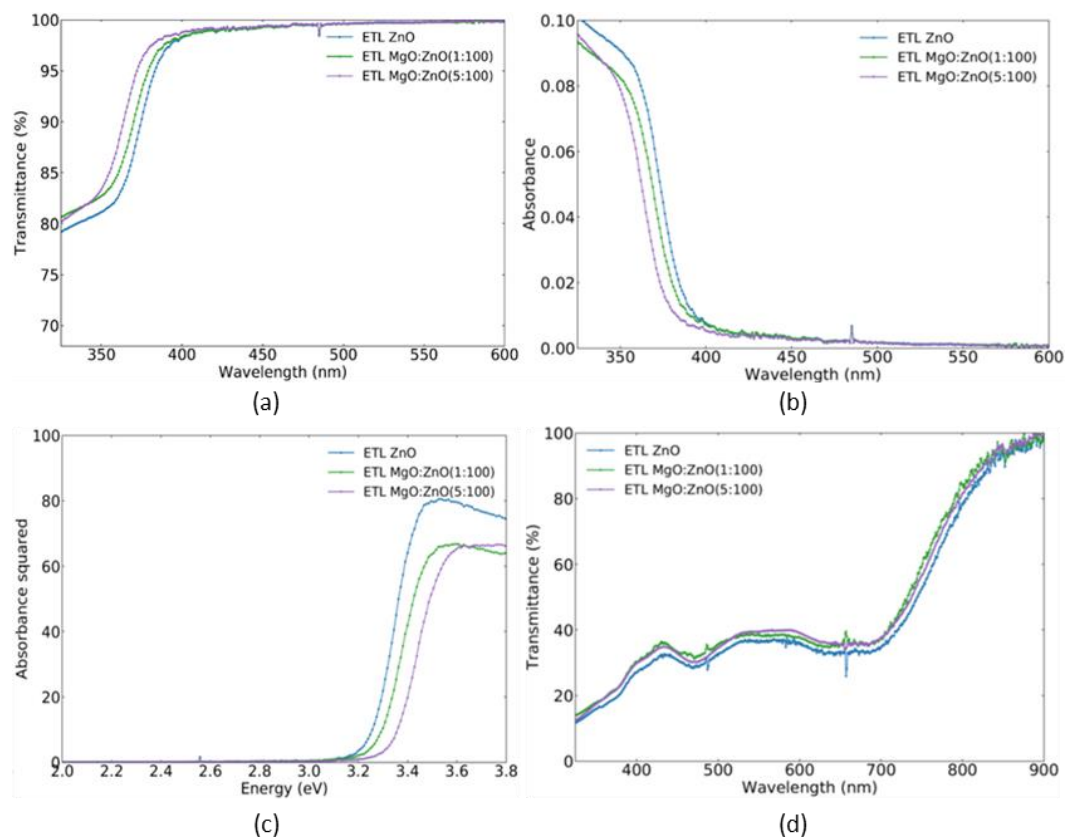


Figure 31. (a) Transmission spectra of thin films of ZnO and Mg-doped ZnO. There is a blue-shift in the spectrum with increasing Mg-doping. (b) Transmittance spectra presented in the form of Absorbance (not corrected for reflectance) and (c) corresponding Tauc plots. (d) Transmission spectra of ITO/ZnO/PTB7-Th:PC<sub>70</sub>BM, ITO/Mg-doped (1:100) ZnO/PTB7-Th:PC<sub>70</sub>BM and ITO/Mg-doped (5:100) ZnO/PTB7-Th:PC<sub>70</sub>BM films.

## AFM

I investigated potential variations in the surface morphology and  $S_q$  of the PTB7-Th:PC<sub>70</sub>BM blend on top of the un-doped and Mg-doped ZnO ETLs, via tapping mode AFM and I report the corresponding images in Figure 32 (a, b, c). There are only insignificant variations in  $S_q$  between the films (smaller than the uncertainties), hence, it can be inferred that for the length scales investigated

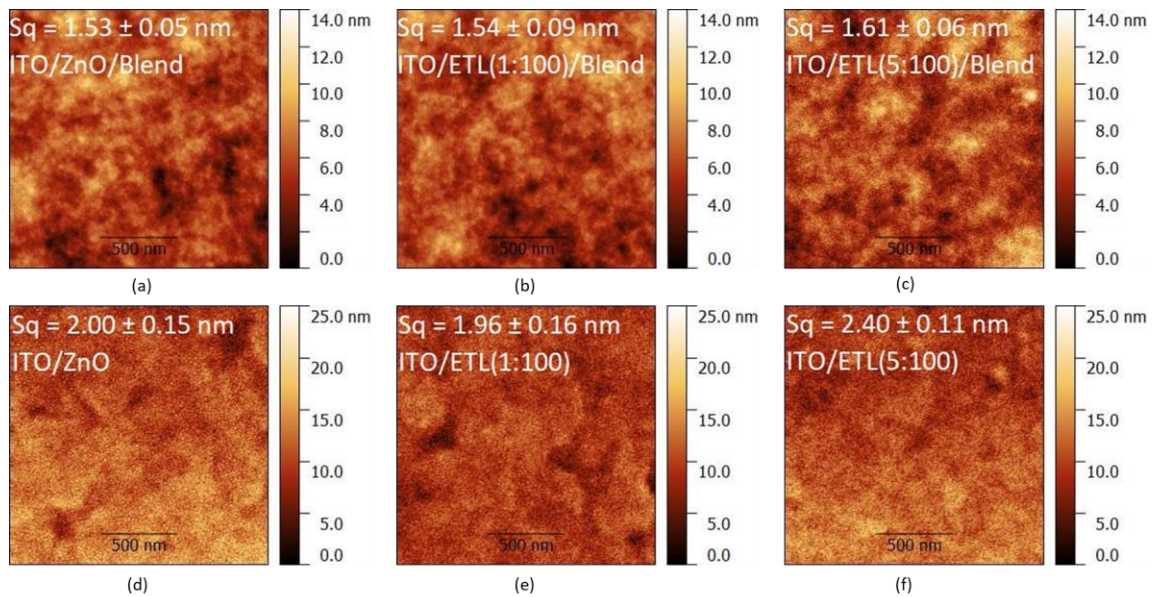


Figure 32. Tapping mode AFM images ( $1.6 \mu\text{m} \times 1.6 \mu\text{m}$ , annotated with the corresponding  $S_q$ ) of the topography of (a) ITO/ZnO/PTB7-Th:PC<sub>70</sub>BM, (b) ITO/Mg-doped (1:100) ZnO/PTB7-Th:PC<sub>70</sub>BM, (c) ITO/Mg-doped (5:100) ZnO/PTB7-Th:PC<sub>70</sub>BM, (d) ITO/ZnO, (e) ITO/Mg-doped (1:100) ZnO and (f) ITO/Mg-doped (5:100) ZnO. There is no significant variation of  $S_q$  between the bare ITO/ZnO and ITO/Mg-doped (1:100) ZnO films, although  $S_q$  is  $\sim 20\%$  larger for the ITO/Mg-doped (5:100) ZnO films. Mg-doping of the ETL does not influence the morphology of the PTB7-Th:PC<sub>70</sub>BM blend for the investigated length scales.

here, Mg-doping of the ETL does not influence the morphology of the blend. I report the AFM images of the corresponding ETL films without the blend on top in Figure 32 (d, e, f) respectively for the different Mg loadings. The variation in  $S_q$  between the ETL formed from a MgO:ZnO precursor ratio of 1:100 and the undoped ZnO ETL is smaller than the uncertainties in the measurements, however, there is a  $\sim 20\%$  increase in  $S_q$  for the ETL formed from a MgO:ZnO precursor ratio of 5:100. Such an increase in  $S_q$  is indicative of a less uniform and less homogeneous surface of the ETL at  $\sim 5\%$  loading, with potential phase separation and formation of MgO-rich regions which may influence negatively the OPV performance.

## Hall measurements

The van der Pauw method was used to assess the electrical properties of the films. The extracted parameters from the measurement are shown in Table 11. Mg doping leads to a higher carrier concentration in the thin films. In general, Hall mobility is expected to decrease with doping due to enhanced scattering (as seen in the case of doping Si for example). Hence the film formed from the MgO:ZnO precursor ratio of 1:100 exhibits a lower Hall mobility than the un-doped ZnO film. The film formed from the MgO:ZnO precursor ratio of 5:100, even though expected to show an even lower Hall mobility, exhibits a Hall mobility that it is very similar to the un-doped ZnO thin film. This might be the result of a potential phase separation between ZnO and MgO that appears to occur for this higher level of Mg doping, as suggested by the rougher morphology of these films observed in the AFM investigation. The resistivity of a film is proportional to the inverse of the product of carrier concentration and mobility. This leads to the highest resistivity obtained when the ETL is formed from the MgO:ZnO precursor ratio of 1:100.

Table 11. Hall measurements. The Hall mobility, carrier concentration and resistivity values were extracted from the measurement.

ETL (MgO:ZnO)	Hall mobility ( $\text{cm}^2\text{V}^{-1}\text{s}^{-1}$ )	Carrier concentration ( $\times 10^{21} \text{ cm}^{-3}$ )	Resistivity ( $\times 10^{-5} \Omega\text{cm}$ )
ZnO	$39.8 \pm 0.05$	$1.86 \pm 0.03$	$8.44 \pm 0.01$
(1:100)	$34.8 \pm 0.05$	$2.00 \pm 0.11$	$8.97 \pm 0.01$
(5:100)	$40.9 \pm 0.05$	$2.03 \pm 0.06$	$7.51 \pm 0.01$

### **5.4.3 Discussion: Origin of performance improvement and comparison with previous literature**

The results above show that low-temperature annealing of a mixed MgO:ZnO precursor leads to a significant increase of the performance parameters of OPVs incorporating such an ETL, and in particular an ~ 18% relative increase of the PCE with respect to un-doped ZnO ETLs for films with a ~ 1% atomic Mg doping. Interestingly, analysis of the electrical properties of the OPVs reveal a higher  $R_{SH}$  (accounting for the reduced losses for such devices, also evidenced by the faster increase of the  $V_{OC}$  upon light switch-on and the slower  $V_{OC}$  decay after light switch-off, as well as by the decreased dark current in reverse bias (Figure 29 (c)). The increased  $J_{PH}$  on the other hand (Figure 29 (d)) indicates a reduction in  $R_S$  which would also lead to an increase of both the  $J_{SC}$  and of the FF, as indeed observed. Of course, the increased  $R_{SH}$  also accounts for the increased  $V_{OC}$ , and  $J_{sc}$ .

The electrode characterisation revealed that in the case of using an Mg-doping strategy to improve ZnO ETLs, the improvement is not a result of an increase in transmittance of the semi-transparent electrode or a favourable change in active layer blend morphology. The device energetics (work function modification) also seem to be unaffected by the limited addition of Mg doping used in the investigations. To gather some insight into the microscopic origin of the reduced recombination losses within the OPV devices I note that the properties of ZnO films are well-established to be highly dependent on the presence and/or concentration of defects (traps) such as oxygen vacancies, zinc interstitials

and/or other dopants.<sup>164</sup> For example, it has been proposed that Mg can reduce the density of oxygen vacancies in ZnO nanorods.<sup>165</sup> In our case as well, I suggest that Mg doping compensates oxygen vacancies which may act as charge recombination centres. In addition, I note that bulk MgO is characterised by a rather large ionisation potential ( $\sim 10$  eV) compared to ZnO ( $\sim 7.6$  eV), thereby suggesting significantly better hole-blocking properties for any MgO-rich region of the modified electrodes, which would also contribute to reduction of PV losses linked to hole currents flowing through the electron-collecting electrode. The question arises as to how much Mg will provide optimum results. My data show that the best results are obtained with a Mg loading between  $\sim 1$  and 3%, but that when increasing this to  $\sim 5\%$ , despite a higher  $R_{SH}$  (expected due to the insulating nature of MgO) carrier recombination becomes significant (e.g. from Figure 29 (e) & (f)) eventually leading to a lower PCE. It is interesting that the Hall (lateral) resistivity at  $\sim 5\%$  Mg is decreased with respect to un-doped and  $\sim 1\%$ -doped ETLs, with a concomitant increase of the electron mobility, thereby hinting at a potential overcompensation of the oxygen vacancies, with a concomitant increase of carrier recombination centres. This is also corroborated by the morphology changes visible in AFM images at such a concentration (Figure 32). In a study by Kim et al where Mg-doped ZnO nanoparticle (NP) thin-film transistors were fabricated and characterised using XPS, it is evident that a change between 1% to 5% doping significantly affects the concentration of oxygen vacancies, corroborating the above findings.<sup>166</sup> In summary I propose that  $\sim 1\%$  Mg doping strikes the “right balance” between the various processes at play,

i.e., extraction of the electrons, blocking of the holes, and hole-electron recombination.

This result is different from the previous studies by Yin et al.<sup>158</sup> and by MacLeod et al.<sup>159</sup> where Mg-doped ZnO ETLs have been applied to OPVs and a much higher doping was present in the ETL to optimise the PCE. The difference in the optimum doping level range for the ETL between the study presented herein and the previous studies in the literature are probably related to the lower annealing temperature used during our device fabrication. To gather some insight to the interplay of annealing temperature and required level of doping, I have also tested OPVs containing ETLs formed with an annealing temperature of 300°C. A comparison between OPVs with ETLs prepared at 300°C and 150°C is shown in Figure 33 and Table 12. The findings suggest that the optimum Mg loading for the ETL that is required to maximise the PCE depends on the annealing temperature. For the key temperature of 150°C (that enables compatibility with the flexible substrates) the optimum loading is 1-3%. However, at 300°C this is no longer the optimum loading. It is also useful to note that for the un-doped ZnO ETL and the ETL formed from a MgO:ZnO precursor ratio 1:100 (that shows the highest performance) annealing at 150°C rather than 300°C yields devices with higher PCE. The increase in efficiency when comparing the PCE of the un-doped ZnO ETL and the ETL formed from a MgO:ZnO precursor ratio of 1:100 annealed at 150°C for this new batch tested, differs from the 18% reported earlier in terms of absolute value, however the overall efficiency trend between the different Mg doping amounts is consistent.

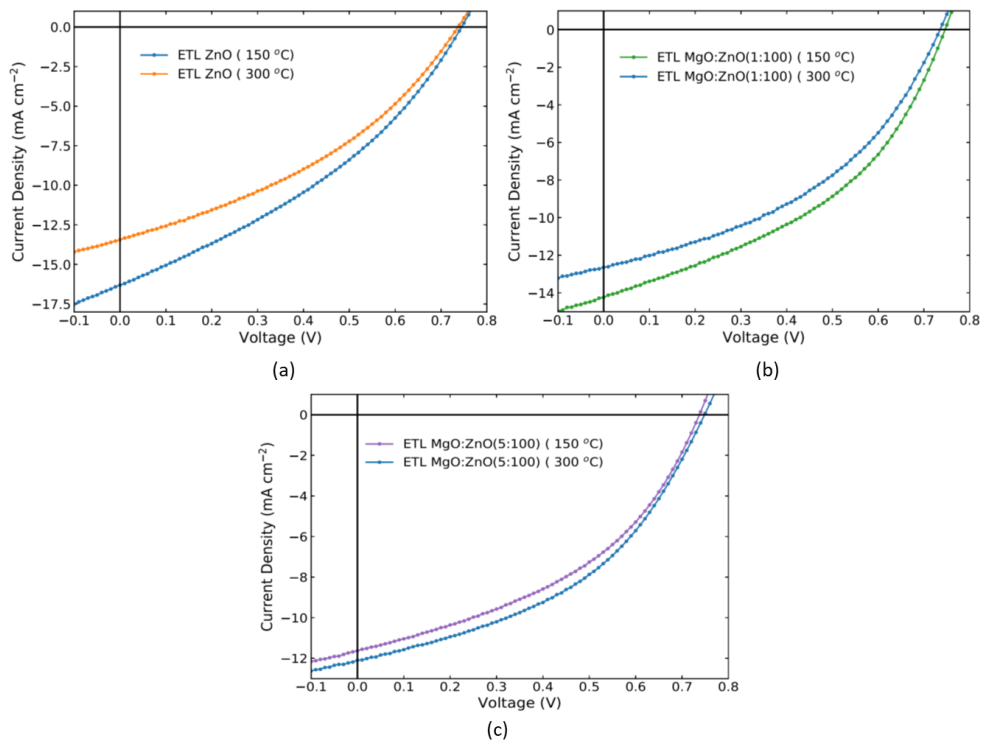


Figure 33. Representative current density vs. voltage curves under 1 Sun illumination comparing OPVs with the ETL annealed at temperatures of 150°C vs. 300°C for (a) ZnO-only ETLs, and ETLs formed from MgO:ZnO precursor ratios of (b) 1:100 and (c) 5:100. Active layer: PTB7-Th:PC<sub>70</sub>BM.

Table 12 Extracted parameters for OPV devices presented in Figure 33

ETL(MgO:ZnO) (Annealing Temp.)	PCE (%)	J <sub>sc</sub> (mAcm <sup>-2</sup> )	V <sub>oc</sub> (V)	FF
ZnO (150°C)	4.26 ± 0.13	15.98 ± 0.72	747 ± 4	0.36 ± 0.01
ZnO (300°C)	4.00 ± 0.13	13.86 ± 0.72	741 ± 4	0.39 ± 0.01
(1:100) (150°C)	4.37 ± 0.13	14.48 ± 0.72	745 ± 4	0.41 ± 0.01
(1:100) (300°C)	3.73 ± 0.13	12.62 ± 0.72	734 ± 4	0.40 ± 0.01
(5:100) (150°C)	3.58 ± 0.13	11.62 ± 0.72	736 ± 4	0.42 ± 0.01
(5:100) (300°C)	3.77 ± 0.13	12.05 ± 0.72	745 ± 4	0.42 ± 0.01

The annealing temperature might play such a significant role in determining the optimum Mg loading for Mg-doped ZnO ETLs due to the degree of decomposition of the zinc and magnesium acetate precursors achieved at different temperatures. At 300°C crystalline ZnO starts to form hence the presence of only a limited amount of Mg might hinder crystallinity and thus performance, whereas much higher Mg doping might lead to a favourable crystalline structure. In addition, much higher levels of Mg (than in the range tested herein) have been shown to affect other characteristics of the films (such as its work function, bandgap, mobility, etc.) and the different balance of all these factors leads to the necessity of a different (and higher) Mg loading to achieve an increase in performance via Mg doping at 300°C. At 150°C the acetates do not decompose fully, and the benefit of limited Mg addition is likely to be related to filling of oxygen vacancies with optimisation achieved in the doping range of 1-3%. Higher doping percentages for this temperature regime may hinder performance due to an overcompensation of the oxygen vacancies. A different annealing temperature will also affect the number of oxygen vacancies for the same doping amount, as shown by Kim et al.<sup>166</sup> Determining the correlation between temperature and Mg loading required to optimise the PCE of OPVs, would require a more exhaustive study that is beyond the scope of this chapter.

#### **5.4.4 Extending the use of Mg-doped ZnO to PM6:Y6 (non-fullerene) organic photovoltaics**

The applicability of the Mg-doped ZnO ETLs has also been tested and shown to be successful for the case where the NFA PM6:Y6 system has been used as the active layer in OPV devices. Similarly to the PTB7-Th:PC<sub>70</sub>BM system, doping of

Mg in the ZnO ETL can result to enhancement in the PCE for ETLs annealed at the temperature of 150°C. The current density–voltage characteristics at 1 Sun illumination for PM6:Y6 OPVs employing the un-doped ZnO ETL vs. the Mg-doped ZnO ETLs with varying Mg content are shown in Figure 34 (a). The corresponding average key PV performance indicators are displayed in Table 13. The trends observed for the PM6:Y6 devices are similar to those of the PTB7-Th:PC<sub>70</sub>BM devices in terms of J<sub>sc</sub> and the FF. J<sub>sc</sub> values were also extracted by the calculation of the photocurrent from EQE spectra (Figure 34 (b)) calculated to be  $19.8 \pm 1.0$ ,  $22.3 \pm 1.0$  and  $19.7 \pm 1.0$  mAcm<sup>-2</sup> for the ZnO-only device and the devices with an Mg-doped ZnO ETL formed from a MgO:ZnO precursor ratio of 1:100 and 5:100 respectively, which are in agreement with the extracted data from the current density–voltage investigations. The V<sub>oc</sub> of the measured devices (for each type of ETL) varied significantly leading to a large uncertainty in the value of the V<sub>oc</sub> preventing solid conclusions regarding the V<sub>oc</sub> trend. Nevertheless, in terms of PCE and similarly to the PTB7-Th:PC<sub>70</sub>BM OPVs, the best performing devices are the ones that employ an Mg-doped ZnO ETL formed from a MgO:ZnO precursor ratio of 1:100 yielding a PCE of  $5.48 \pm 0.53\%$ . The increase in PCE is ~ 5% with respect to the device employing the un-doped ZnO ETL. This is lower than the one observed with the PTB7-Th:PC<sub>70</sub>BM devices but still significant. In addition to the OPV performance characterisation, I have also carried out further electrical testing of the PM6:Y6 based devices including current density–voltage curves in the dark (Figure 34 (c)) J<sub>PH</sub> - V<sub>EFF</sub> curves (Figure 34 (d)), as well as V<sub>oc</sub> decay (Figure 34 (e)) and rise curves (Figure 34 (f)).

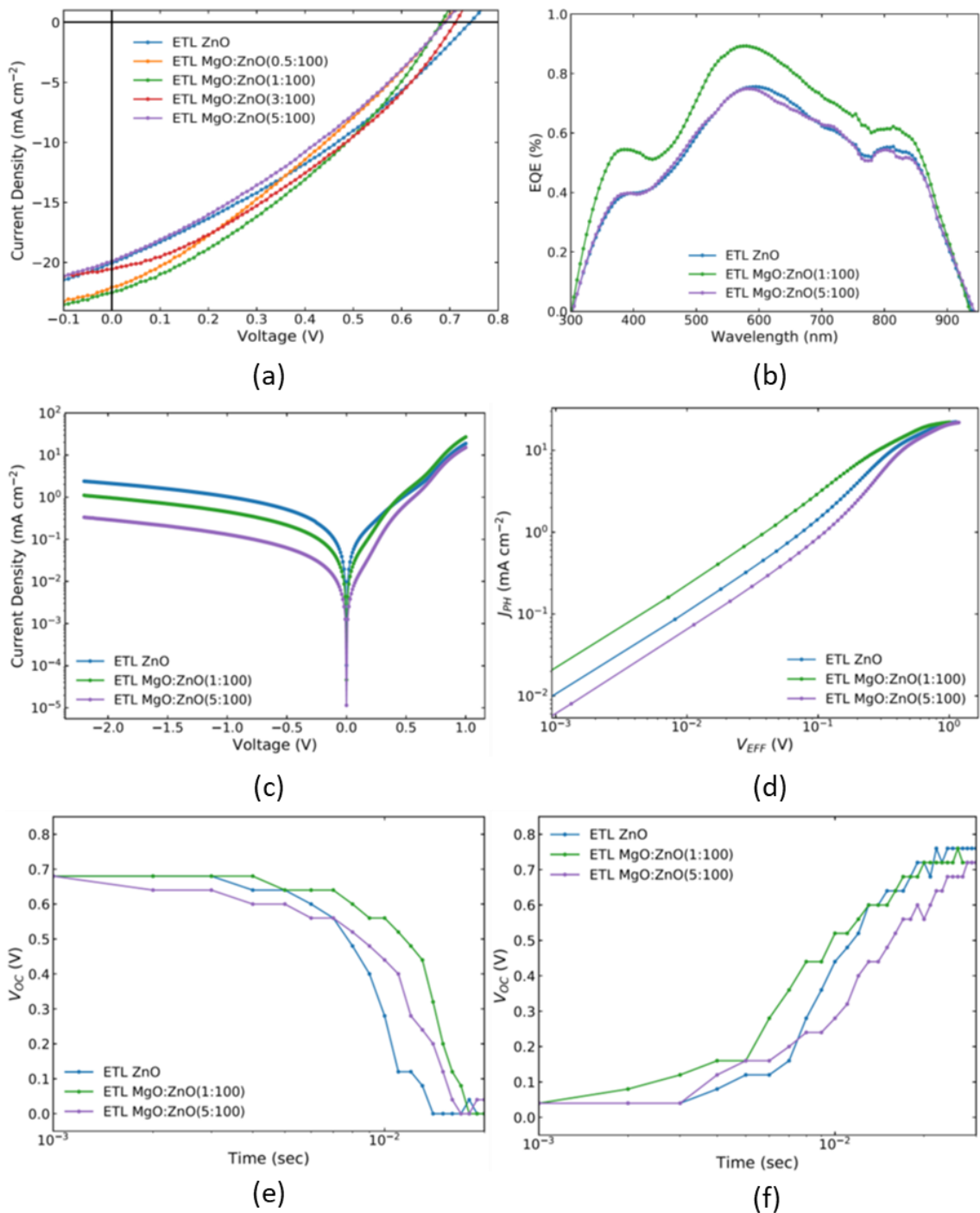


Figure 34. (a) Representative current density vs. voltage curves under 1 Sun illumination for OPV devices based on a PM6:Y6 active layer with ETLs containing various Mg doping levels. (b) Representative EQE curves (c) Representative current density–voltage curves in the dark. (d) Representative  $J_{PH}$  -  $V_{EFF}$  curves. (e) Representative  $V_{OC}$  decay curves. (e) Representative  $V_{OC}$  rise curves.

Table 13. Extracted parameters for OPV devices presented in Figure 34 (a). Averages from 8 distinct devices with multiple measurements are reported for each device type.

ETL (MgO:ZnO)	PCE (%)	J <sub>sc</sub> (mAcm <sup>-2</sup> )	V <sub>oc</sub> (V)	FF
ZnO	5.21 ± 0.53	20.74 ± 0.48	737 ± 35	0.34 ± 0.02
(0.5:100)	5.09 ± 0.53	21.97 ± 0.48	704 ± 35	0.33 ± 0.02
(1:100)	5.48 ± 0.53	22.21 ± 0.48	688 ± 35	0.36 ± 0.02
(3:100)	5.36 ± 0.53	20.91 ± 0.48	693 ± 35	0.37 ± 0.02
(5:100)	4.93 ± 0.53	19.97 ± 0.48	710 ± 35	0.35 ± 0.02

Similarly to the PTB7-Th:PC<sub>70</sub>BM devices, the incremental addition of Mg in the ZnO ETL leads to a reduction in the current leakage and a corresponding increase in the R<sub>SH</sub>. The average current density at -1 V is -1.04 mAcm<sup>-2</sup> for the un-doped ZnO ETL and decreases to -0.50 mAcm<sup>-2</sup> for the Mg-doped ZnO ETL device formed from a MgO:ZnO precursor ratio of 1:100 and further decreases to -0.18 mAcm<sup>-2</sup> for the Mg-doped ZnO ETL device formed from a MgO:ZnO precursor ratio of 5:100. The corresponding increase in R<sub>SH</sub> is observed, with R<sub>SH</sub> calculated as 1142 Ωcm<sup>2</sup>, 2650 Ωcm<sup>2</sup> and 6192 Ωcm<sup>2</sup> respectively. The extracted P<sub>DISS</sub> from the J<sub>PH</sub> - V<sub>EFF</sub> investigations, increases from 94.88% for the un-doped ZnO device to 95.72% for the 1:100 Mg-doped ZnO device before decreasing to 94.37% at 5:100 Mg loading in a similar trend to PTB7-Th:PC<sub>70</sub>BM devices. Lastly, in the time dependent V<sub>oc</sub> decay curve, the OPV device based on the Mg-doped ZnO ETL formed from a MgO:ZnO precursor ratio of 1:100 takes the longest time to be completely discharged in comparison to the other devices and rise times

are similar between the un-doped ZnO device and the 1:100 Mg-doped ZnO device and slower for the 5:100 doped ZnO device.

## 5.5 Conclusions

In this chapter, I have demonstrated that Mg acetate can be directly added to ZnO precursor solutions to form Mg-doped ZnO ETLs for OPVs with a reduced annealing temperature of 150°C. Not only is this appealing for low-temperature industrial manufacturing and greater sustainability, but also affords greater OPV PCEs. I obtained my best results with a 1:100 MgO:ZnO precursor concentrations and this yields a relative increase in PCE of ~ 18% compared to devices incorporating un-doped ZnO ETLs. The Mg-doped devices show enhanced stability, and this strategy is viable for OPVs based both on fullerene and NFA active layer blends. The relative improvement in PCE exceeds the one reported in chapter 4 (~ 10%) when MgO was used on top of ZnO (i.e., effectively forming a bilayer). The observed increase in PCE is a result of an enhanced  $J_{sc}$ ,  $V_{oc}$  and FF, which I can trace down to an improved contact with the active layer exhibiting decreased recombination losses via the passivation of traps (most likely due to the filling of oxygen vacancies which act as charge recombination centres) and a decreased leakage current. Doping with low levels of Mg does not significantly affect the work function, transmittance or blend morphology. My results show that for achieving better performance the Mg doping needs to be limited when the annealing temperature used is 150°C, as doping in the ETL formed from a MgO:ZnO precursor ratio of 5:100 is already excessive and can hinder performance.

# 6 Conclusions and outlook

## 6.1 Summary and conclusions

This thesis focussed on the emerging PV technology of OPVs. More specifically, OPVs were improved via the development of MgO modified ZnO ETLs that were fabricated at low temperature (150°C).

In chapter 1, an overview of the thesis and an outline of its structure are given.

In chapter 2 a general overview of PV technologies and the current PV market has been provided. The necessary characteristics and motivation for future PVs beyond those based on silicon have also been discussed and the key emerging PV technologies were identified with a special focus given to two promising candidates: PSCs and OPVs. Following this, OS and their corresponding diodes have been introduced. Next, a historic review of the major achievements of OPV research (including the recent discovery of NFAs) and the currently accepted working principles of OPVs have been recounted. Finally, the discussion was focused on the characteristics of ETLs and the different strategies by which they can be modified to bring about OPV performance enhancements.

In chapter 3, the main methodologies used to characterise OPV devices and ETLs have been presented in detail. These include optoelectronic methods such as current density-voltage,  $V_{oc}$  decay and rise, EQE and EA spectroscopy measurements as well as photophysical methods such as Kelvin probe, UV-VIS

absorption spectroscopy, profilometry and AFM measurements. Experiments carried out by collaborators that include XPS, UPS and Hall measurements have also been briefly described.

In chapters 4 and 5, I explore two different strategies of modifying ZnO ETLs with MgO. Low cost, non-toxic MgO has a great track record as an additive or bilayer in ETLs for optoelectronic devices. It offers the key advantages of good compatibility with other metal oxides and a high ionisation potential ( $\sim 10$  eV) that allow it to act as a good hole blocker, hence the motivation behind its use in this thesis.

In chapter 4, I explore the strategy of forming a bilayer ETL to improve OPV performance, by employing ultrathin ( $\sim 10$  nm) MgO to serve as the top component of a ZnO/MgO bilayer ETL. Initially, I review the literature of bilayer ETLs based on ZnO and prior uses of metal oxide/MgO bilayer ETLs in optoelectronic devices. Next, I detail the experimental procedures used to fabricate devices and samples and present preliminary investigations that describe the optimisation studies that led to the ITO/ZnO/PTB7-Th:PC<sub>70</sub>BM/MoO<sub>3</sub>/Au OPV device that is used as benchmark for the rest of the investigations. Current density-voltage investigations reveal that application of the MgO interlayer boosts the  $J_{SC}$  and FF enhancing the PCE by  $\sim 10\%$  and that the MgO containing devices exhibit a higher  $R_{SH}$ . Further electrical characterisation and analysis of devices including  $J_{PH} - V_{EFF}$  studies and  $V_{OC}$  decay and rise curves demonstrate the reduction in the recombination losses and

$R_s$  in devices that include the MgO interlayer. To investigate the origin of the performance enhancement resulting from the addition of MgO in my device structure, in addition to the above studies, I present AFM, cAFM, Kelvin probe and optical spectroscopy (namely transmittance, absorbance and EA) measurements. These measurements enable us to demonstrate that the MgO addition does not affect the photon capture rate and blend morphology, but the ZnO/MgO ETL has a more uniform top surface and a lower work function (that seems to be associated with the electrostatic compressive effect of MgO on metal oxides) manifested as an increase in  $V_{BI}$ . In addition, I show that the MgO layer is successful despite being insulating, because it only partially covers the ZnO allowing for sufficient “charge transparency”. OPVs with the modified ETL outperform those based on a single ZnO ETL both for fullerene and NFA active layer blends.

In chapter 5, I explore the strategy of doping the ETL to improve OPV performance, by directly adding an Mg precursor in a ZnO precursor solution to form an Mg-doped ZnO ETL. Importantly, our ETL is treated with an annealing temperature of only 150°C which sets it apart from previously demonstrated Mg-doped ZnO ETLs in the literature that required higher temperature treatments of ~ 300°C. Initially, I review a number of successful dopants for ZnO ETLs and prior uses of the Mg-doped ZnO ETLs in optoelectronic devices. Next, I detail the experimental procedures used to fabricate devices and samples and present preliminary investigations that describe the optimisation studies that led to the ITO/ZnO/PM6:Y6/MoO<sub>3</sub>/Au OPV device that is used as benchmark for NFA

based OPVs in my investigations. Confirmation that the tested Mg-doped ZnO ETLs had the expected amounts of doping was achieved using XPS. The current density - voltage investigations performed, reveal that doping leads to a concomitant increase of the  $J_{SC}$ , FF and  $V_{OC}$ , enhancing the PCE by ~ 18% and that the Mg-doped devices exhibit a higher  $R_{SH}$ . Mg-doped devices also show greater stability with respect to un-doped devices. The best results were obtained when the ZnO ETL is doped with ~ 1% of Mg. Without changing the work function of the ETL, the morphology of the active layer or affect the photon capture rate – as verified by UPS, Kelvin probe, AFM and optical spectroscopy– I show that this level of Mg doping enables the formation of an improved electrode that leads to reduced recombination losses and decreased  $R_S$  in OPV devices, most likely due to the filling of oxygen vacancies in the ZnO ETL. This is demonstrated by analysing the dependence of the  $J_{PH}$  on  $V_{EFF}$ , and by measurements of the  $V_{OC}$  decay and rise. Furthermore, Hall measurements indicate that Mg doping of ZnO ETLs increases the concentration of charge carriers in the ETL. The reason behind the hindering of performance with excess addition of Mg dopant (~ 5%) in the ZnO ETL and the interplay of “optimal” doping with respect to the employed annealing temperature are also discussed. Finally, NFA OPVs with the modified ETL are also tested and shown to outperform their un-doped ZnO ETL counterparts.

Through my investigations, I demonstrate that high transparency and a high ionisation potential can serve as useful design rules for materials used to modify ETLs but more importantly my study serves as proof that inspiration for future

ETLs for OPVs can be drawn by novelties in other solution-processed emerging PV systems and that transfer of developments from one field to another can be a viable route to synergistically push the performance boundaries of these promising technologies to even higher levels. My work provides an industrially scalable approach to electrodes for high-performance OPVs and is in principle applicable to both top and bottom contact electrodes.

## 6.2 Future research

Silicon PVs will continue to serve us for years to come, however, as discussed in chapter 2, the urgency of climate change and the looming energy crisis demand further research to accelerate bringing to market other novel PV technologies that do not suffer from the shortcomings of silicon. Emerging PV technologies such as PSCs and OPVs have to reach higher efficiencies and lifetimes. For this to be achieved, refinement of all the layers in these multi-layered structures is necessary.

Having demonstrated strategies to form an effective ETL in this thesis, the next natural step for the work could be the improvement of the active layer of OPVs. Indeed, part of the work carried out by the author in parallel to this thesis, has been preliminary testing of a ternary blend OPV where poly[4,4,9,9-tetrakis(4-hexylphenyl)-4,9-dihydro-s-indaceno[1,2-b:5,6-b']dithiophene-2,7-diyl-alt-5,5'-bis(2-octyldodecyl)-4H,4'H-[1,1-bithieno-[3,4-c]pyrrole]-4,4,6,6'(5H,5'H)-tetrone-3,3'-diyl] is used as the third component in PM6:Y6 blends for the first time to achieve a higher PCE.

Beyond PVs, ETLs find use in other optoelectronic devices. Given the excellent performance of the modified ETLs in OPV devices we are also motivated to adapt them to OLEDs.

Lastly, additional studies could be carried out to fully optimise the MgO modified ZnO ETLs, if these are to be used at an industrial scale. For example, the suggested doping strategy is 1-3% Mg content, but further testing can pinpoint the exact content necessary for maximum performance. In addition, an even lower annealing temperature for the ETL can be targeted along with a clearer understanding of the interplay between temperature and optimal doping to achieve the highest possible performance at the lowest possible temperature.

# Bibliography

1. I. Ierides, I. Squires, G. Lucarelli, T. M. Brown and F. Cacialli, *J. Mater. Chem. C*, 2021, **9**, 3901-3910.
2. I. Ierides, G. Ligorio, M. A. McLachlan, K. Guo, E. J. W. List-Kratochvil and F. Cacialli, *Sustain Energy Fuels*, 2022, **6**, 2835-2845.
3. I. Ierides, A. Zampetti and F. Cacialli, *Curr Opin Green Sust Chem*, 2019, **17**, 15-20.
4. M. Pompilio, I. Ierides and F. Cacialli, *Molecules*, 2022.
5. A. Attanzio, M. Rosillo-Lopez, A. Zampetti, I. Ierides, F. Cacialli, C. G. Salzmann and M. Palma, *Nanoscale*, 2018, **10**, 19678-19683.
6. IRENA, *Future of Solar Photovoltaic: Deployment, investment, technology, grid integration and socio-economic aspects (A Global Energy Transformation: paper)*, 2019.
7. U. S. E. I. Administration, *Annual Energy Outlook 2022 with projections to 2050*, EIA, 2022.
8. A. Hoekstra, Photovoltaic growth: reality versus projections of the International Energy Agency, <https://maartensteinbuch.com/2017/06/12/photovoltaic-growth-reality-versus-projections-of-the-international-energy-agency/>, (accessed 05/08/2022).
9. M. Knupfer, *Appl Phys a-Mater*, 2003, **77**, 623-626.
10. J. Nelson, *The physics of solar cells*, Imperial college press, 2004.
11. K. Guo, M. Righetto, I. Ierides and F. Cacialli, unpublished work.
12. F. B. Insights, Market Research Report/Renewables/Solar PV Market, [https://www.fortunebusinessinsights.com/industry-reports/solar-pv-market-100263#:~:text=The%20global%20solar%20photovoltaic%20\(PV,in%20the%202021%2D2028%20periods](https://www.fortunebusinessinsights.com/industry-reports/solar-pv-market-100263#:~:text=The%20global%20solar%20photovoltaic%20(PV,in%20the%202021%2D2028%20periods), (accessed 20/03/2022).
13. I. Fraunhofer Institute for Solar Energy Systems, PHOTOVOLTAICS REPORT, <https://www.ise.fraunhofer.de/content/dam/ise/de/documents/publications/studies/Photovoltaics-Report.pdf>, (accessed 20/03/2022).
14. C. U. N. Society, Sam Stranks: Halide Perovskites for Next-Generation Solar Photovoltaics, <https://www.youtube.com/watch?v=WbHes7IYYTU>, (accessed 05/08/2022).
15. B. S. Xakalashé and M. Tangstad, *Southern African Pyrometallurgy*, 2011.
16. G. M. Lazzerini, F. Di Stasio, C. Flechon, D. J. Caruana and F. Cacialli, *Appl Phys Lett*, 2011, **99**.
17. N. S. Lewis and D. G. Nocera, *P Natl Acad Sci USA*, 2007, **104**, 20142-20142.
18. C. J. Brabec, A. Distler, X. Y. Du, H. J. Egelhaaf, J. Hauch, T. Heumueller and N. Li, *Adv Energy Mater*, 2020, **10**.
19. L. Kinner, T. Dimopoulos, G. Ligorio, E. J. W. List-Kratochvil and F. Hermerschmidt, *Rsc Adv*, 2021, **11**, 17324-17331.

20. C. L. Cutting, M. Bag and D. Venkataraman, *J. Mater. Chem. C*, 2016, **4**, 10367-10370.
21. Q. Q. Lin, A. Armin, P. L. Burn and P. Meredith, *Accounts Chem Res*, 2016, **49**, 545-553.
22. P. Papagiorgis, A. Manoli, S. Michael, C. Bernasconi, M. I. Bodnarchuk, M. V. Kovalenko, A. Othonos and G. Itkos, *Acs Nano*, 2019, **13**, 5799-5809.
23. J. Dagar, S. Castro-Hermosa, G. Lucarelli, A. Zampetti, F. Cacialli and T. M. Brown, *Ieee J Photovolt*, 2019, **9**, 1309-1315.
24. M. J. Yuan, M. X. Liu and E. H. Sargent, *Nat Energy*, 2016, **1**.
25. E. El Mahboub, A. El Hichou and M. Mansori, *Phys Status Solidi A*, 2022, **219**.
26. B. J. Stanbery, D. Abou-Ras, A. Yamada and L. Mansfield, *J Phys D Appl Phys*, 2022, **55**.
27. N. R. E. Laboratory, Best Research-Cell Efficiency Chart, <https://www.nrel.gov/pv/cell-efficiency.html>, (accessed 05/08/2022).
28. A. Kojima, K. Teshima, Y. Shirai and T. Miyasaka, *J Am Chem Soc*, 2009, **131**, 6050.
29. W. J. Yin, J. H. Yang, J. Kang, Y. F. Yan and S. H. Wei, *J Mater Chem A*, 2015, **3**, 8926-8942.
30. Y. C. Liu, Z. Yang and S. Z. Liu, *Adv Sci*, 2018, **5**.
31. D. Shi, V. Adinolfi, R. Comin, M. J. Yuan, E. Alarousu, A. Buin, Y. Chen, S. Hoogland, A. Rothenberger, K. Katsiev, Y. Losovyj, X. Zhang, P. A. Dowben, O. F. Mohammed, E. H. Sargent and O. M. Bakr, *Science*, 2015, **347**, 519-522.
32. Y. Yang, M. J. Yang, Z. Li, R. Crisp, K. Zhu and M. C. Beard, *J Phys Chem Lett*, 2015, **6**, 4688-4692.
33. Oxford PV, <https://www.oxfordpv.com/>, (accessed 05/08/2022).
34. IDTECHX, Dr Isabel Al-Dhahir, Perovskite Photovoltaics: The Solution to our Energy Needs?, <https://www.idtechex.com/>, (accessed 05/08/2022).
35. Saule Technologies, <https://sauletech.com/>, (accessed 05/08/2022).
36. H. K. H. Lee, J. Y. Wu, J. Barbe, S. M. Jain, S. Wood, E. M. Speller, Z. Li, F. A. Castro, J. R. Durrant and W. C. Tsoi, *J Mater Chem A*, 2018, **6**, 5618-5626.
37. Epishine, <https://www.epishine.com/>, (accessed 05/08/2022).
38. Q. S. Liu, Y. F. Jiang, K. Jin, J. Q. Qin, J. G. Xu, W. T. Li, J. Xiong, J. F. Liu, Z. Xiao, K. Sun, S. F. Yang, X. T. Zhang and L. M. Ding, *Sci Bull*, 2020, **65**, 272-275.
39. F. Cacialli, personal communication.
40. O. V. Mikhnenko, R. Ruiter, P. W. M. Blom and M. A. Loi, *Phys Rev Lett*, 2012, **108**.
41. J. J. M. Halls, K. Pichler, R. H. Friend, S. C. Moratti and A. B. Holmes, *Appl Phys Lett*, 1996, **68**, 3120-3122.
42. T. Förster., *Annalen der Physik*, 1948, **2**, 55-75.
43. C. W. Tang, *Appl Phys Lett*, 1986, **48**, 183-185.
44. J. J. M. Halls, C. A. Walsh, N. C. Greenham, E. A. Marseglia, R. H. Friend, S. C. Moratti and A. B. Holmes, *Nature*, 1995, **376**, 498-500.

45. G. Yu, J. Gao, J. C. Hummelen, F. Wudl and A. J. Heeger, *Science*, 1995, **270**, 1789-1791.
46. J. K. Lee, W. L. Ma, C. J. Brabec, J. Yuen, J. S. Moon, J. Y. Kim, K. Lee, G. C. Bazan and A. J. Heeger, *J Am Chem Soc*, 2008, **130**, 3619-3623.
47. E. F. Manley, J. Strzalka, T. J. Fauvell, N. E. Jackson, M. J. Leonardi, N. D. Eastham, T. J. Marks and L. X. Chen, *Adv Mater*, 2017, **29**.
48. D. Luo, W. Jang, D. D. Babu, M. S. Kim, D. H. Wang and A. K. K. Kyaw, *J Mater Chem A*, 2022, **10**, 3255-3295.
49. R. J. E. Westbrook, I. Sanchez-Molina, J. M. Marin-Beloqui, H. Bronstein and S. A. Haque, *J Phys Chem C*, 2018, **122**, 1326-1332.
50. J. H. Lee, S. Y. Jeong, G. Kim, B. Park, J. Kim, S. Kee, B. Kim and K. Lee, *Adv Funct Mater*, 2018, **28**.
51. Z. G. Yin, J. J. Wei and Q. D. Zheng, *Adv Sci*, 2016, **3**.
52. R. Ganesamoorthy, G. Sathiyar and P. Sakthivel, *Sol Energ Mat Sol C*, 2017, **161**, 102-148.
53. Y. Y. Liang, Y. Wu, D. Q. Feng, S. T. Tsai, H. J. Son, G. Li and L. P. Yu, *J Am Chem Soc*, 2009, **131**, 56.
54. Y. Y. Liang, Z. Xu, J. B. Xia, S. T. Tsai, Y. Wu, G. Li, C. Ray and L. P. Yu, *Adv Mater*, 2010, **22**, 135.
55. J. S. Yu, Y. F. Zheng and J. Huang, *Polymers-Basel*, 2014, **6**, 2473-2509.
56. H. Y. Chen, J. H. Hou, S. Q. Zhang, Y. Y. Liang, G. W. Yang, Y. Yang, L. P. Yu, Y. Wu and G. Li, *Nat Photonics*, 2009, **3**, 649-653.
57. Q. Q. Gan, F. J. Bartoli and Z. H. Kafafi, *Adv Mater*, 2013, **25**, 2385-2396.
58. A. Savva, I. Burgues-Ceballos, G. Papazoglou and S. A. Choulis, *Acs Appl Mater Inter*, 2015, **7**, 24608-24615.
59. Z. H. Hu, F. J. Zhang, Q. S. An, M. Zhang, X. L. Ma, J. X. Wang, J. Zhang and J. Wang, *Acs Energy Lett*, 2018, **3**, 555-561.
60. L. C. Chang, M. Sheng, L. P. Duan and A. Uddin, *Org Electron*, 2021, **90**.
61. L. L. Zhan, S. X. Li, T. K. Lau, Y. Cui, X. H. Lu, M. M. Shi, C. Z. Li, H. Y. Li, J. H. Hou and H. Z. Chen, *Energ Environ Sci*, 2020, **13**, 635-645.
62. G. M. Paterno, J. R. Stewart, A. Wildes, F. Cacialli and V. G. Sakai, *Polymer*, 2016, **105**, 407-413.
63. G. M. Paterno, M. W. A. Skoda, R. Dalgliesh, F. Cacialli and V. G. Sakai, *Sci Rep-Uk*, 2016, **6**.
64. G. Paterno, A. J. Warren, J. Spencer, G. Evans, V. G. Sakai, J. Blumberger and F. Cacialli, *J. Mater. Chem. C*, 2013, **1**, 5619-5623.
65. G. M. Lazzerini, G. M. Paterno, G. Tregnago, N. Treat, N. Stingelin, A. Yacoot and F. Cacialli, *Appl Phys Lett*, 2016, **108**.
66. Z. Xiao, X. Jia, D. Li, S. Z. Wang, X. J. Geng, F. Liu, J. W. Chen, S. F. Yang, T. P. Russell and L. M. Ding, *Sci Bull*, 2017, **62**, 1494-1496.
67. H. J. Bin, L. Gao, Z. G. Zhang, Y. K. Yang, Y. D. Zhang, C. F. Zhang, S. S. Chen, L. W. Xue, C. Yang, M. Xiao and Y. F. Li, *Nat Commun*, 2016, **7**.
68. J. Liu, S. S. Chen, D. P. Qian, B. Gautam, G. F. Yang, J. B. Zhao, J. Bergqvist, F. L. Zhang, W. Ma, H. Ade, O. Inganäs, K. Gundogdu, F. Gao and H. Yan, *Nat Energy*, 2016, **1**.
69. X. T. Hu, R. Datt, Q. He, P. Kafourou, H. K. H. Lee, A. J. P. White, W. C. Tsoi and M. Heeney, *J. Mater. Chem. C*, 2022, **10**, 9249-9256.

70. P. Kafourou, Z. R. Qiao, M. Toth, F. Anies, F. Eisner, N. Gasparini and M. Heeney, *Acs Appl Mater Inter*, 2022.
71. W. C. Zhao, S. S. Li, H. F. Yao, S. Q. Zhang, Y. Zhang, B. Yang and J. H. Hou, *J Am Chem Soc*, 2017, **139**, 7148-7151.
72. J. Yuan, Y. Q. Zhang, L. Y. Zhou, G. C. Zhang, H. L. Yip, T. K. Lau, X. H. Lu, C. Zhu, H. J. Peng, P. A. Johnson, M. Leclerc, Y. Cao, J. Ulanski, Y. F. Li and Y. P. Zou, *Joule*, 2019, **3**, 1140-1151.
73. F. W. Zhao, S. X. Dai, Y. Q. Wu, Q. Q. Zhang, J. Y. Wang, L. Jiang, Q. D. Ling, Z. X. Wei, W. Ma, W. You, C. R. Wang and X. W. Zhan, *Adv Mater*, 2017, **29**.
74. L. X. Meng, Y. M. Zhang, X. J. Wan, C. X. Li, X. Zhang, Y. B. Wang, X. Ke, Z. Xiao, L. M. Ding, R. X. Xia, H. L. Yip, Y. Cao and Y. S. Chen, *Science*, 2018, **361**, 1094.
75. A. Armin, W. Li, O. J. Sandberg, Z. Xiao, L. M. Ding, J. Nelson, D. Neher, K. Vandewal, S. Shoaee, T. Wang, H. Ade, T. Heumuller, C. Brabec and P. Meredith, *Adv Energy Mater*, 2021, **11**.
76. A. Zampetti, A. Minotto, B. M. Squeo, V. G. Gregoriou, S. Allard, U. Scherf, C. L. Chochos and F. Cacialli, *Sci Rep-Uk*, 2017, **7**.
77. Q. He, P. Kafourou, X. T. Hu and M. Heeney, *Sn Appl Sci*, 2022, **4**.
78. T. J. Macdonald, A. J. Clancy, W. D. Xu, Z. Y. Jiang, C. T. Lin, L. Mohan, T. Du, D. D. Tune, L. Lanzetta, G. H. Min, T. Webb, A. Ashoka, R. Pandya, V. Tileli, M. A. McLachlan, J. R. Durrant, S. A. Haque and C. A. Howard, *J Am Chem Soc*, 2021, **143**, 21549-21559.
79. J. Dagar, S. Castro-Hermosa, G. Lucarelli, F. Cacialli and T. M. Brown, *Nano Energy*, 2018, **49**, 290-299.
80. Z. C. He, C. M. Zhong, S. J. Su, M. Xu, H. B. Wu and Y. Cao, *Nat Photonics*, 2012, **6**, 591-595.
81. H. L. Yip and A. K. Y. Jen, *Energ Environ Sci*, 2012, **5**, 5994-6011.
82. P. Li, Z. Z. Jiang, H. S. Huang, S. J. Tian, X. Y. Hu, W. J. Li, X. Bao and Y. Wang, *Mat Sci Semicon Proc*, 2020, **116**.
83. J. C. D. Faria, A. J. Campbell and M. A. McLachlan, *Adv Funct Mater*, 2015, **25**, 4657-4663.
84. Z. Q. Liang, Q. F. Zhang, L. Jiang and G. Z. Cao, *Energ Environ Sci*, 2015, **8**, 3442-3476.
85. Y. B. Lin, Y. Firdaus, M. I. Nugraha, F. Liu, S. Karuthedath, A. H. Emwas, W. M. Zhang, A. Seitkhan, M. Neophytou, H. Faber, E. Yengel, I. McCulloch, L. Tsetseris, F. Laquai and T. D. Anthopoulos, *Adv Sci*, 2020, **7**.
86. X. Y. Du, Y. Yuan, L. Zhou, H. Lin, C. J. Zheng, J. Y. Luo, Z. H. Chen, S. L. Tao and L. S. Liao, *Adv Funct Mater*, 2020, **30**.
87. J. C. Wang, W. T. Weng, M. Y. Tsai, M. K. Lee, S. F. Horng, T. P. Perng, C. C. Kei, C. C. Yu and H. F. Meng, *J Mater Chem*, 2010, **20**, 862-866.
88. J. B. Franklin, B. Zou, P. Petrov, D. W. McComb, M. P. Ryan and M. A. McLachlan, *J Mater Chem*, 2011, **21**, 8178-8182.
89. A. Rivera, A. Mazady and M. Anwar, *Solid State Electron*, 2015, **104**, 126-130.

90. S. Schumann, R. Da Campo, B. Illy, A. C. Cruickshank, M. A. McLachlan, M. P. Ryan, D. J. Riley, D. W. McComb and T. S. Jones, *J Mater Chem*, 2011, **21**, 2381-2386.
91. Y. M. Sun, J. H. Seo, C. J. Takacs, J. Seifert and A. J. Heeger, *Adv Mater*, 2011, **23**, 1679.
92. J. Q. Zhang, H. X. Yang, X. Y. Zhang, M. Morbidoni, C. H. Burgess, R. Kilmurray, S. H. Feng and M. A. McLachlan, *Inorg Chem Front*, 2020, **7**, 2809-2817.
93. J. Q. Zhang, M. Morbidoni, C. H. Burgess, J. Y. Wu, T. Du, K. Harrabi, D. J. Payne, J. R. Durrant and M. A. McLachlan, *Cryst Growth Des*, 2017, **17**, 6559-6564.
94. J. Q. Zhang, J. C. D. Faria, M. Morbidoni, Y. Porte, C. H. Burgess, K. Harrabi and M. A. McLachlan, *Adv Electron Mater*, 2016, **2**.
95. C. H. Wang, D. X. Luo, Y. J. Gao, G. Wang, C. Wang, P. F. Ma, H. Y. Li, S. P. Wen, W. Dong and S. P. Ruan, *J Phys Chem C*, 2019, **123**, 16546-16555.
96. J. Y. Xie, X. J. Wang, S. L. Wang, Z. T. Ling, H. Lian, N. Liu, Y. J. Liao, X. Y. Yang, W. S. Qu, Y. Peng, W. X. Lan and B. Wei, *Org Electron*, 2019, **75**.
97. C. Y. Chan, Y. F. Wei, H. T. Chandran, C. S. Lee, M. F. Luo and T. W. Ng, *Rsc Adv*, 2015, **5**, 77071-77074.
98. X. Y. Zhang, Y. Sun, M. Wang, H. X. Cui, W. F. Xie, L. Shen and W. B. Guo, *Sol Energy*, 2019, **181**, 9-16.
99. T. M. Brown, G. M. Lazzerini, L. J. Parrott, V. Bodrozic, L. Burgi and F. Cacialli, *Org Electron*, 2011, **12**, 623-633.
100. V. V. Brus, C. M. Proctor, N. A. Ran and T. Q. Nguyen, *Adv Energy Mater*, 2016, **6**.
101. J. D. Servaites, M. A. Ratner and T. J. Marks, *Energ Environ Sci*, 2011, **4**, 4410-4422.
102. B. A. Guo, J. X. Han, J. Qiu, C. Z. Yu, Y. Q. Sun, F. H. Li, Z. H. Hu and Y. Wang, *Acs Appl Mater Inter*, 2017, **9**, 42969-42977.
103. C. L. Hou and H. Z. Yu, *Chem Eng J*, 2021, **407**.
104. X. Song, G. L. Liu, P. Sun, Y. Liu and W. G. Zhu, *J Phys Chem Lett*, 2021, **12**, 10616-10621.
105. M. E. Ziffer, J. C. Mohammed and D. S. Ginger, *Acs Photonics*, 2016, **3**, 1060-1068.
106. E. Siebert-Henze, V. G. Lyssenko, J. Fischer, M. Tietze, R. Brueckner, M. Schwarze, K. Vandewal, D. Ray, M. Riede and K. Leo, *Aip Adv*, 2014, **4**.
107. V. Bodrozic, PhD, University College London, 2005.
108. M. Abd-Allah, J. Cann, S. V. Dayneko, A. Laventure, E. Cieplechowitz and G. C. Welch, *Acs Appl Electron Ma*, 2019, **1**, 1590-1596.
109. Y. T. Tang, Y. Pang, X. Li, B. B. Zong, B. N. Kang, S. R. P. Silva and G. Y. Lu, *J Colloid Interf Sci*, 2020, **562**, 142-148.
110. X. Cai, T. Yuan, X. F. Liu and G. L. Tee, *Acs Appl Mater Inter*, 2017, **9**, 36082-36089.
111. A. Soultati, A. Verykios, S. Panagiotakis, K. K. Armadorou, M. I. Haider, A. Kaltzoglou, C. Drivas, A. Fakharuddin, X. C. Bao, C. M. Yang, A. B. Yusoff, E. K. Evangelou, I. Petsalakis, S. Kennou, P. Falaras, K. Yannakopoulou,

- G. Pistolis, P. Argitis and M. Vasilopoulou, *Acs Appl Mater Inter*, 2020, **12**, 21961-21973.
112. Y. Y. Yu, C. Tseng, W. C. Chien and C. P. Chen, *Org Electron*, 2019, **69**, 20-25.
113. J. Dagar, G. Scavia, M. Scarselli, S. Destri, M. De Crescenzi and T. M. Brown, *Nanoscale*, 2017, **9**, 19031-19038.
114. Q. K. Rong, Q. Zhang, M. Q. Cui, L. Nian, D. F. Zheng, X. S. Gao, L. L. Shui, G. F. Zhou and N. Li, *Org Electron*, 2020, **81**.
115. G. S. Han, H. S. Chung, B. J. Kim, D. H. Kim, J. W. Lee, B. S. Swain, K. Mahmood, J. S. Yoo, N. G. Park, J. H. Lee and H. S. Jung, *J Mater Chem A*, 2015, **3**, 9160-9164.
116. E. N. Jayaweera, G. R. A. Kumara, C. Kumarage, S. K. Ranasinghe, R. M. G. Rajapakse, H. M. N. Bandara, O. A. Ileperuma and B. S. Dassanayake, *J Photoch Photobio A*, 2018, **364**, 109-115.
117. P. Docampo, P. Tiwana, N. Sakai, H. Miura, L. Herz, T. Murakami and H. J. Snaith, *J Phys Chem C*, 2012, **116**, 22840-22846.
118. S. Huang, B. N. Kang, L. Duan and D. D. Zhang, *J Colloid Interf Sci*, 2021, **583**, 178-187.
119. L. Song, W. J. Wang, E. Barabino, D. Yang, V. Korstgens, P. Zhang, S. V. Roth and P. Muller-Buschbaum, *Acs Appl Mater Inter*, 2019, **11**, 3125-3135.
120. V. H. Tran, S. H. Eom, S. C. Yoon, S. K. Kim and S. H. Lee, *Org Electron*, 2019, **68**, 85-95.
121. B. Y. Qi and J. Z. Wang, *Phys Chem Chem Phys*, 2013, **15**, 8972-8982.
122. M. G. Li, J. Li, L. S. Yu, Y. Zhang, Y. Z. Dai, R. F. Chen and W. Huang, *Front Chem*, 2020, **8**.
123. H. M. Kim, S. Cho, J. Kim, H. Shin and J. Jang, *Acs Appl Mater Inter*, 2018, **10**, 24028-24036.
124. Y. Z. Sun, Y. B. Jiang, H. R. Peng, J. L. Wei, S. D. Zhang and S. M. Chen, *Nanoscale*, 2017, **9**, 8962-8969.
125. M. Neukom, S. Zuffe, S. Jenatsch and B. Ruhstaller, *Sci Technol Adv Mat*, 2018, **19**, 291-316.
126. A. Savva, F. Petraki, P. Elefteriou, L. Sygellou, M. Voigt, M. Giannouli, S. Kennou, J. Nelson, D. D. C. Bradley, C. J. Brabec and S. A. Choulis, *Adv Energy Mater*, 2013, **3**, 391-398.
127. M. Wang, Y. Sun, J. X. Guo, Z. W. Li, C. Y. Liu and W. B. Guo, *Org Electron*, 2019, **74**, 258-264.
128. G. D. M. R. Dabera, J. Lee and R. A. Hatton, *Adv Funct Mater*, 2019, **29**.
129. F. G. Zhao, L. L. Deng, K. Wang, C. F. Han, Z. Liu, H. M. Yu, J. P. Li and B. Hu, *Acs Appl Mater Inter*, 2020, **12**, 5120-5127.
130. T. Jaouen, G. Jezequel, G. Delhaye, B. Lepine, P. Turban and P. Schieffer, *Appl Phys Lett*, 2012, **100**.
131. S. Prada, U. Martinez and G. Pacchioni, *Phys Rev B*, 2008, **78**.
132. OSSILA, PC70BM, <https://www.ossila.com/products/pc70bm>, (accessed 06/08/2022).
133. T. M. Brown, J. S. Kim, R. H. Friend, F. Cacialli, R. Daik and W. J. Feast, *Appl Phys Lett*, 1999, **75**, 1679-1681.

134. S. H. Huang, N. Ali, Z. X. Huai, J. P. Ren, Y. S. Sun, X. H. Zhao, G. S. Fu, W. G. Kong and S. P. Yang, *Org Electron*, 2020, **78**.
135. Y. Q. Xia, C. Wang, B. Dong, G. Wang, Y. Chen, R. C. I. MacKenzie, W. Dong, S. P. Ruan, Y. Z. Liu and S. P. Wen, *Acs Appl Mater Inter*, 2021, **13**, 14436-14445.
136. S. Park, R. Kang and S. Cho, *Curr Appl Phys*, 2020, **20**, 172-177.
137. B. Usmani, R. Ranjan, Prateek, S. K. Gupta, R. K. Gupta, K. S. Nalwa and A. Garg, *Sol Energy*, 2021, **214**, 220-230.
138. D. Chi, S. D. Lu, R. Xu, K. Liu, D. W. Cao, L. Y. Wen, Y. Mi, Z. J. Wang, Y. Lei, S. C. Qu and Z. G. Wang, *Nanoscale*, 2015, **7**, 15251-15257.
139. G. L. Xin Song, Po Sun, Yu Liu, and Weiguo Zhu, *The Journal of Physical Chemistry Letters*, 2021, **0**.
140. M. Chrzanowski, M. Kuchowicz, R. Szukiewicz, P. Sitarek, J. Misiewicz and A. Podhorodecki, *Org Electron*, 2020, **80**.
141. L. S. Wang, J. Lin, X. Y. Liu, S. Cao, Y. J. Wang, J. L. Zhao and B. S. Zou, *J Phys Chem C*, 2020, **124**, 8758-8765.
142. H. M. Kim, W. Jeong, J. H. Kim and J. Jang, *Nanomaterials-Basel*, 2020, **10**.
143. L. X. Wang, J. Y. Pan, J. P. Qian, W. Lei, Y. J. Wu, W. Zhang, D. K. Goto and J. Chen, *J. Mater. Chem. C*, 2018, **6**, 8099-8104.
144. M. M. Yan, Y. Li, Y. T. Zhou, L. Liu, Y. Zhang, B. G. You and Y. Li, *IEEE Photonics J*, 2017, **9**.
145. S. B. Heo, J. S. Shin, T. Y. Kim, S. Park, W. H. Jung, H. Kim, J. A. Hong, B. S. Kim, Y. Park, B. D. Chin, J. G. Kim and S. J. Kang, *Curr Appl Phys*, 2021, **29**.
146. H. Wu, Y. Zhang, X. Y. Zhang, M. Lu, C. Sun, T. Q. Zhang and W. W. Yu, *Adv Opt Mater*, 2017, **5**.
147. Y. J. Lin, P. H. Wu, C. L. Tsai, C. J. Liu, Z. R. Lin, H. C. Chang and C. T. Lee, *J Appl Phys*, 2008, **103**.
148. G. El Hallani, S. Nasih, N. Fazouan, A. Liba, M. Khulili, M. Sajjeddine, M. Mabrouki, L. Laanab and E. H. Atmani, *J Appl Phys*, 2017, **121**.
149. A. Singh and P. Kumar, *J Optoelectron Adv M*, 2014, **16**, 311-316.
150. L. Meng, X. G. Yang, H. Y. Chai, Z. R. Lv and T. Yang, *Thin Solid Films*, 2019, **672**, 186-191.
151. A. Ringleb, R. Ruess, N. Hofeditz, W. Heimbrod, T. Yoshida and D. Schlettwein, *Phys Chem Chem Phys*, 2021, **23**, 8393-8402.
152. C. J. Raj, K. Prabakar, S. N. Karthick, K. V. Hemalatha, M. K. Son and H. J. Kim, *J Phys Chem C*, 2013, **117**, 2600-2607.
153. I. Biswas, P. Roy, U. Maity, P. K. Sinha and A. K. Chakraborty, *Thin Solid Films*, 2020, **711**.
154. M. B. Xing, Y. Y. Wei, D. D. Wang, Q. Shen and R. X. Wang, *Curr Appl Phys*, 2021, **21**, 14-19.
155. J. X. Song, E. Q. Zheng, L. J. Liu, X. F. Wang, G. Chen, W. J. Tian and T. Miyasaka, *Chemsuschem*, 2016, **9**, 2640-2647.
156. X. Li, J. Y. Yang, Q. H. Jiang, W. J. Chu, J. W. Xin, J. D. Hou and H. Lai, *Electrochim Acta*, 2018, **261**, 474-481.
157. R. T. Ginting, C. C. Yap, M. Yahaya and M. M. Salleh, *J Alloy Compd*, 2014, **585**, 696-702.

158. Z. G. Yin, Q. D. Zheng, S. C. Chen, D. D. Cai, L. Y. Zhou and J. Zhang, *Adv Energy Mater*, 2014, **4**.
159. B. A. MacLeod, P. Schulz, S. R. Cowan, A. Garcia, D. S. Ginley, A. Kahn and D. C. Olson, *Adv Energy Mater*, 2014, **4**.
160. N. Johansson, F. Cacialli, K. Z. Xing, G. Beamson, D. T. Clark, R. H. Friend and W. R. Salaneck, *Synthetic Met*, 1998, **92**, 207-211.
161. V. D. Mihailetschi, H. Xie, B. de Boer, L. J. A. Koster and P. W. M. Blom, *Adv Funct Mater*, 2006, **16**, 699-708.
162. J. Vollbrecht and V. V. Brus, *Energies*, 2021, **14**, 4800.
163. Kim J.S., Lagel B., Moons E., Johansson N., Baikie I.D., Salaneck W.R., Friend R.H. and Cacialli F., *Synthetic Met*, 2000, **111-112**, 311-314.
164. A. Janotti and C. G. Van de Walle, *Rep. Prog. Phys.*, 2009, **72**, 126501.
165. X. Yu, X. Yu, M. Yan, T. Weng, L. Chen, Y. Zhou and J. Wei, *Sens. Actuator A Phys.*, 2020, **312**, 112163.
166. B. Kim, D. Lee, B. Hwang, D. J. Kim and C. K. Kim, *Mol Cryst Liq Cryst*, 2022, **735**, 61-74.